A STACKED BETAVOLTAIC BATTERY USING A LATERAL-GROWTH-SMOOTHED BGAN INTRINSIC REGION

A Dissertation
Presented to
The Academic Faculty

by

Charles E. Munson IV

In Partial Fulfillment
of the Requirements for the Degree
Doctor of Philosophy in the
School of Electrical and Computer Engineering

Georgia Institute of Technology

December 2016

A STACKED BETAVOLTAIC BATTERY USING A LATERAL-GROWTH-SMOOTHED BGAN INTRINSIC REGION

Approved by:

Dr. Abdallah Ougazzaden, Advisor
School of Electrical and Computer Engineering
Georgia Institute of Technology

Dr. Alexandre Locquet
School of Electrical and Computer Engineering
Georgia Institute of Technology

Dr. Paul L Voss, Co-Advisor
School of Electrical and Computer Engineering
Georgia Institute of Technology

Dr. Bertrand Boussert
School of Electrical and Computer Engineering
Georgia Institute of Technology

Dr. Jean Paul Salvestrini
Professeur des Universités
Directeur du laboratoire
Université de Lorraine et Supélec

Dr. Nico Declercq
School of Mechanical Engineering
Georgia Institute of Technology

Date Approved: October 19, 2016

ACKNOWLEDGEMENTS

I would like to thank my family and friends for all of the love and support that they have given me throughout my life, and for having encouraged me to always try my best in everything that I do.

Additionally I would like to thank my colleagues and our partner labs who helped make the results in this thesis possible. Without their extensive help and guidance, it would not have been possible to have performed all of the work that was included here, ranging from device fabrication to device processing and Ni-63 testing.

TABLE OF CONTENTS

LIST OF TABLES

LIST OF FIGURES

LIST OF EQUATIONS

NOMENCLATURE

AFM	Atomic Force Microscopy
CL	Cathode Luminescence
DLTS	Deep-Level Transient Spectroscopy
EHP	Electron-Hole Pair
HAADF	High-Angle Annular Dark-Field
IV/CV	I - current, V - voltage, C - capacitance
IQE	Internal Quantum Efficiency
Ni-63	Ni-63 (radioactive isotope of nickel)
PCE	Power Conversion Efficiency
PVD	Physical Vapor Deposition
PIN	p-type / intrinsic / n-type device stack
Pm-147	Promethium-35 (radioactive isotope of promethium)
S-35	Sulfur-35 (radioactive isotope of sulfur)
SEM	Scanning Electron Microscopy
STEM	Scanning Transmission Electron Microscopy
TLM	Transmission Line Measurement

SUMMARY

An investigation into possible ways to increase the efficiency of betavoltaic battery technology by using a novel material, BGaN, by utilizing the stacking of PIN devices, and to research designs to increase the radioactive source efficiency by reducing self-absorption.

One major issue in the development of nitride-based PIN devices is maximizing efficiency with a strong electric field across the intrinsic region. The high carrier concentration of intrinsic GaN due to unintentional doping reduces the possible PIN electrical field strength and results in high recombination of electron-hole pairs generated. By using BGaN, we expect to reduce this carrier concentration and increase overall device efficiency.

Additionally, most betavoltaic battery designs only consider beta particle collection on one side of the radioactive source. This gives a maximum overall efficiency of only 50%, since energy that emits away from the device cannot be collected. By creating a stacked package design, we expect to efficiently collect beta particles emitted in all directions by the radioactive source, thereby potentially doubling the overall battery efficiency.

Since Ni-63 in particular is highly susceptible to self-absorption, steps to reduce these effects should be taken to help increase the efficiency of the radioactive source itself. Although this does not affect the overall device efficiency, it does have an impact on the maximum potential power output of the device given a fixed amount of Ni-63 material. Various designs have been proposed by us that aim to reduce the effects of self-absorption

in the radioactive source, and we expect to achieve up to 95% source efficiency from our designs.

Finally, a study demonstrating the durability of our materials and devices will be discussed, which show that exposure to radioactive Ni-63 over 100 years will not appreciably degrade the performance of our betavoltaic battery. This ensures our battery could maintain a high level of power and efficiency for at least 100 years.

We will discuss the simulations and designs that we created, which are necessary to achieve these results, as well as discuss the fabrication and packaging of a Ni-63 betavoltaic battery that is used to realize the designs. A comparison of the modeling predictions with experimental data will be explored, demonstrating the accuracy of our models and the quality of our materials and designs.

This doctoral research is funded by the BATGaN project, which aims to create a high-efficiency betavoltaic battery using Ni-63 and a stacked design. The BATGaN project is funded by the CNRS (Centre national de la recherche scientifique), a large government research organization in France, and the research is designed to be done over a period of three years. Research was done in partnership with LPN (Laboratoire de Photonique et de Nanostructures), Nanovation and the CEA (Commissariat à l'énergie atomique et aux énergies alternatives).

CHAPTER 1

INTRODUCTION

Battery size requirements have been shrinking over the last several decades, while power density requirements have steadily been increasing at the same time. Classic, chemical-based batteries do not scale well with size, and thus do not perform well when shrunk down to power micro-sized devices. Additionally, these batteries have comparably short lifetimes, or must be constantly recharged.

Nuclear batteries provide high power-density with a long half-life (100 years for Ni-63 [1]), and thus do not need to be refueled or recharged as often. Additionally, the beta particles emitted by Ni-63, for instance, is low enough energy to be blocked by the surface layer of dead skin that covers our bodies. Thus, batteries designed with this fuel source can be easily and safely packaged with minimal danger.

An important part of designing devices is having a deep understanding of how the processes involved in the device will work. In order to effectively design a betavoltaic battery, the processes involved beginning from the behavior of the nuclear material all the way through the current extraction from the device itself must be well understood.

Ni-63 Material Limitations

Due to the density of nickel and the low-energy beta particles that are most commonly emitted from the material, Ni-63 self-absorption plays a large role in determining the maximum amount of power a device can obtain given certain device dimensions. Research has previously been done that summarizes the self-absorption properties of Ni-63 and determined via simulations that the power saturates at 2.85 uW/cm^2 [2]. It was determined that the optimal thickness of Ni-63 was therefore around 1.5 um, resulting in a maximum power of around 2.15 uW/cm^2. Note that self-absorption

plays a role in all beta-emitting materials, such as Pm-147 with higher-energy beta particles, though often to a lesser extent than Ni-63 [3].

Betavoltaic Battery Technology Overview

Theoretical research into using GaN as a betavoltaic battery has been done over the past few decades. Polikarpov and Yakimov published simulation results for Ni-63-like particles with a Scanning Electron Microscope at various angles into the material and found the energy loss at various depths within GaN and Si [4]. Simulations done by Zuo, Khou and Ke were done with Ni-63 on GaN, showing expected voltages and currents from their model that was then validated with real-life devices [5]. Additionally, San, Yao, et al published simulation results on a Ni-63 Schottky GaN device, theorizing it could achieve an efficiency of 2.25% [6]. In addition to GaN-based betavoltaic batteries using Ni-63, theoretical research has also been done using various other radioactive materials like Pm-147 and S-35 [7, 8], and semiconductor materials such as GaAs, SiC and Si [8-11], with expected performances ranging from poor (high EHP recombination rates) to nearly 5% efficiency.

Similarly, experimental research has also been done in this field. A group comprised of Lu, Wang and Yao created a GaN-based PIN device that boasted a potential efficiency of up to 1.6% [12]. Devices using iron-doping of the intrinsic region of a GaN-based PIN similarly yielded results ranging from 0.98% to 2.7% [13-15]. It should be noted, however, that the 2.7% efficiency calculation is based on a non-standard efficiency equation which over-estimates efficiency when compared to other publications; an efficiency of 0.98% is thus considered to be state-of-the-art for a Ni-63 GaN PIN battery. Likewise, Ni-63 experimental research using non-GaN-based materials have been performed [1, 16-17], yielding potentially promising results after various changes could be made to the designs in the future.

Stacked Design Technology

It is important to take note that previous research into GaN-based betavoltaic batteries using Ni-63 have typically provided device efficiencies that were below 2%, and often below 1% [18-20]. These devices were simple PIN structures that did not take advantage of stacking techniques.

Traditional betavoltaic battery device designs would, by their very nature, fail to collect particles emitted away from the PIN structure. By stacking two PIN devices and sandwiching the beta material in-between the two PINs, there is the ability to effectively double the potential amount of energy collected (doubling the efficiency vs. a single PIN structure by itself) [21]. Previous designs that tried to achieve similar results (e.g., via stacking, implantation, 3D surfaces etc.) were limited by the radioactive or semiconductor materials chosen (typically silicon) [22-26].

For instance, research has been performed involving infusion of radioactive material directly into the semiconductor [26]. This method boasted an efficiency of 7%, but was based on the usage of radioactive sulfur-35 (S-35) as a power source [25] (which matched well with their chosen semiconductor material of selenium). One issue with this is that S-35 has a half-life of only 87 days, and thus does not compare as well to other radioactive materials with half-lives that span several years or decades.

Research into usage of 3D surfaces has also been performed with varying levels of success [22-24]. These devices were silicon-based, however (low radiation resistance and thus a higher material degradation than GaN). These devices also did not typically see a significant efficiency boost over usage of the Ni-63 PIN structures. One device created used a 3D surface but did not take advantage of stacking – leading to an efficiency of 1.7% [23] that could potentially have been higher with a stacking design. Another device created took advantage of both stacking and a 3D surface, but only obtained an efficiency of around 1% [22] due to a high recombination-generation current in their silicon.

Carbon nanotubes have also been investigated as a collection material with Ni-63 as a radiation source, but this device achieved only 0.1% efficiency [27]. Various other publications with non-GaN materials have also been published, but these were based on simple PIN devices or Schottky devices that did not take advantage of stacking and did not result in efficiencies higher than previously mentioned [28-33].

Material Choice

For many non-nitride semiconductor materials such as silicon, the material will degrade quickly when exposed to high-energy beta particles. By using GaN for the device, the material has a significantly-increased durability when exposed to beta particles over long periods of time [35]. GaN-based materials are also particularly well-suited for usage in betavoltaic devices because they have a high theoretical efficiency of around 27% (compared with around 15% with silicon, for instance) [34].

Various experiments have been performed to test the effects of beta-particle bombardment on nitride-based materials, predominantly using a Scanning Electron Microscope (SEM) as a beta particle source. The results were mixed depending on the doping of the material that was bombarded and the amount of energy used for bombardment.

When bombarding p-GaN materials with electron energies in the range of 5 KeV to 20 KeV, for instance, the results reported were either an increase in cathode-luminescence (CL) intensity or an increase in diffusion length [36-40]. This improvement in material quality is theorized to be because of annealing effects of the p-GaN material; even when bombardment was performed on more complicated structures such as Multi-Quantum Wells, no negative effects were noticed in the material other than the aforementioned annealing-like effects [41-44].

In the worst case scenario, bombardments performed noticed no significant changes to the material properties when exposed to an SEM beam ranging from 5 – 20 KeV [45-49]. The dosages and energies used in the previously-mentioned experiments were all within the range of what would be expected to be released from Ni-63 (which has an average energy of 17 KeV). In fact, the only time degradation was noticed in the material is when very high energies, in the range of 1 – 3 MeV, were used for bombardment [50-51]. Note, however, that this is far outside the maximum energy range seen in Ni-63 (which is around 67 KeV) and would thus not be expected to occur with a Ni-63-based betavoltaic battery.

An important issue with nitride-based semiconductors is achieving high p-type doping, however, as well as achieving a low unintentional-doping of the intrinsic region. This limits the effectiveness of using existing technologies, such as 3D device surfaces, to maximize efficiency. By implementing a combination of technologies to reduce the carrier concentration of the PIN intrinsic region, using lift-off techniques and stacking devices, efficiency can still be maximized using just nitride technologies.

Intrinsic Region Carrier Concentration

A low unintentional doping of the intrinsic region will generate a stronger electric field, which will allow for a larger intrinsic region thickness. Most of the electron-hole pairs that are collected will be generated in the intrinsic region (where the field to separate the electron-hole pairs is the strongest), which means that an optimal device will have a larger intrinsic region thickness.

Even the best i-GaN growth today does not have a low enough unintentional doping to span a micrometer or more, unless treatment with impurities such as iron, for instance, is done [13]. This creates many traps within the material, however, and degrades device performance. Because of this, a new method of lowering the

unintentional doping of the intrinsic region is needed that produces a higher material quality.

Recent experimentation has shown that the BGaN alloy of GaN can have both a low carrier concentration (undoped) as well as a high mobility [52]. For instance, a boron composition of 1.34% is shown to have a carrier concentration of only $3x10^3/cm^3$ while maintaining a high mobility of 96 cm^2/Vs. This makes it a great semiconductor material to use for the intrinsic region, as it has the desirable aforementioned properties.

The drawback of using BGaN is that the growth quality of current technology does not allow it to be effectively grown at the desired thicknesses (close to, or exceeding, 1 um). By breaking the BGaN layer up into thinner sections and using a thin, magnesium-doped, lateral-growth smoothing GaN layer on top of these BGaN layers, the material growth quality is able to be increased and the BGaN-GaN layers could be combined and extended to the desired thicknesses [53-55].

CHAPTER 2

RADIATION AND DEVICE SIMULATIONS

The ability to accurately model Ni-63 emission and absorption in a GaN device has various benefits, especially considering the relatively high cost of purchasing and using radioactive material. Being able to predict real-life device performance without needing to purchase or use Ni-63 allows for a much more efficient, streamlined device development. In light of this fact, the first task for developing a betavoltaic battery was properly modeling both the radioactive material and the device itself. Some of the results described in this chapter have been published as "Model of Ni-63 battery with realistic PIN structure" [56].

In order to create an accurate device model, a real-life, mock device had to be emulated. In Figure 1, we can see the 4 mm x 4 mm area PIN device used for experimental analysis. It includes a 40 nm current spreading layer on top of the device (20 nm of gold and 20 nm of palladium). This is followed by a 150 nm p-GaN region (carrier concentration of $5 \times 10^{17}/cm^3$) and a 600 nm i-GaN region (estimated to have an unintentionally doped carrier concentration of around $3 \times 10^{16}/cm^3$). The rest of the device is n-type GaN with a carrier concentration of around $3 \times 10^{18}/cm^3$.

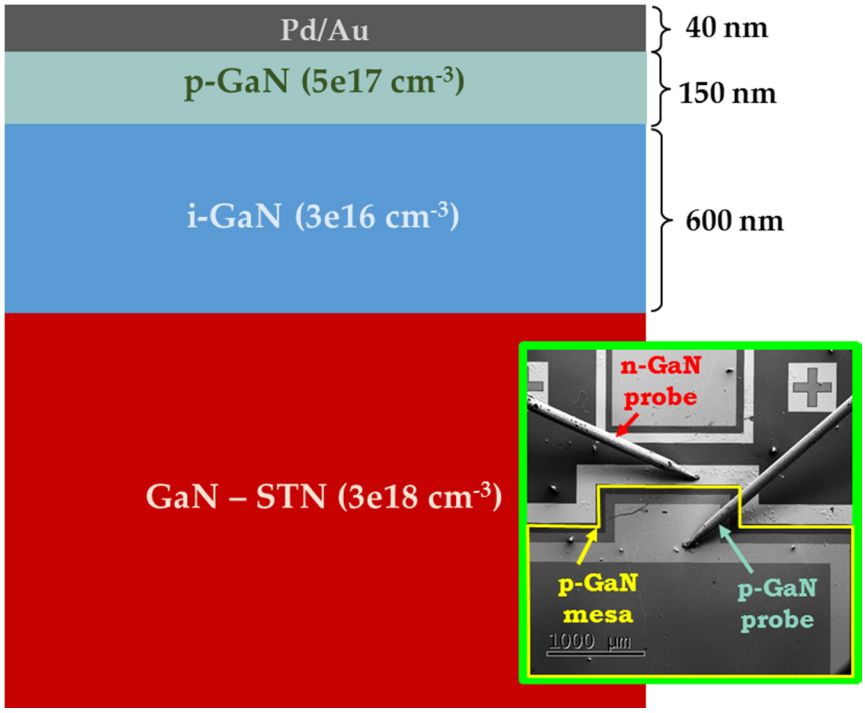

Figure 1: Experimental device structure. Inset: SEM image of device with n-GaN and p-GaN probes, as well as p-GaN mesa.

The inset shows a SEM image of the actual device from the top view along with contacting probes touching the n-contacts and p-contacts. The p-GaN mesa is also highlighted and can clearly be seen in this image.

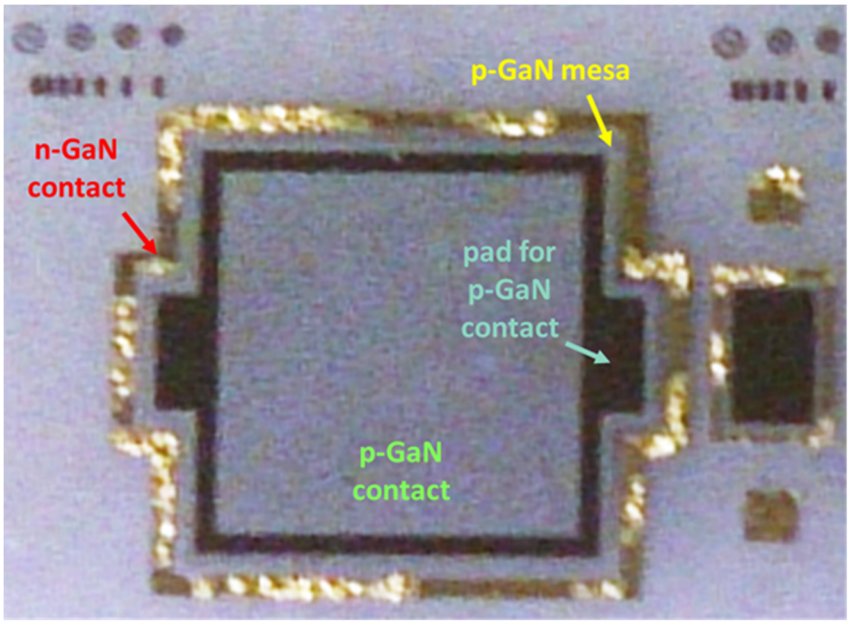

Figure 2: Optical microscope image of experimental device.

Figure 2 shows the experimental device under an optical microscope. Clearly visible are the n-GaN contacts and large p-GaN contact. The dark gray pad for the p-GaN contact is also visible around the p-GaN contact, while the p-GaN mesa shows the separation between the p-GaN and n-GaN regions.

SEM E-beam Model

The first part of the model deals with mimicking Ni-63 emissions with an e-beam current. Since the e-beam can only emit at a single electron energy, we had to choose which energy would most accurately represent the energy of beta particles coming from Ni-63. It is well known that the most probable energy released from Ni-63 is around 17 keV and quickly declines in probability when the energies fall outside the range of 5 keV and 50 keV [11], as displayed in Figure 3.

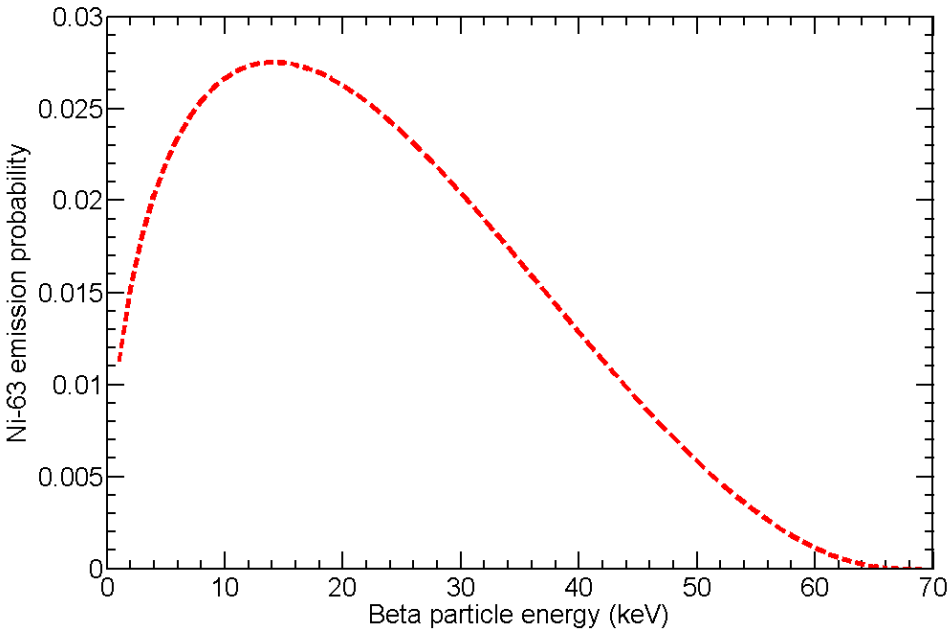

Figure 3: Ni-63 emission profile vs beta particle energy [71].

As can be seen in Figure 4, a Probability Density Function (PDF) of the electron energy absorption profile was calculated based on the CASINO 2 Monte Carlo simulations for 17 keV. The integrated area under the curve for a given depth range provides the percentage of electron energy that is absorbed in that depth range, and the area under the entire curve (including the 40 nm metal spreading layer, not shown) will add up to 100%. Note that this does not take into account backscattering of electrons off of the sample surface; the e-beam source currents used here are the specimen currents, which ignores the effects of backscattered, secondary, and transmitted electrons.

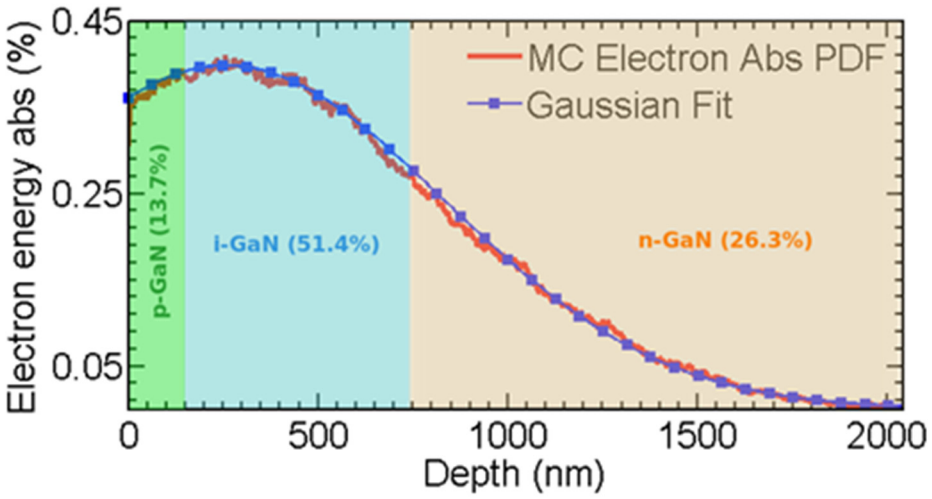

Figure 4: Electron energy absorption PDF at 17 keV SEM, first 40 nm of spreading layer not included.

Electron energies absorbed within the 40 nm of metal spreading layer are assumed to be lost, and so are not included in the absorption model (though they account for 8.6% of electron energy absorption). This absorption model was then later used in the device simulations to determine the electron-hole pairs that would be generated from such a profile (and consequently the current that would be generated).

We can see here that around 22% of the energy is lost from penetration through the metal spreading layer (not shown) and p-GaN regions (8.6% and 13.7%, respectively) of the device, while 51.4% of the total energy will fall within the intrinsic GaN region. The remaining 26.3% of the energy is lost in the n-GaN region and substrate.

Figure 5 shows the distribution of beta particle energy absorption in certain regions of the device versus electron energy. As expected, lower electron energies are almost completely absorbed by the current spreading layer, while electron energies from around 10 keV to 22 keV are predominantly absorbed within the i-GaN region of the device.

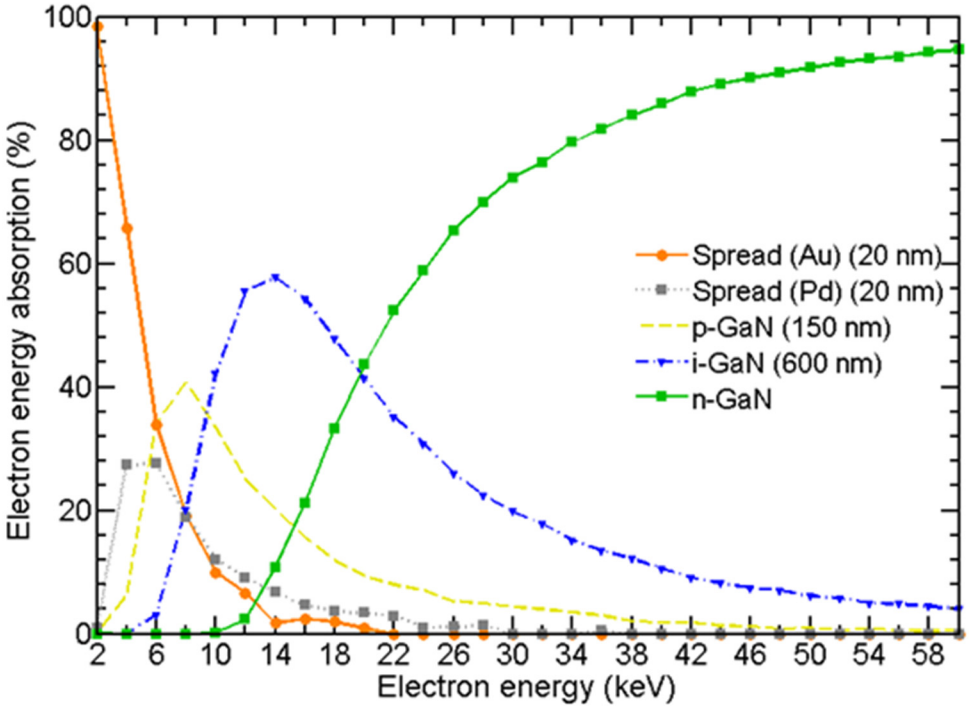

Figure 5: Distribution of electron energy absorption versus electron energy across various device regions.

Higher electron energies, above 22 keV, are lost to absorption mostly within the n-GaN region of the device. Note again that this figure does not show losses due to backscattering from the device surface but is intended to show which regions of the device are absorbing the most amounts of energy at different electron energies.

We can similarly see in Figure 6 the energy absorption versus electron energy scaled by the probability of that energy being emitted by Ni-63. The most obvious difference with the previous figure is that energies above 30 keV are unlikely to be emitted from Ni-63 and thus do not play an important role in the absorption profile. Energies around 17 keV (with the highest probability of emission) are higher here because they play a larger role in the absorption profile.

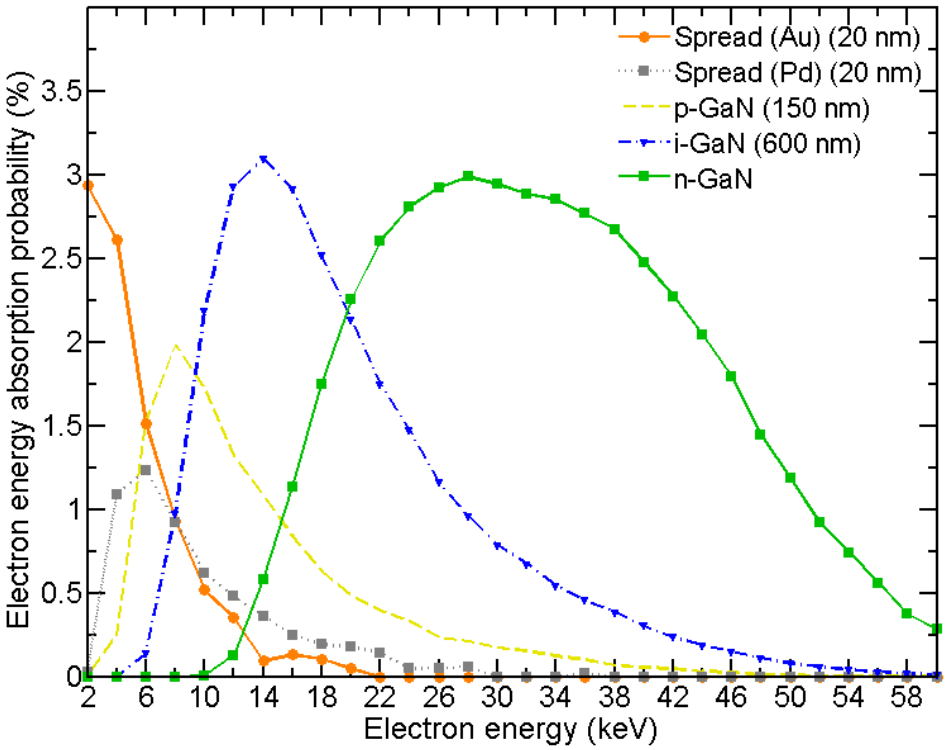

Figure 6: Distribution of electron energy absorption versus electron energy across various device regions, scaled to take probability of Ni-63 emission profile into account.

Radiation Absorption Model

In order to extend these e-beam models to a viable Ni-63 model, various Ni-63 thicknesses had to be used in order to correctly take into account the self-absorption of beta particles, various penetration angles had to be taken into account, and multiple energies had to be chosen to fit the beta particle energies expected to be emitted from Ni-63. A range of 5 nm to 4000 nm of Ni-63 were used so that the saturation effects could be seen at both large and small Ni-63 thicknesses.

These simulation results, denoted as MC_abs(y,d,e,θ) in Equation 1, can then be combined together to form an overall Ni-63 model. This model takes into account reflectance off of the device surface and all angles of penetration (Equation 1), an energy

emittance profile mimicking that of Ni-63 (Equation 2), and is valid for various Ni-63 thicknesses as chosen by Equation 3.

$$ABS_\theta(y,d,e) = \sum_{\theta=0}^{\pi}(MC\_abs(y,d,e,\theta) * (1 - R_\theta)) * \Delta\theta, \quad (1)$$

$$ABS_e(y,d) = \sum_{e=5k}^{60k}(ABS_\theta(y,d,e) * \Pr(E = e)) * \Delta e, \quad (2)$$

$$Absorption(y,t) = \sum_{d=0}^{t} ABS_e(y,d) * \Delta d, \quad (3)$$

$$P_{nm} \sim \rho * \frac{A}{1e7} * E_{avg} * q \quad \left(\frac{W}{cm^2 * nm}\right), \quad (4)$$

Constants are defined as follows: R_θ is the reflectance at a given angle θ, Pr(E=e) is the probability of an electron being emitted from Ni-63 at the given energy e, y is the y-coordinate of depth into the device and t is the total Ni-63 thickness.

In Equation 4 we can see the estimation for the total amount of energy released from a 1 cm^2 x nm volume of Ni-63, not considering self-absorption (which is taken into account in the simulation data, MC_abs). Of course this can be easily scaled up depending on the thickness of Ni-63 that has been chosen: for instance, 500 nm of Ni-63 (over a 1 cm^2 surface area) would emit a total power of $500*P_{nm}$. Here, ρ is the density of Ni-63 (8.91 g/cm^3) and A is the specific activity of Ni-63 per gram (2.2 x 10^{12} Bq/g) [3], E_{avg} is the average energy released from Ni-63 (17 keV) and q is the electron charge (1.6022 x 10^{-19} C).

The results of these simulations can be seen in Figure 7, where we show the absorption profile of beta particles in GaN for various Ni-63 thicknesses. For very thin layers of Ni-63 the GaN absorption is seen to be more hyperbolic, while for thick Ni-63 layers the profile smoothes out to a standard exponential absorption.

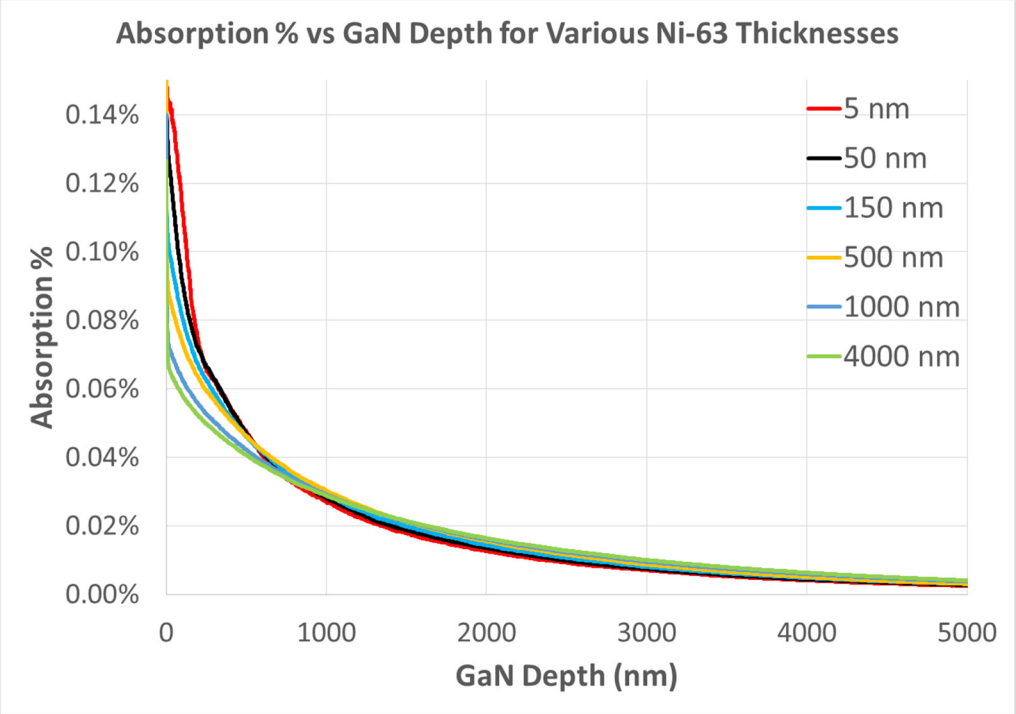

Figure 7: GaN absorption profiles for various Ni-63 thicknesses.

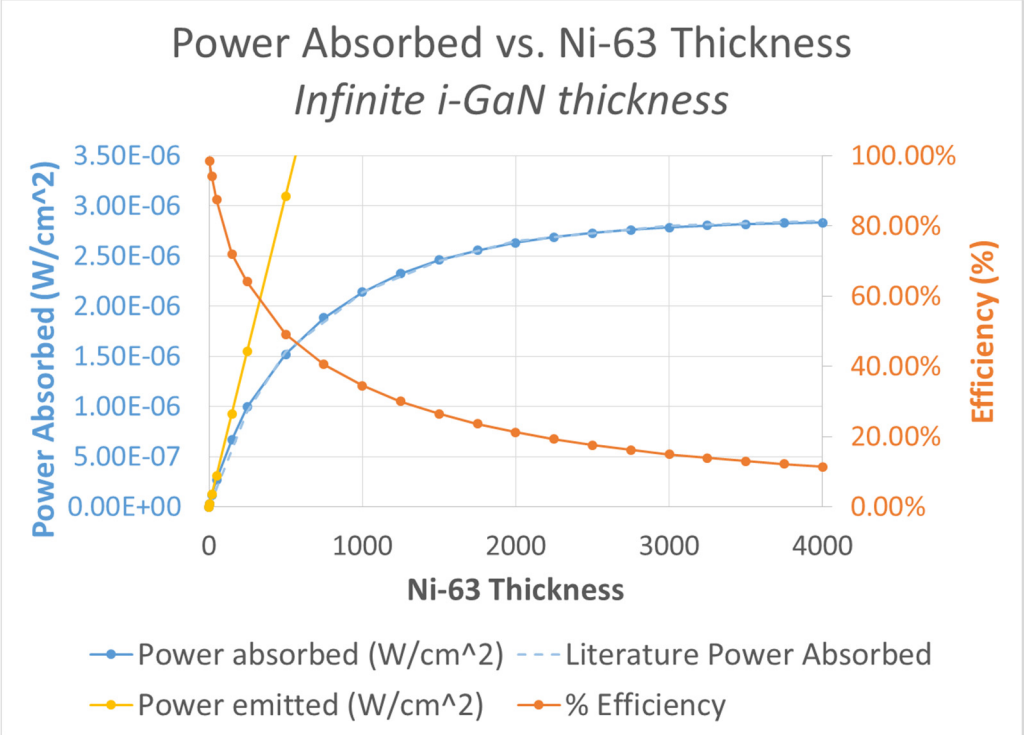

Figure 8: Power absorption efficiency in GaN vs. Ni-63 thickness.

Finally, Figure 8 shows that the power absorbed in the GaN material saturates towards 2.85 uW/cm^2 as the Ni-63 thickness increases. The highest efficiency Ni-63 thickness is infinitely thin, of course, since this would result in the least self-absorption. It can be estimated that the optimal Ni-63 thickness is somewhere around 1500 nm of Ni-63, since the power quickly begins to saturate after this point. It can be seen that these results match well with results published in literature [3]. This model is in the process of being published.

Device and Material Simulations

Now that a model of the behavior of beta particle-like absorption into the GaN PIN had been created using Monte Carlo simulations, detailed device model simulations had to be done.

For the device simulations, we used Silvaco TCAD software. Parameters to use in the simulation for the GaN materials involved were taken from Mnatsakanov et al. [57] and Vurgaftman and Meyer. [58] All other parameters for the simulated device were taken from measurements made directly from the experimental device (minority carrier concentrations, region thicknesses, etc.).

Based on literature, [34] it has been shown that for GaN-based materials, the maximum betavoltaic current efficiency is approximately 27%. Because the device simulations do not take this into account (it assumes the particles are photons, whose frequency we have chosen to be optimal for absorption in GaN), we multiply the efficiency of the device by 0.27.

Finally, an absorption profile for the SEM electrons needed to be imported into Silvaco software for device simulation. Because this software does not support beta

particles but only photons, the absorption model of the electrons had to be accurately mapped to the photon model in Atlas. In order to achieve this, a PDF was fitted to the Monte Carlo simulation data from Figure 3, represented mathematically in the following equation:

$$Absorption\ rate \sim \frac{1}{\sigma * \sqrt{2\pi}} * \exp\left(-\frac{(y-\mu)^2}{2*\sigma^2}\right), \quad (5)$$

where y is the vertical depth down into the GaN material in nanometers, μ is the mean value for our PDF (256.53 nm), and σ is the standard deviation (576 nm). Note that this equation gives us the shape of absorption and an arbitrary magnitude. The magnitude is determined based on the expected device efficiency (for a perfect device) with losses due to the current spreading layer (already taken into account previously, ~8% loss), beta particle efficiency, and losses in the p-GaN and n-GaN regions (whose electron-hole pairs will predominantly not be successfully collected).

In order to calibrate the simulator, the simulations need to be matched against real-world experimental results. We can estimate the power efficiency of a perfect PIN device with e-beam penetration at 17 keV at this point

$$Max.power\ efficiency = 0.514 * 0.27 \rightarrow 0.1388, \quad (6)$$

where 51.4% is the amount of electron energy falling within the i-GaN region (which has the potential to be collected, as previously described) and 27% is the maximum betavoltaic current efficiency for GaN. This leads to a highest possible PCE of around 14%, not taking into account device defects/traps and contacting deficiencies (which will be taken into account later).

The device simulations are run with perfect, defect-less device materials, while scaling the magnitude of the absorption rate given in Equation 5, until the simulation results give the device efficiency predicted in Equation 6. At this point, defects and traps can then be added to the model (if they are known) in order to better calibrate the expected device performance. The corresponding dark and illuminated I-V curves from the simulated device will next be used for our series and shunt resistance model, allowing us to model the effects related to contact inefficiencies.

Device Contact Simulations

In order to better take into account defects introduced into the device by recombination and issues introduced by the contacts, the ideality of the real-world version needs to be matched to the simulated device. We used this information to scale the simulated dark I-V curve to more accurately mimic the experimental device using the following ideal diode equation:

$$Id = Is * \left\{\exp\left(\frac{q*Vd}{n*k*T}\right) - 1\right\}, \quad (7)$$

where Is is the saturation current, q is the electron charge, n the ideality factor, k is Boltzmann's constant, and T is the temperature (300 K).

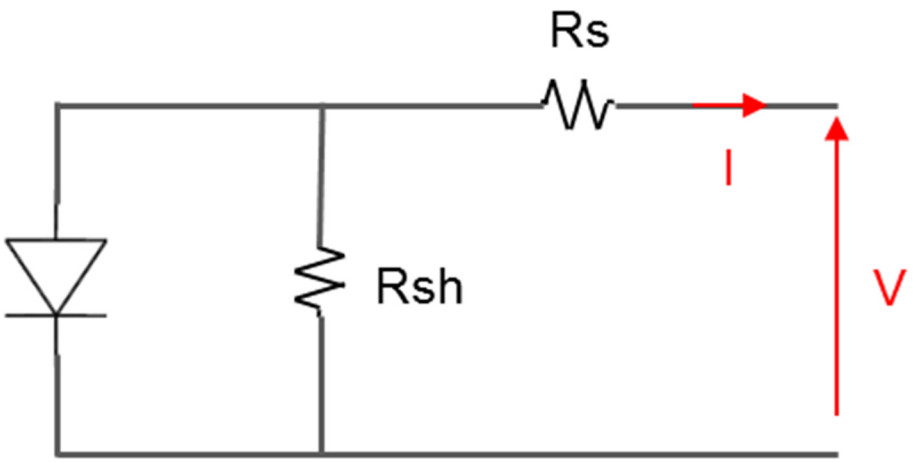

Figure 9: Single diode series and shunt resistance model.

Additional defects are introduced by the contacts that can be modeled as shunt and series resistances that were not already taken into account with the ideality factor (n), as can be seen in Equations 8 and 9 and Figure 9:

$$I = Id * \frac{Vd}{Rsh}, \quad (8)$$

$$V = \left(1 + \frac{Rs}{Rsh}\right) * Vd + Id * Rs, \quad (9)$$

Here, Rs represents the total series resistance of the device, Rsh is the total shunt resistance, and Id and Vd are the ideal IV-curve current and voltage, respectively.

The results of this model match up well with effects previously described in literature, [59] where the shunt resistance has a large impact in the lower voltage range, while effects due to series resistance dominate in the higher voltages (although we obtained the model by first modeling the device as an ideal diode with measured ideality and then applied the series and shunt resistance models). The threshold voltage drop with increasing series resistance also matches up well with literature studying the effects of these resistances. [60]

Note that this model can be further refined by using a two- or three-diode version instead of only one diode (as in Figure 9), depending on the level of accuracy needed for the IV-curves. Additionally, an illuminated model can be made even more accurate by matching it to experimental IV-curves under similar-power illumination (such as SEM illumination to improve the quality of a Ni-63 model).

Comparing Simulations to Experimental Data

In Figure 10, we see the original, device simulation IV-curve as the dashed blue line. The red, dashed line is the experimental dark IV-curve with the device undergoing no beta particle bombardment, while the solid red line is the ideal diode equation scaled to take series and shunt resistances (of 9.4 Ω and 1.1 MΩ, respectively) into account. These values were specifically chosen to best fit the experimental results.

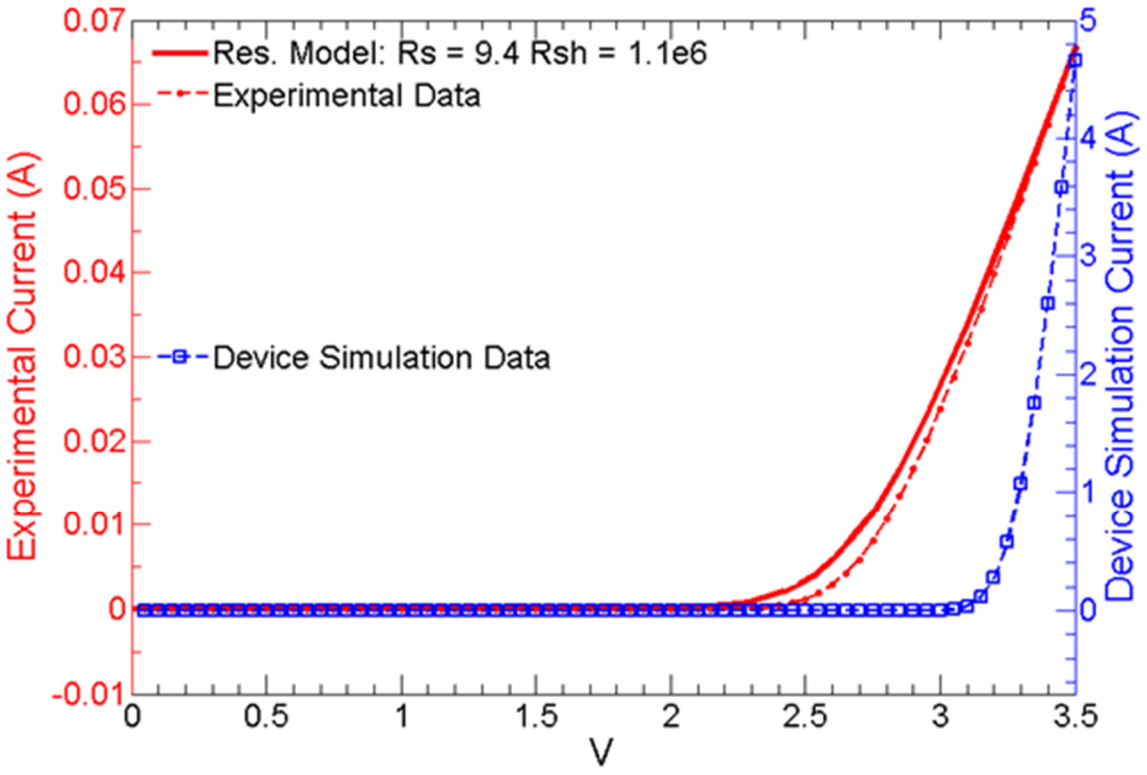

Figure 10: Dark I-V fitting curves—simulated vs experimental data.

Now that we have created a model that also reflects the inefficiencies introduced by the contacts, we can model the beta-illuminated conditions of the device. The simplest way to do this is to take the predicted Isc by the device simulations for a given input power and combine it with the series and shunt resistance model's dark I-V curve, as described previously.

These simulation results can then be compared to results obtained experimentally. For the following experiments, the sample was mounted onto a commercial holder with two probes for the e-beam bombardment measurements. The probes on the sample were connected to an output circuit with a Keithley 4200 for measuring the I-V behavior of the

device during bombardment. Several beam energies were tested and the ones with values close to Ni-63 were then selected, as presented in Figure 11.

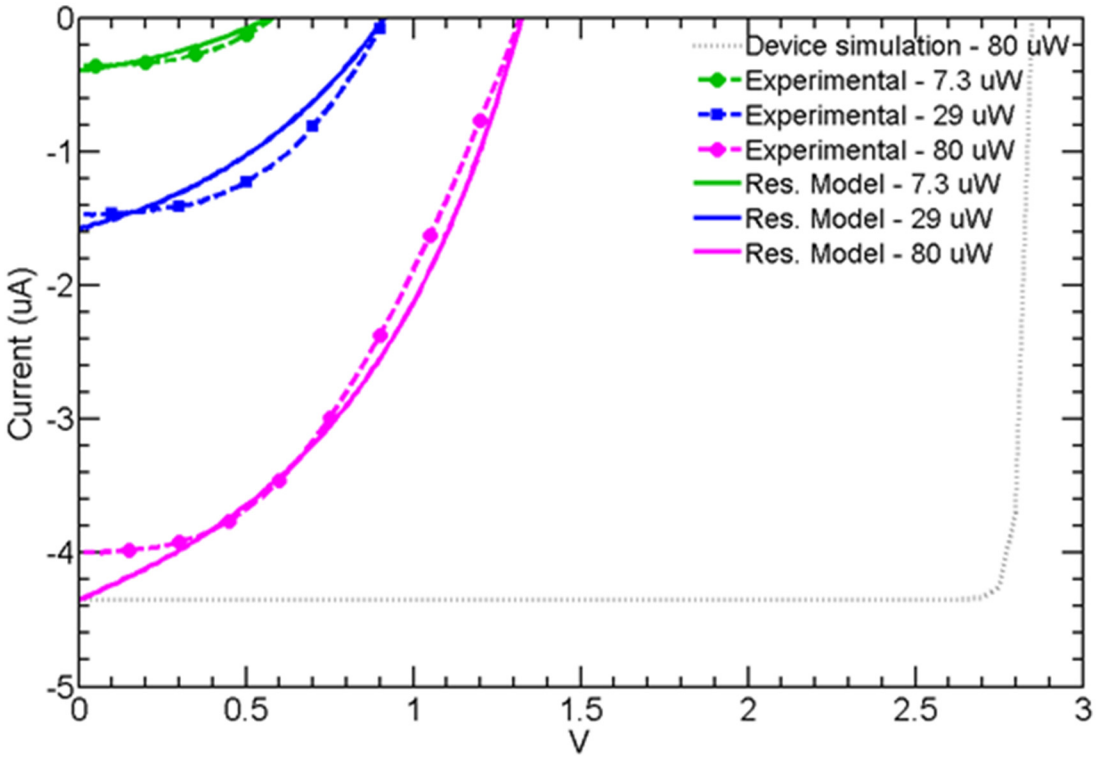

Figure 11: Comparison of modeled illuminated curves and experimental illuminated curves. Device simulation illuminated curve at 80 uW provided for comparison to resistance model.

Here, we can see the green dashed line is the experimental IV-curve with 7.3 uW of energy introduced via e-beam (at 17 keV), the blue dashed line is experimental with 29 uW, and the purple dashed line is experimental with 80 uW. The solid, colored lines are the final, simulated approximations of the device for each respective input energy. The dashed gray line shows the raw device simulation data for 80 uW of power introduced, which assumes a near-perfect device, before the resistance model is added—compare this with the solid, purple line, which additionally adds the series and shunt resistance model.

We can also see this expressed numerically in Table 1. In the ideal simulated diode (directly from the device simulations), we have a high open-circuit voltage mainly because it has no defects at all, not even from parasitic resistances in the contacts. We can see the difference after adding the ideality and resistance models to the ideal simulated diode, where the open-circuit voltage drops from 3 V to 1.3 V. Both the experimental and simulated resistance models expect around 4 uA at 0 V applied to the device and 80 uW of power from the e-beam. With an open-circuit voltage of around 1.3 V, the model and experiments show a device power expected to be over 2 uW (and thus an efficiency of around 3%).

Table 1: Illuminated electrical characteristics at 80 uW power deposited in the sample. "Sim–Ideal" shows the expected performance based on device simulations, "Sim–Resistance" is after the resistance model has been applied to the device simulation model, and "Experimental" is the experimental results.

	Sim. – Ideal	Sim. – Resistance	Experimental
Isc (uA)	4.34	4.34	4.03
Voc (V)	3.03	1.3	1.3
Device Power (uW)	12.43	2.34	2.33
Fill Factor (%)	94.5	41.5	44.4
PCE (%)	15.54	2.93	2.91

Table 2: Illuminated electrical characteristics with simulated Ni-63 source at 13.6 uW power.

	Sim. – Ideal	Sim. – Resistance
Isc (uA)	0.28	0.28
Voc (V)	2.95	0.44
Device Power (uW)	0.78	0.068
Fill Factor (%)	94.3	54.7
PCE (%)	5.7	0.5

Using the Ni-63 absorption profile, described previously, under 13.6 uW of power (5 GBq of activity) instead of the SEM profile, we get the results seen in Table 2. This model assumes a stacked PIN design with energy collected in both a top and bottom PIN device. This model takes into account backscatter off of the sample surface, as well as the self-absorption of electrons within the Ni-63 source. With an ideal diode (no defects or parasitic resistances), we expect a high open-circuit voltage of 2.95 V, while this drops to only 0.44 V when we add in defects due to ideality and parasitic resistances. This is responsible for dropping the efficiency from 5.7% to only 0.5%, resulting in an output power of around 68 nW.

Next, the model was matched to an experiment done by Cheng et al. [14] in order to test its accuracy with a device that experimentally underwent Ni-63 bombardment. This experiment was chosen in particular, because it matches closely to the specifications of the project that we are working on and developing a device for and is taken as state-of-the-art for GaN-based, Ni-63-sourced betavoltaic batteries.

Table 3: Illuminated electrical characteristics with Ni-63 source at 50 nW power.

	Sim. – Ideal	Sim. – Resistance	Experimental[14]
Isc (pA)	617.6	617.6	568
Voc (V)	2.58	1.7	1.64
Device Power (nW)	1.59	1.05	0.93
Fill Factor (%)	54.8	54.3	53
PCE (%)	1.74	1.14	0.98

In Table 3, we see that, after our resistance model is applied to the device simulations of their device, the model's expected efficiency is 1.14%—only 0.16% higher than the experimental efficiency of 0.98%. Note that, since the material properties related to the iron doping of their intrinsic region were not fully detailed, values from literature [61, 62] were used instead. The electron mobility of their iron-doped material was also assumed to be state-of-the-art quality, which explains why the model overestimated the expected short-circuit current and thus device power.

Simulations Summary

In conclusion, we have demonstrated a betavoltaic model that involves emission of the most probable beta particle energy from Ni-63 (17 keV) directly into a GaN-based PIN device. The model takes into account losses through contacting metals, losses by energy absorption efficiency of electrons into GaN-like materials, losses due to electron-hole pairs that are created outside of the intrinsic region of the device, and defects due to recombination and parasitic resistances (ideality factor and series-shunt resistances).

We have demonstrated that the model matches well with experimental results of a fabricated device in dark conditions and under SEM-illumination. We have also

demonstrated that the model matches well with Ni-63 bombardment results from literature. In the end, we expect that the device could operate with an efficiency and short-circuit current that are within a 10% margin of error.

CHAPTER 3

DEVICE AND MATERIAL LONGEVITY

In order to verify the longevity of our GaN PIN while undergoing a 100 year dosage of Ni-63 beta particles, an experiment was carried out using an SEM to mimic the Ni-63 material. There are various measurements that can be performed to determine electrical and physical changes of a material from bombardment. For instance, CL measurements can determine if there were any changes in the device absorption or emission profiles. AFM and SEM results determine if there are any physical changes in surface roughness. The IV/CV curves tell us if there are any electrical changes in device performance due to bombardment. TLM measurements indicate changes in contact resistance, and DLTS measurements inform us of any changes in defect densities throughout our device.

Ni-63 Dose-Equivalence Calculations

In order to determine how long a sample needs to be bombarded for under SEM illumination in order to achieve an equivalent dosage in Ni-63, the following equations were used:

$$J_{SEM} = \frac{I_{SEM}}{SA_{beam}} \quad \left(\frac{C}{s* cm^2}\right), \quad (10)$$

$$J_{Ni63} = \eta * q * \frac{A}{2} \quad \left(\frac{C}{s* cm^2}\right), \quad (11)$$

As described in Equation 10, we can see that J_{SEM} is the current density calculation for the SEM normalized over a 1 cm^2 surface area, while I_{SEM} is the SEM

specimen beam current (in amps, or C/s) and SA_{beam} is the surface area of bombardment (the size of the SEM beam in cm^2).

In Equation 11 we have the current density calculation for Ni-63 over a 1 cm^2 surface area. Here, A is the radioactivity of Ni-63 (for example, 5 GBq in our experiments), which is halved since only particles in the downward direction would enter our sample (while the other half would be emitted away from our sample, as in the case of the SEM bombardment), η is the source efficiency (fraction of beta particles that are not lost due to self-absorption within the source), and q is the elementary charge (1.602 x 10^{-19} C).

Recall that the density of Ni-63 is 8.91 g/cm^3 and the specific activity of Ni-63 per gram is 2.2 x 10^{12} Bq/g. This corresponds to around 1.96 GBq/um*cm^2, and thus 2.55 um of Ni-63 will be required for a 1 cm^2 surface area to achieve 5 GBq. Finally, Figure 8 tells us that we can expect a source efficiency of around 20% for 2.55 um of Ni-63 (and so η = 0.2).

$$Equiv_{Ni63}(t) = \frac{J_{SEM}}{J_{Ni63}} * t, \quad (12)$$

Finally, in Equation 12 we can see the conversion between SEM and Ni-63, where we input an amount of time, t, for SEM bombardment and get an equivalent-dosage amount of time for Ni-63.

Material Longevity Bombardments

The first bombardment experiments performed were designed to see if the GaN material itself degrades over a long exposure to beta particles. An electron energy of 25 keV was used for these experiments with a beam current of 5450 pA, and bombardment was done over an area of 458 x 345 um^2, using what would be the equivalent of a 2.5

year dose of beta particles (30 minutes under SEM). These experiments were performed on n-type, intrinsic, and p-type GaN.

As can be seen in Figure 12, the CL profile of i-GaN bombardment remains unchanged for the most part, as there is no noticeable change to magnitude or shape. Additionally, referring to Table 4, we can see that there is no noticeable change to material mobility, resistivity or bulk concentration. As discussed previously, these results fall in line with what we expect for SEM bombardment at this level of SEM energy.

Similar results are seen with n-GaN, as can be seen in Figure 13, as there is again no significant change in either shape or magnitude during bombardment. These results are confirmed with IV results as seen in Table 5, where there is again no major change seen in material mobility, resistivity or bulk concentration. This is again consistent with the behavior we expect from SEM bombardment of n-GaN at these SEM energy levels.

Finally, we can see in Figure 14 that p-GaN does not show any major changes to CL intensity or shape during this 30 minute bombardment. We do see some minor variations in IV characteristics, seen in Table 6, though such a small variation in these parameters could likely be due to the poor quality that indium contacts make when paired with p-type GaN, which results in small fluctuations between each measurement (sometimes up to a 10% fluctuation). Such a small variation was not seen to have any noticeable impact on device performance.

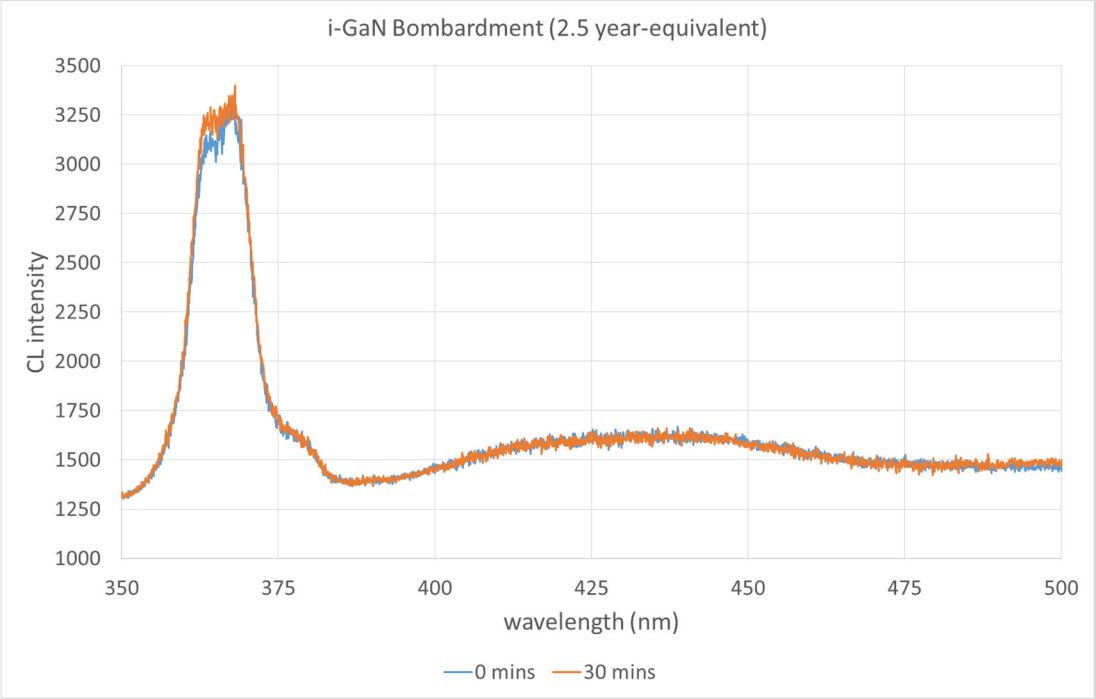

Figure 12: i-GaN 5x5 CL before and after bombardment

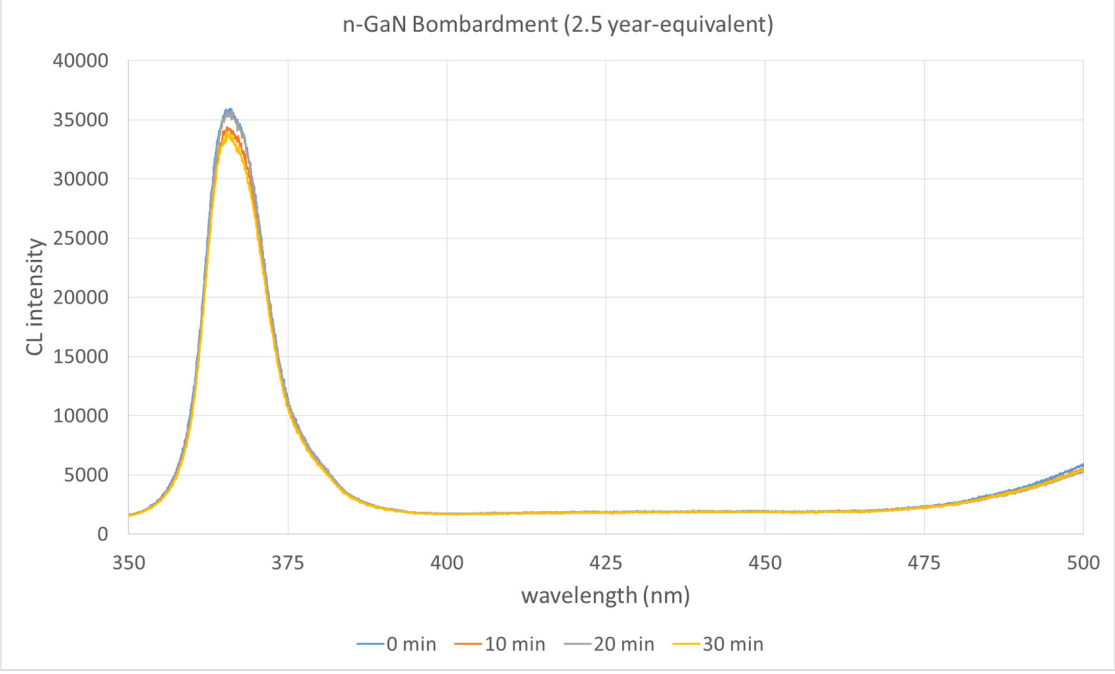

Figure 13: n-GaN 5x5 CL before and after bombardment

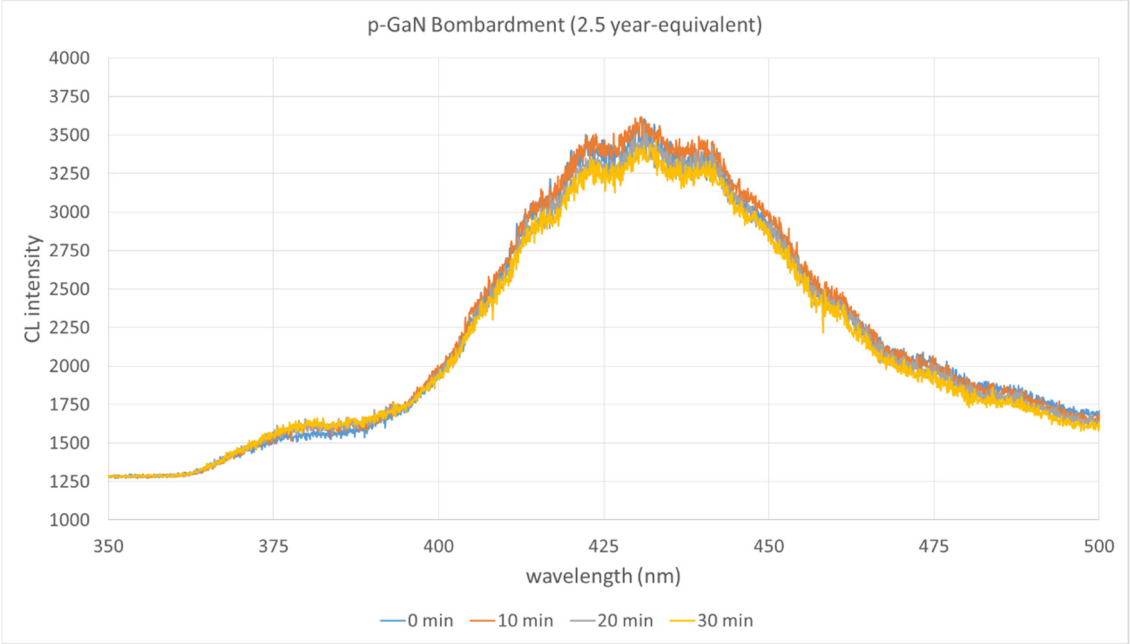

Figure 14: p-GaN 5x5 CL before and after bombardment

Table 4: i-GaN 5x5 electrical properties before and after 30 minutes of SEM irradiation.

	Mobility (cm^2/Vs)	Resistivity (Ωcm)	Bulk Conc. (cm^{-3})
No irradiation	258.89	0.328	-7.346×10^{16}
30' irradiation	262.30	0.325	-7.316×10^{16}
% change	1.32%	-0.91%	-0.41%

Table 5: n-GaN 5x5 electrical properties before and after 30 minutes of SEM irradiation.

	Mobility (cm^2/Vs)	Resistivity (Ωcm)	Bulk Conc. (cm^{-3})
No irradiation	303.88	0.0129	-1.592×10^{18}
30' irradiation	308.87	0.0129	-1.569×10^{18}
% change	1.64%	< -0.1%	-1.44%

Table 6: p-GaN 5x5 electrical properties before and after 30 minutes of SEM irradiation.

	Mobility (cm^2/Vs)	Resistivity (Ωcm)	Bulk Conc. (cm^{-3})
No irradiation	13.86	2.953	1.525×10^{17}
30' irradiation	13.04	3.196	1.562×10^{17}
% change	-5.92%	8.23%	-2.43%

Considering that literature postulates that p-GaN material sometimes sees changes in its CL properties after exposure to SEM bombardment (though typically with higher electron energies than what we see with Ni-63, and often with poorly-annealed p-type material), we decided to perform an extended SEM bombardment over an area of 230 x 173 um^2 for p-GaN (same beam parameters), which had a Ni-63 equivalence of 36 years.

These results can be seen in Figure 15, where we have mapped the defect band peaks (in blue) over time, and the GaN peaks (in orange) over time. Although we see minor variations throughout the duration of the bombardment for both peaks, the variations appear to be insignificant. In particular, our GaN peak does not appear to have any real changes to peak magnitude, nor does the magnitude seem to follow any trend.

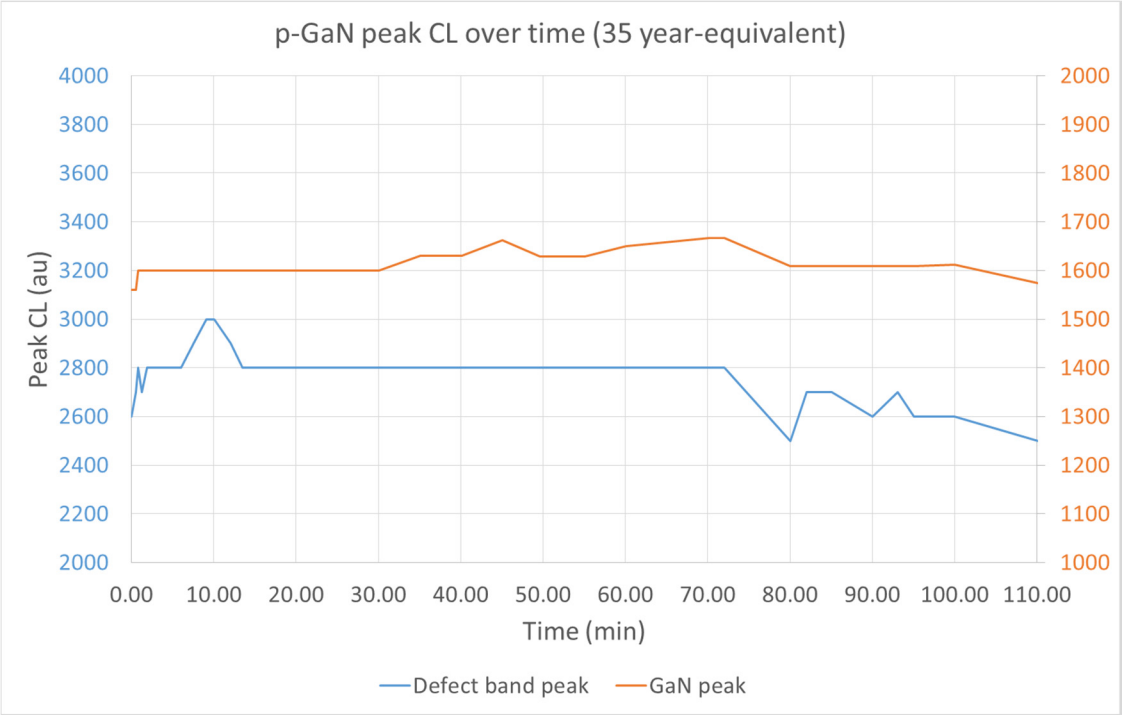

Figure 15: p-GaN 5x5 CL defect band peak (blue) and GaN peak (orange) over 110 minutes

In summation, we have seen that for n-type, intrinsic and p-type GaN materials, we have not seen any significant changes in CL shape or magnitude, material mobility, resistivity or bulk conductivity over a 30 minute SEM bombardment (2.5 year Ni-63-equivalence). Especially with p-GaN, which was further bombarded for a total of 110 minutes over a smaller area (a 36 year Ni-63-equivalence), we saw no noticeable changes to the CL shape or magnitude. As discussed before, literature shows that changes are only significantly noticed with either high beam energies (especially over 1 MeV) or sometimes with poorly-annealed (or not annealed) p-doped GaN.

Contact Longevity Bombardments

Additional bombardments were performed to determine the effects of beta particles on device contacts and the contact interface. Since our device design assumes our beta particles will be penetrating the thin p-GaN spreading layer, experiments were carried out using Ohmic contacts on p-GaN. IV/CV curves, CL, AFM and SEM imaging were all performed to determine if any changes would occur.

The contacts chosen were saw-shaped diodes, with the Ohmic side (comprised of 10 nm/10 nm Ni/Au) appearing a gold color in Figure 16 and the Schottky side (comprised of 50 nm Ni) appearing white.

An electron energy of 20 keV, along with an SEM specimen current of 5700 pA and a beam area of 437 x 328 um^2, resulting in a dose-equivalence of 34 years' worth of Ni-63 was injected through the device contacts. An optical microscope image of the p-GaN contacts can be seen in Figure 16, where the yellow box denotes the targeted area for bombardment (though the beam drifts over time, so it may sometimes fall slightly outside this area).

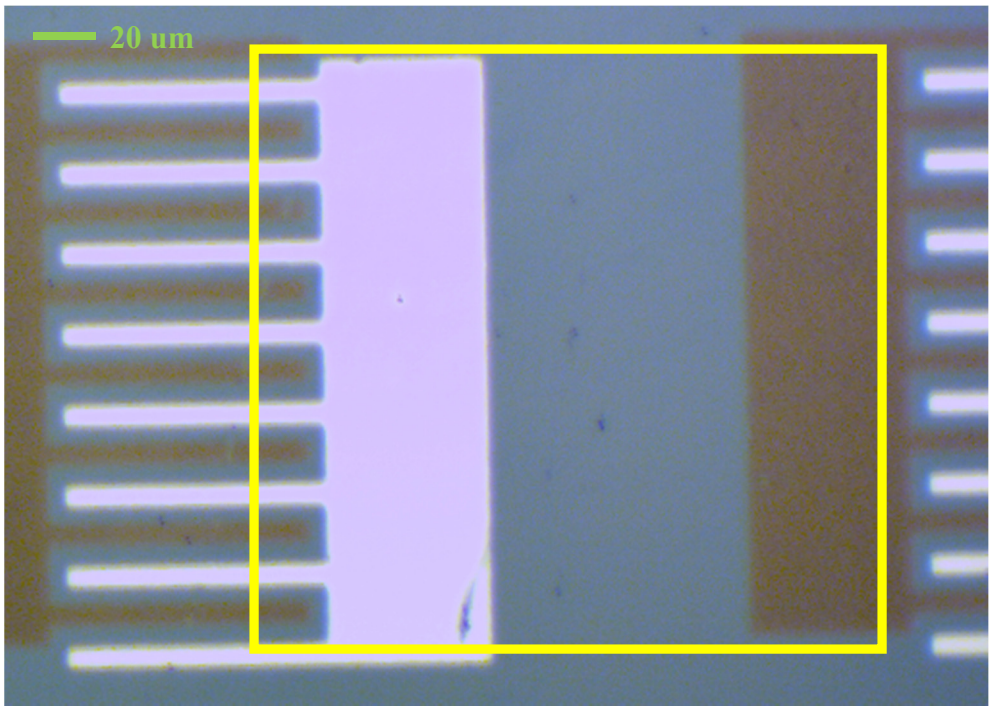

Figure 16: Optical microscope image of p-GaN contact bombardment – before bombardment. Yellow box roughly denotes targeted bombardment area.

A visual inspection can be seen in Figure 17 through Figure 20 via SEM image results. These figures feature a progression of SEM images starting with no bombardment and finishing with 6 hours of bombardment having been completed.

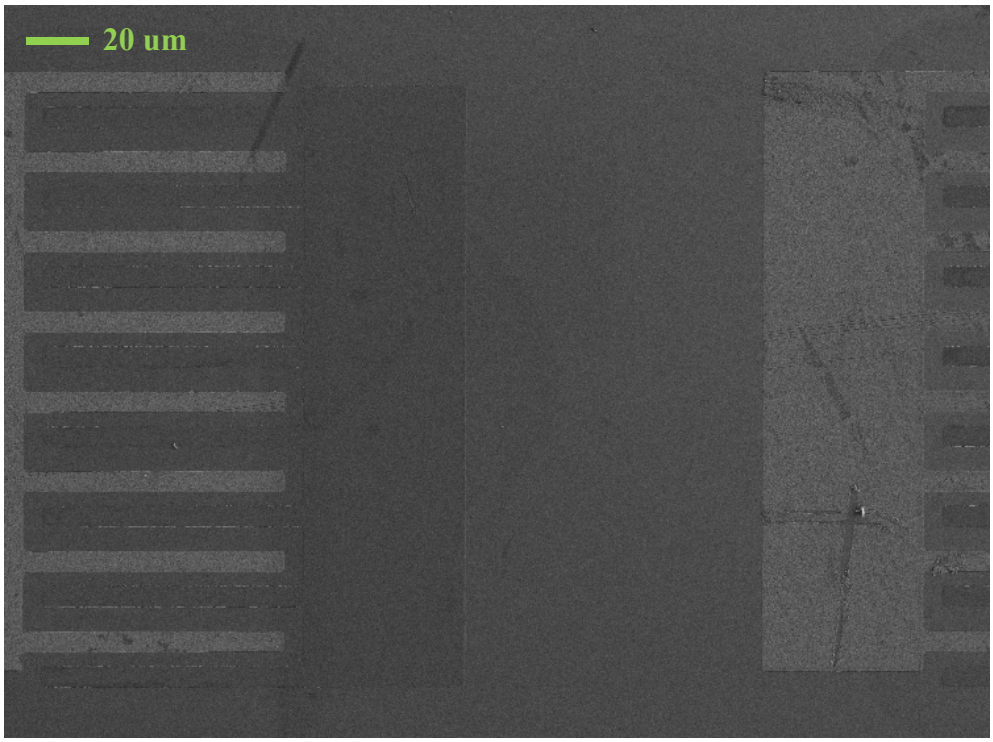

Figure 17: SEM results for p-GaN contact bombardment – before bombardment.

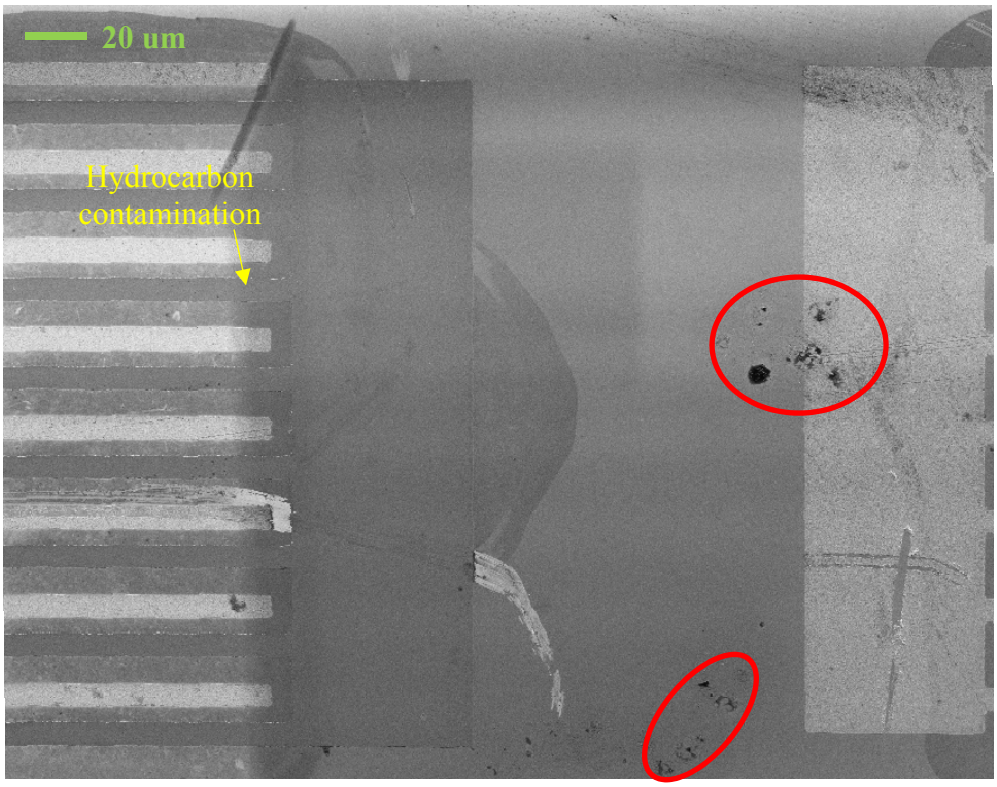

Figure 18: SEM results for p-GaN contact bombardment – after 2 hours. Yellow arrow points out hydrocarbon contamination, causing darkened area in SEM. Red, circled areas denote additional hydrocarbon contamination due to handling of sample.

In Figure 18, after 2 hours of bombardment, a darkened area is clearly seen where the bombardment took place, pointed out by a yellow arrow. This is likely due to hydrocarbon contamination from the SEM beam, and appears to be only superficial, not having an impact on device properties or performance (as we will see). The red circles denote areas of additional hydrocarbon contamination, unrelated to the bombardment of electrons. Other than the darkening in the bombardment area, no clear changes are noted in contact quality.

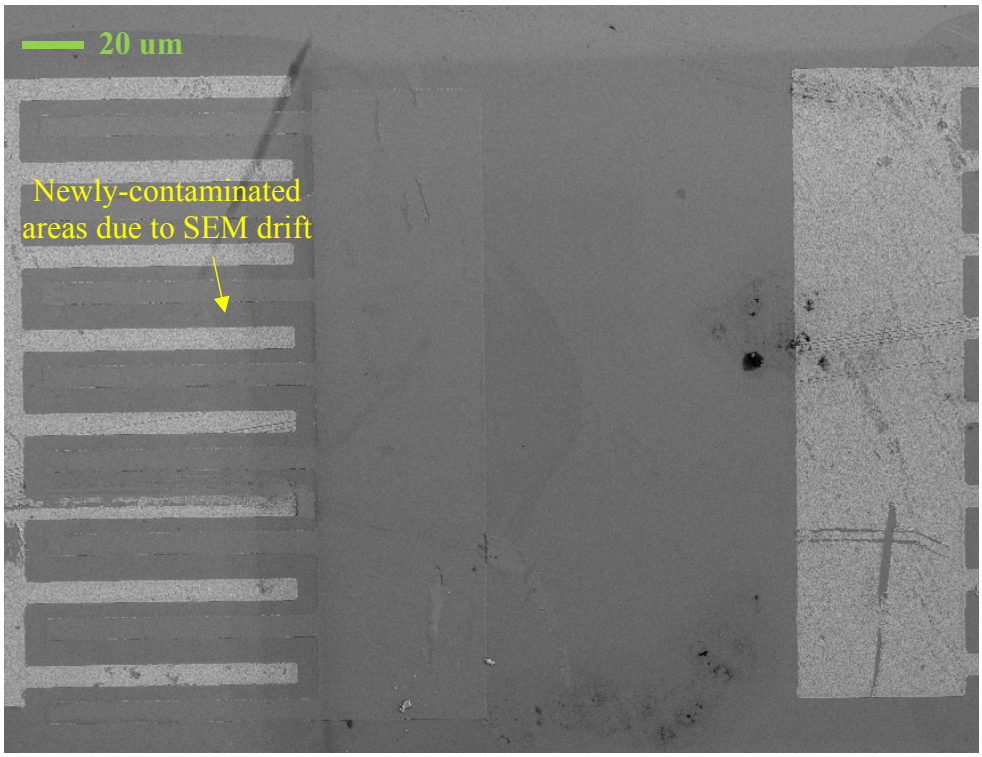

Figure 19: SEM results for p-GaN contact bombardment – after 4 hours. Yellow arrow points out a sliver of bombarded area with slightly less darkening than the main bombardment area. This is likely due to beam drift over time.

Because of the slight drift in the SEM over time, we can see in Figure 19 a sliver of newly-contaminated material with slightly less darkening than the main bombardment area, as pointed out by the yellow arrow. Otherwise, no new changes can be seen in this figure that can be attributed to SEM bombardment.

When finally comparing this with Figure 20, after 6 hours of bombardment, we can confirm that there are no visible signs of contact degradation. Again, the only change here is the darkening of the material due to hydrocarbon contamination from SEM bombardment.

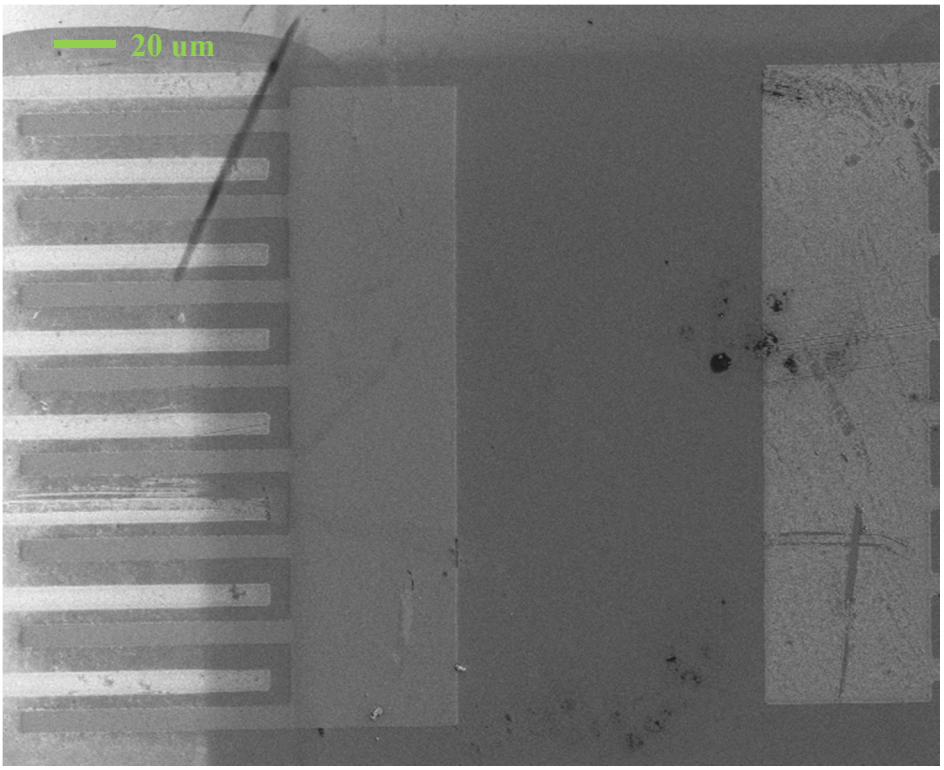

Figure 20: SEM results for p-GaN contact bombardment – after 6 hours. Ultimately we can see no visible signs of contact degradation, other than a slight coloration change due to carbon contamination from the SEM beam.

Finally the AFM results for this bombardment can be seen in Figure 21, where (a) denotes the area of the sample before bombardment and has an RMS roughness of around 0.911 nm in the highlighted box, (b) is the same area after 2 hours of bombardment and has a roughness of 0.759 nm, (c) is that area after 4 hours of bombardment with a roughness of around 0.655 nm and (d) is after 6 hours of bombardment with a roughness of 0.755 nm.

From these results we can see (both visually and numerically) that the p-type pads did not undergo any significant degradation or abrasion from the e-beam bombardment, since the roughness stayed essentially the same (in the general range of around 0.7 or 0.8 nm RMS roughness).

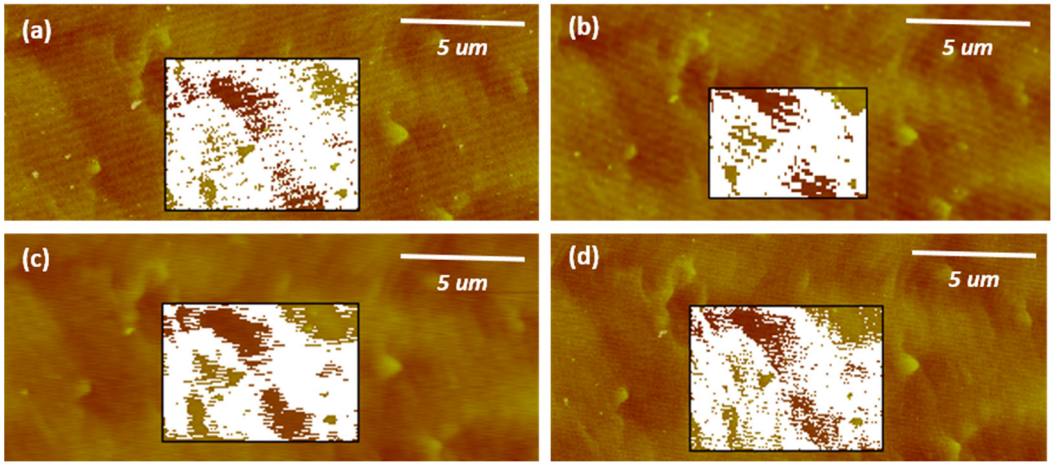

Figure 21: AFM results for p-GaN contact bombardment – (a) before bombardment, (b) after 2 hours of bombardment, (c) 4 hours, (d) 6 hours.

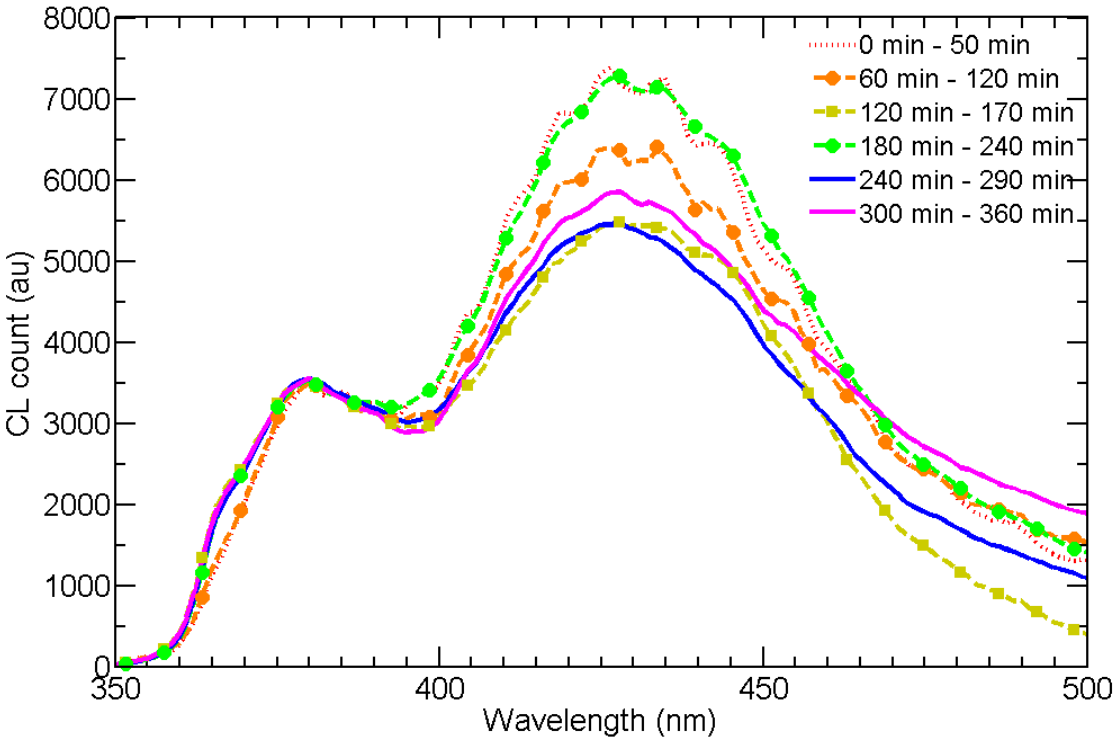

Figure 22: Cathodoluminescence results for 6 hour p-GaN contact bombardment.

As can be seen in Figure 22, the CL profile and magnitude of the sample does not appear to change throughout the duration of the bombardment. There are noticeable

fluctuations in the CL intensity in the defect band, though this can be explained as reflections and interference from the metal contact, and there are no obvious trends in the magnitude.

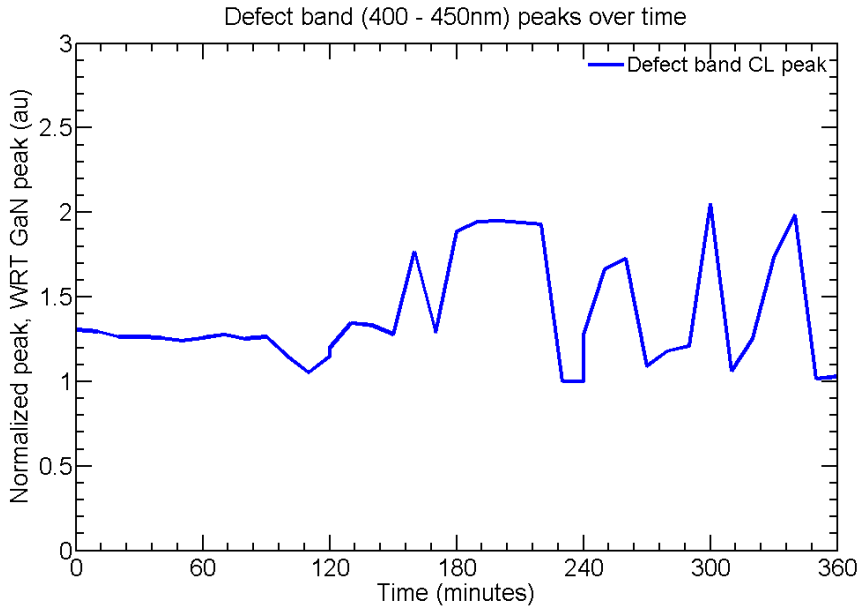

Figure 23: Normalized defect CL peak with respect to GaN peak (AU) for 6 hour p-GaN contact bombardment

Figure 23 shows the normalized defect CL peak with respect to the GaN peak for the 6 hour p-GaN contact bombardment. Though the data begins fluctuating after around 2 hours of bombardment, the data still stays around the same magnitude and shows no clear trend in either direction. This coincides well with the data from Figure 22, which shows no trend in the defect band CL intensity, and verifies our expectations of no real significant trend from the 110 minute p-GaN material bombardment in Figure 15.

In Figure 24 and Figure 25 we can see the IV and CV curves for this device, respectively. Although there is a variation in the overall magnitude of the IV curve, the magnitude change has no clear trend and appears to be due to natural variations while performing the measurements.

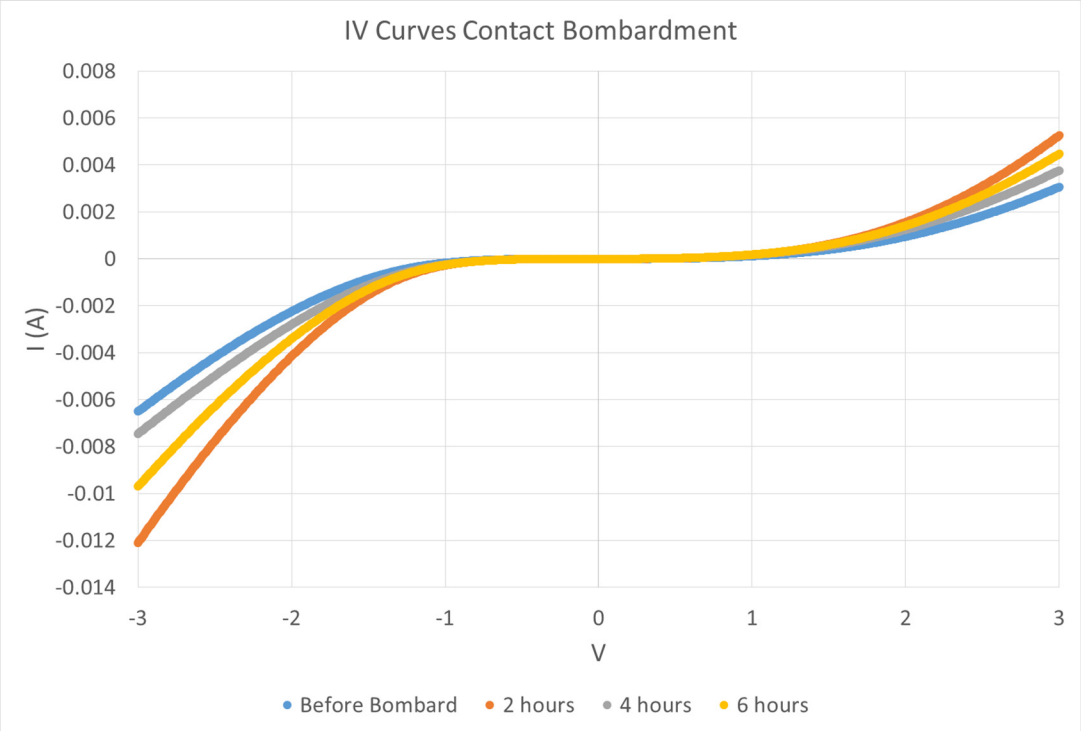

Figure 24: IV Curves for 6 hour p-GaN contact bombardment.

Similarly, the CV curves in Figure 25 show essentially no change in shape or significant change in magnitude. Any differences here could easily be explained as fluctuations in the measurements, as even multiple CV measurements in a row often yield similar slight variations. Since the capacitance is so low (due to the lack of a PN junction, thus the only capacitance is due to the contacts), these fluctuations are typical as we are operating at the limits of the probe station machine.

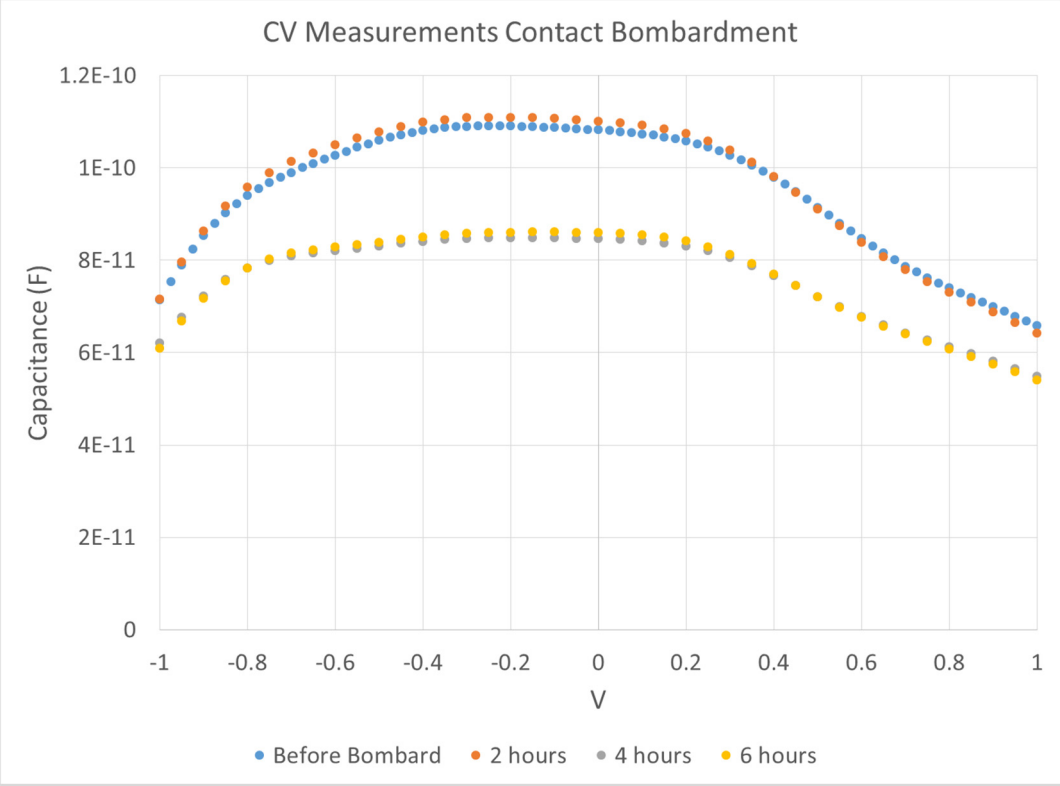

Figure 25: CV Curves for 6 hour p-GaN contact bombardment.

In summary, no significant changes were seen in any of the aforementioned measurements, meaning that both our device and its contacts should be very resilient to Ni-63 beta particles at least for 34 years' worth of Ni-63 exposure.

100 Year Ni-63 Equivalent Bombardment

Finally, bombardments were performed to determine the effects of beta particles on device contacts and the contact interface for a 100 year Ni-63-like dosage. IV/CV curves, CL, AFM and SEM imaging were again all performed to determine if any changes would occur. In this round of bombardments, we did a full bombardment for 10 hours without taking the sample out of the SEM for external characterization (thus limiting the impact of possible sample contamination and measurement-related damages).

An electron energy of 20 keV, along with an SEM specimen current of 5700 pA and a beam area of 437 x 328 um^2, resulting in a dose-equivalence of 102 years' worth of Ni-63 was injected through the device contacts (18 hours of SEM bombardment).

The contacts chosen were again saw-shaped diodes, with the Ohmic side (comprised of 10 nm/10 nm Ni/Au) appearing a gold color in Figure 26 and the Schottky side (comprised of 50 nm Ni) appearing white. This time, both the Ohmic and Schottky side of the contacts were bombarded so that electrical changes in either type of contact could be monitored. The bombarded area is roughly within the area depicted in the yellow box here.

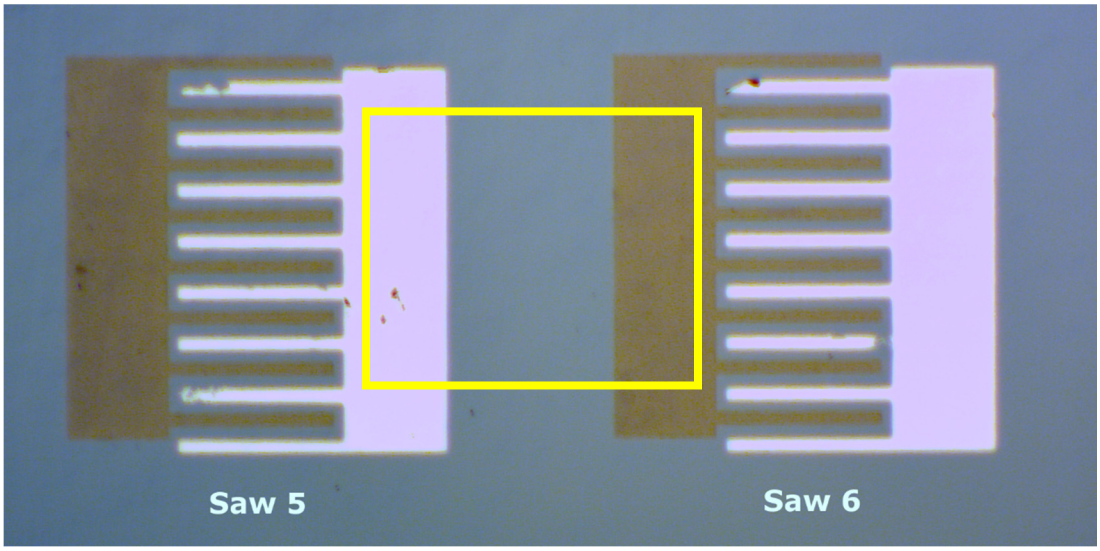

Figure 26: Optical microscope image of p-GaN contact (before bombardment)

The SEM progression during bombardment can be seen in Figure 27 and Figure 28, showing a 126x magnification and 328x magnification, respectively. The most significant change observed here is the hydrocarbon contamination box (appearing as the darkening square between the saw diodes), which was also observed in the previous

bombardments. The higher magnification SEM images show that there are no obvious physical, visible changes that appear to be happening during the 18 hour bombardment.

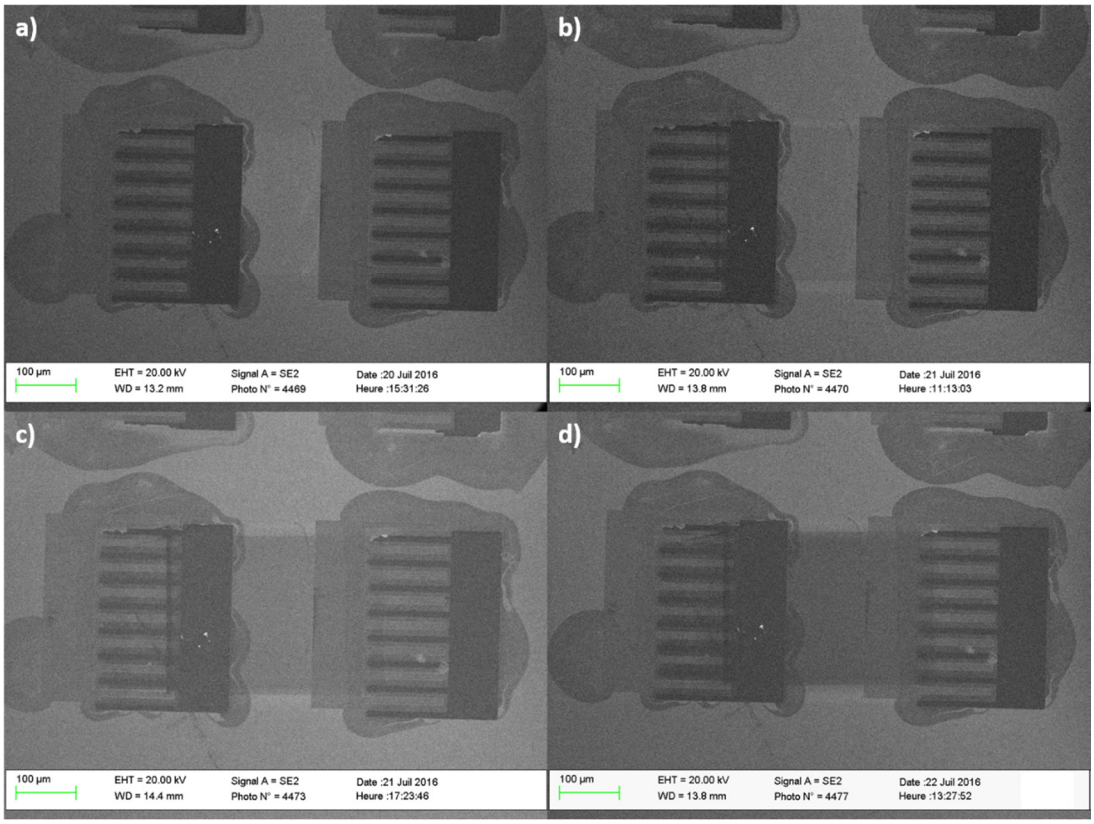

Figure 27: SEM image of p-GaN contact bombardment at 126x – a) before bombardment, b) after 6 hours of bombardment, c) 12 hours and d) 18 hours of bombardment

Similarly, one can observe that there are no major physical changes in surface morphology by AFM inspection. In Figure 29, it is seen that the step height of the Saw 5 Schottky contact showed no real changes in height (51.433 nm before and 51.571 nm after bombardment). This shows that the contact was not worn down via abrasive forces during the 18 hour bombardment.

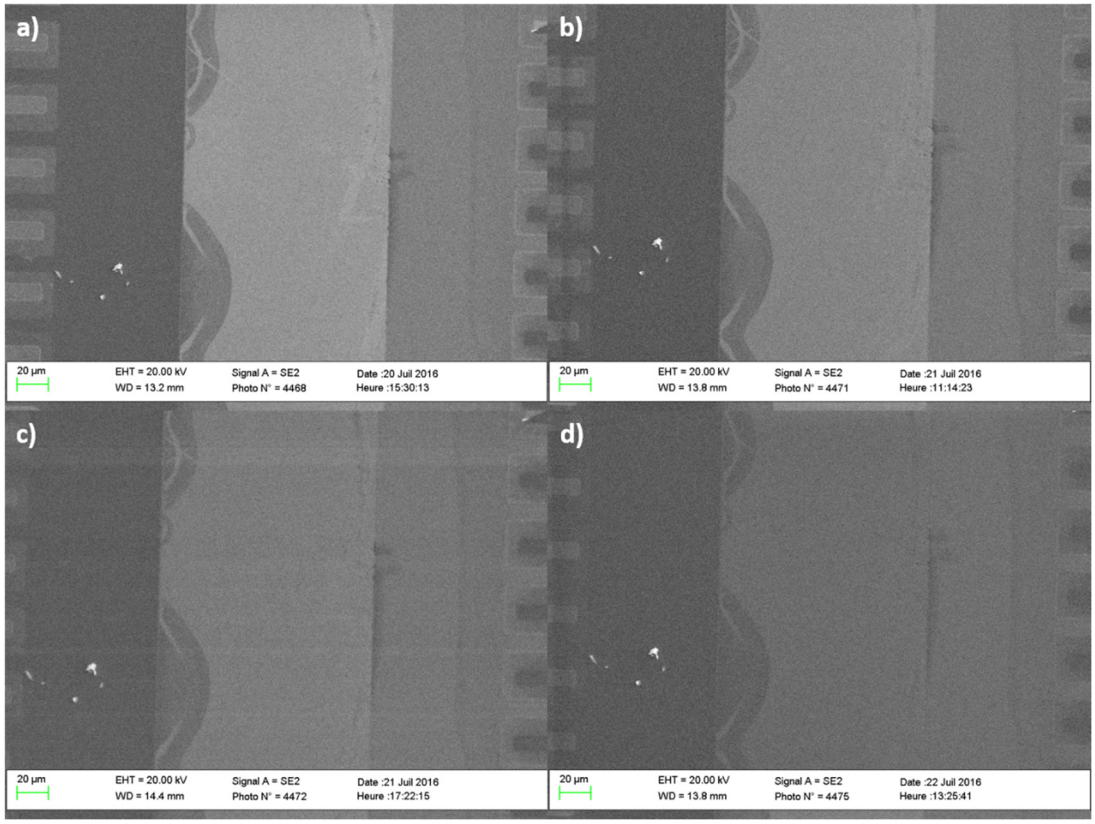

Figure 28: SEM image of p-GaN contact bombardment at 328x – a) before bombardment, b) after 6 hours of bombardment, c) 12 hours and d) 18 hours of bombardment

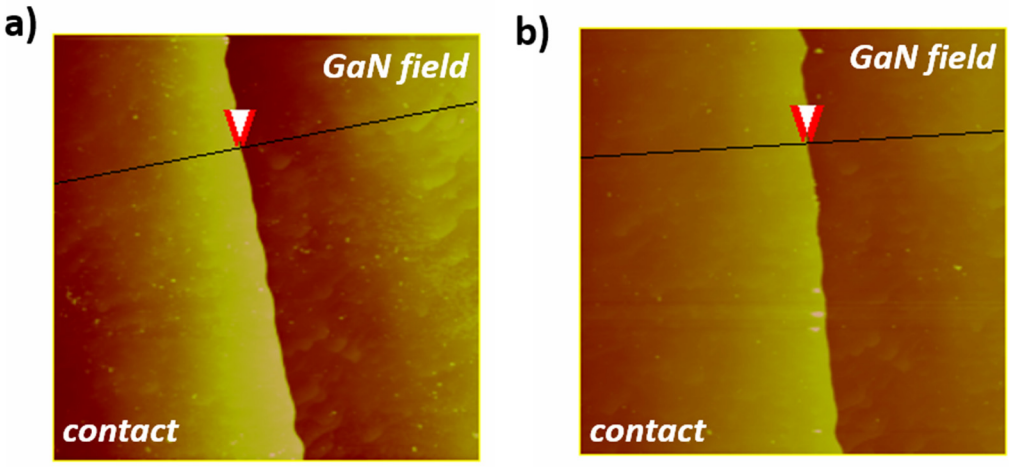

Figure 29: A 30 um x 30 um AFM image of p-GaN contact bombardment– a) step height measurement before bombardment (51.433 nm) and b) step height after 18 hours of bombardment (51.571 nm)

Similarly, Figure 30 shows an AFM RMS roughness measurement on the Saw 5 Schottky contact surface, with no major changes to surface roughness before and after bombardment (2.127 nm vs 2.139 nm roughness, respectively).

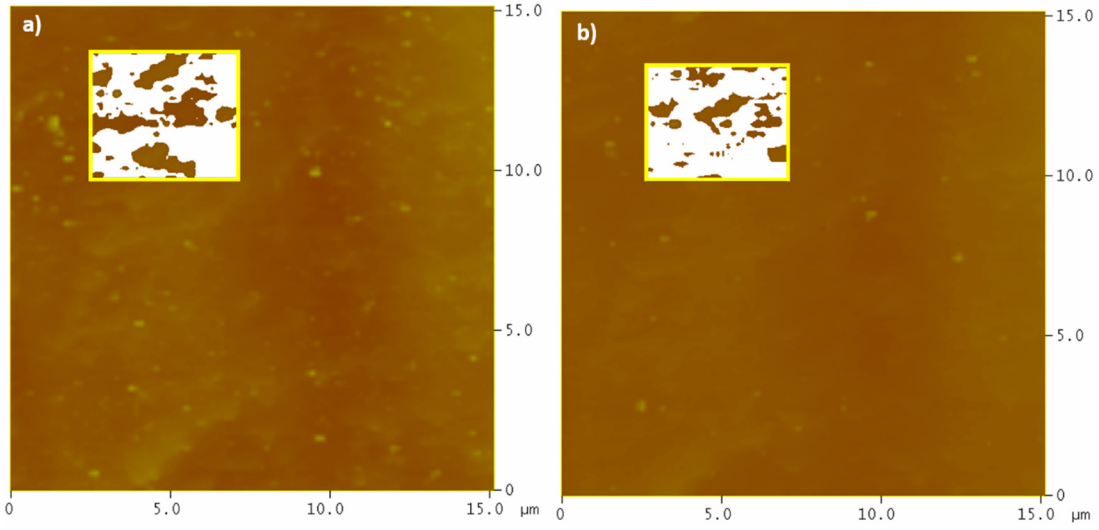

Figure 30: AFM image of p-GaN contact bombardment – contact RMS roughness measurement a) before bombardment (2.127 nm, 1.080 nm inside box) and b) after 18 hours of bombardment (2.139 nm, 0.930 nm inside box)

Finally, Figure 31 shows the AFM RMS roughness measurement on the GaN field between Saw 5 and Saw 6. Although the roughness changes were more pronounced than on the contact, they were less than 1 nm difference (2.297 nm before and 1.696 nm after, or 1.087 nm inside the box before and 0.890 nm inside box after).

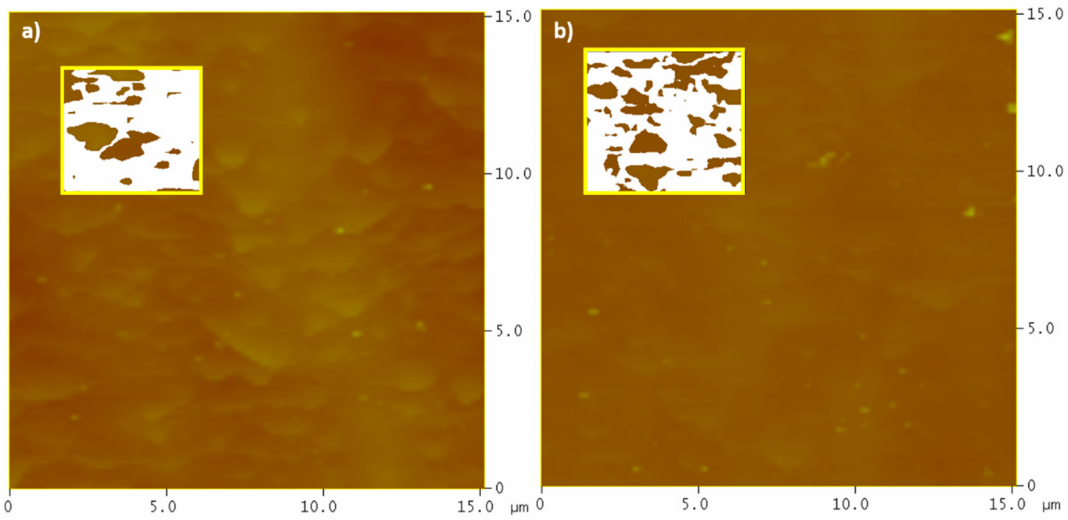

Figure 31: AFM image of p-GaN contact bombardment – GaN field RMS roughness measurement a) before bombardment (2.297 nm, 1.087 nm inside box) and b) after 18 hours of bombardment (1.696 nm, 0.890 nm inside box)

As seen in the 6 hour bombardment results, the CL spectrum of the sample showed no signs of obvious changes throughout the duration of the 18 hour bombardment. This can be seen in Figure 32, which shows constant fluctuations between 450 and 650 detections. There were no observed trends to changes in shape or magnitude during the bombardment.

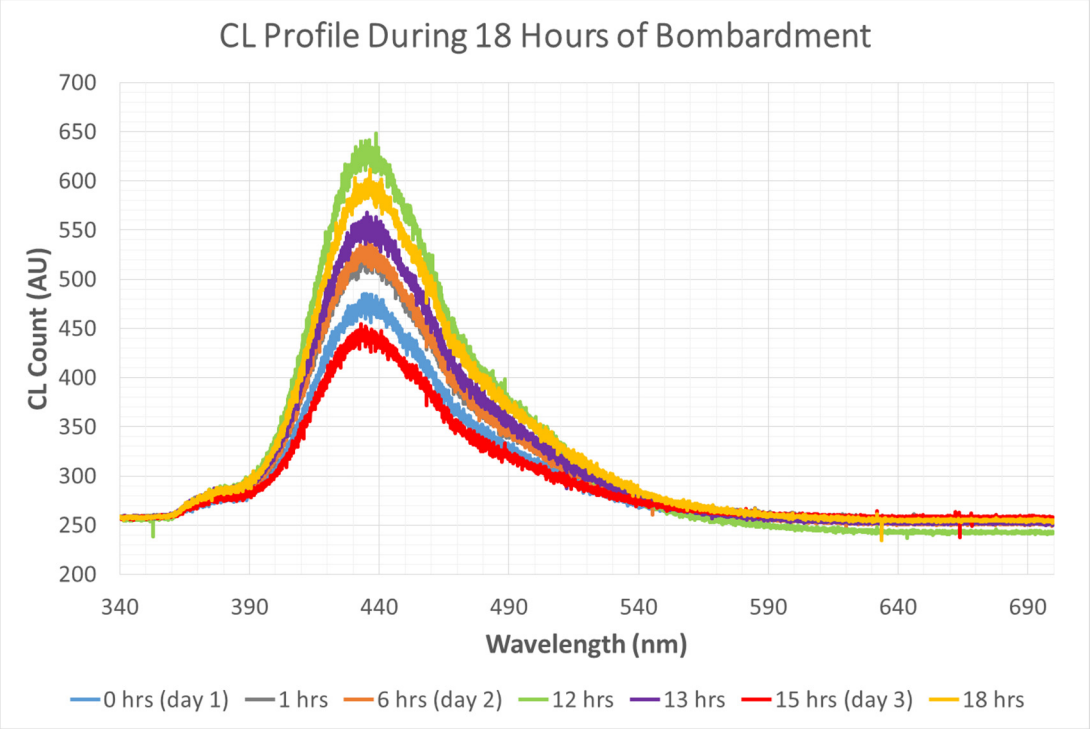

Figure 32: CL image of p-GaN contact bombardment, showing fluctuations between 450 detections and 650 detections at the 440 nm wavelength. Note that 0 hours (day 1 start), 6 hours (day 2 start) and 15 hours (day 3 start) are typically the lowest measurements of the day, most likely because charge builds up on the sample during prolonged bombardment. No changes in shape or peaks are observed.

Finally, the IV/CV characteristics of Saw 5 and Saw 6 were performed, with the IV characteristics seen in Figure 33 and Figure 34, respectively. It is clear here that there were no major changes in the IV properties of either saw diode before and after bombardment, telling us that both Schottky and Ohmic contacts do not experience any significant electrical property degradation throughout a 100 year period of Ni-63-like bombardment.

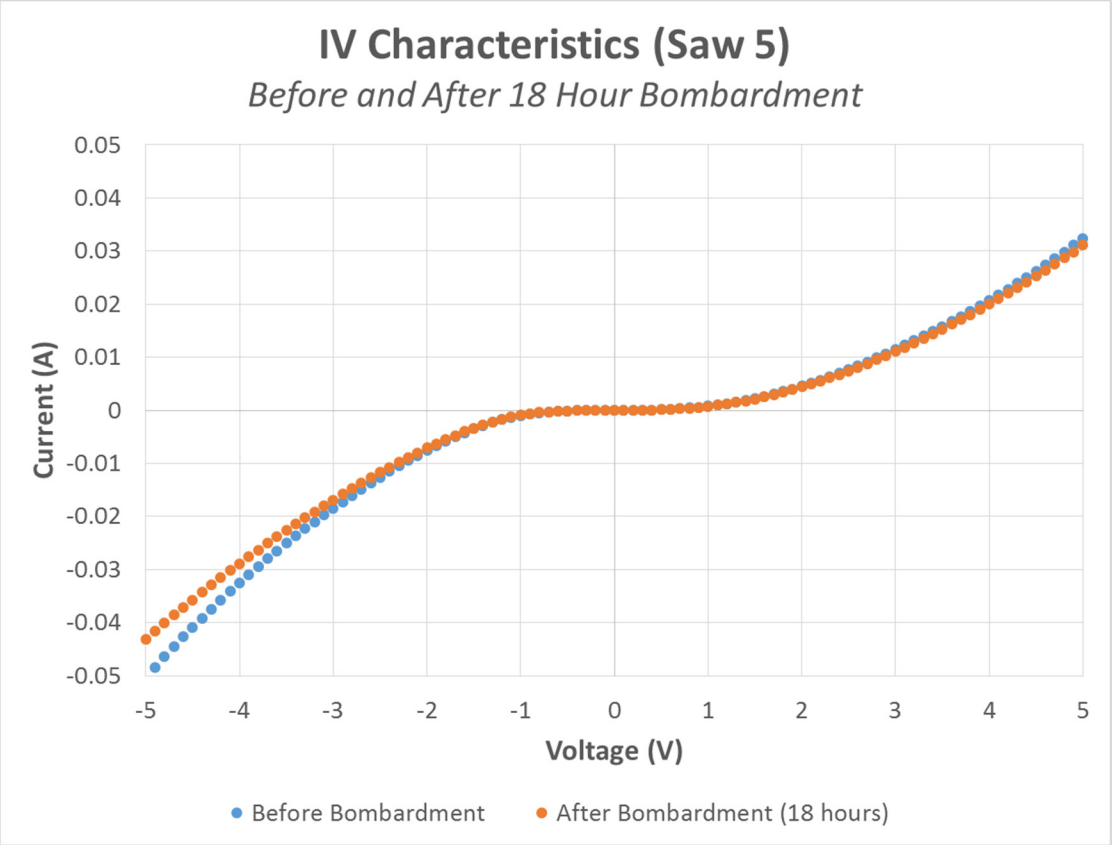

Figure 33: IV characteristics of p-GaN Saw #5 contact bombardment showing no significant change between no bombardment (blue) and the full 18 hour bombardment (orange).

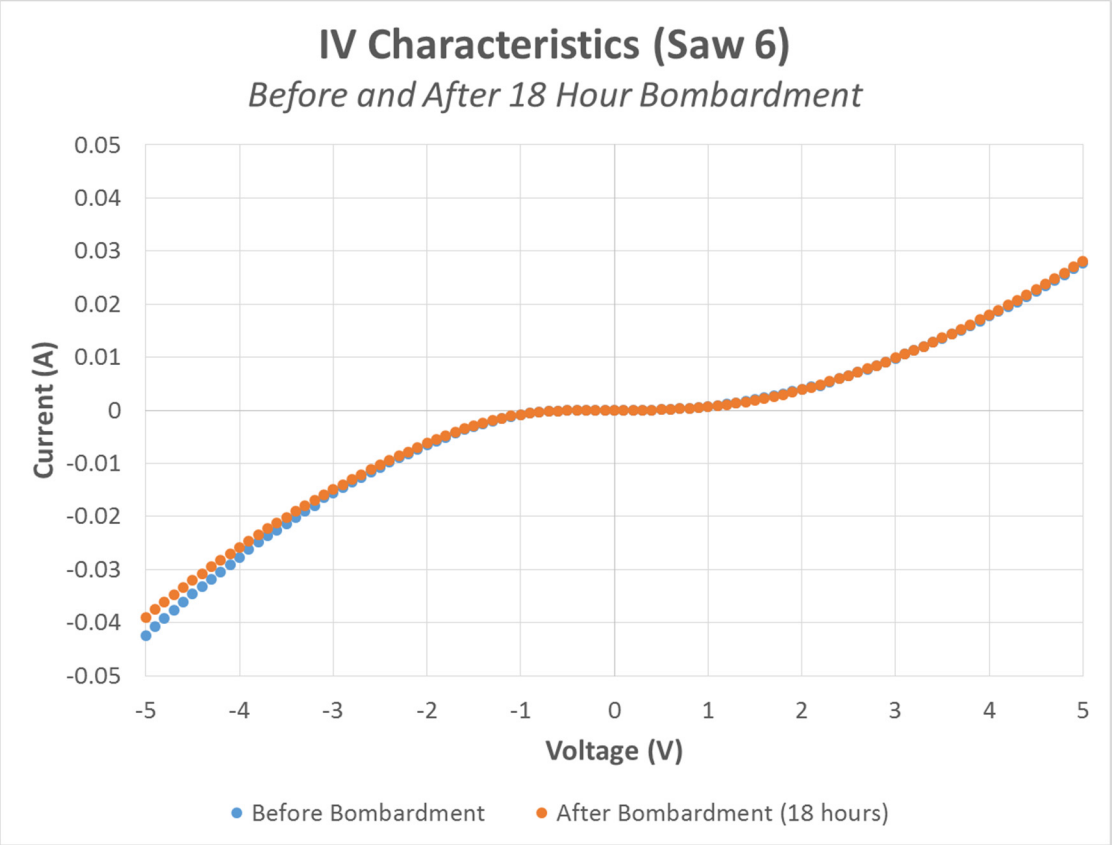

Figure 34: IV characteristics of p-GaN Saw #6 contact bombardment showing no significant change between no bombardment (blue) and the full 18 hour bombardment (orange).

Similarly the CV characteristics can be seen in Figure 35 and Figure 36 for Saw 5 and Saw 6, respectively. No major changes to the shape of the CV curves were noted here, and the magnitudes are also nearly identical before and after bombardment.

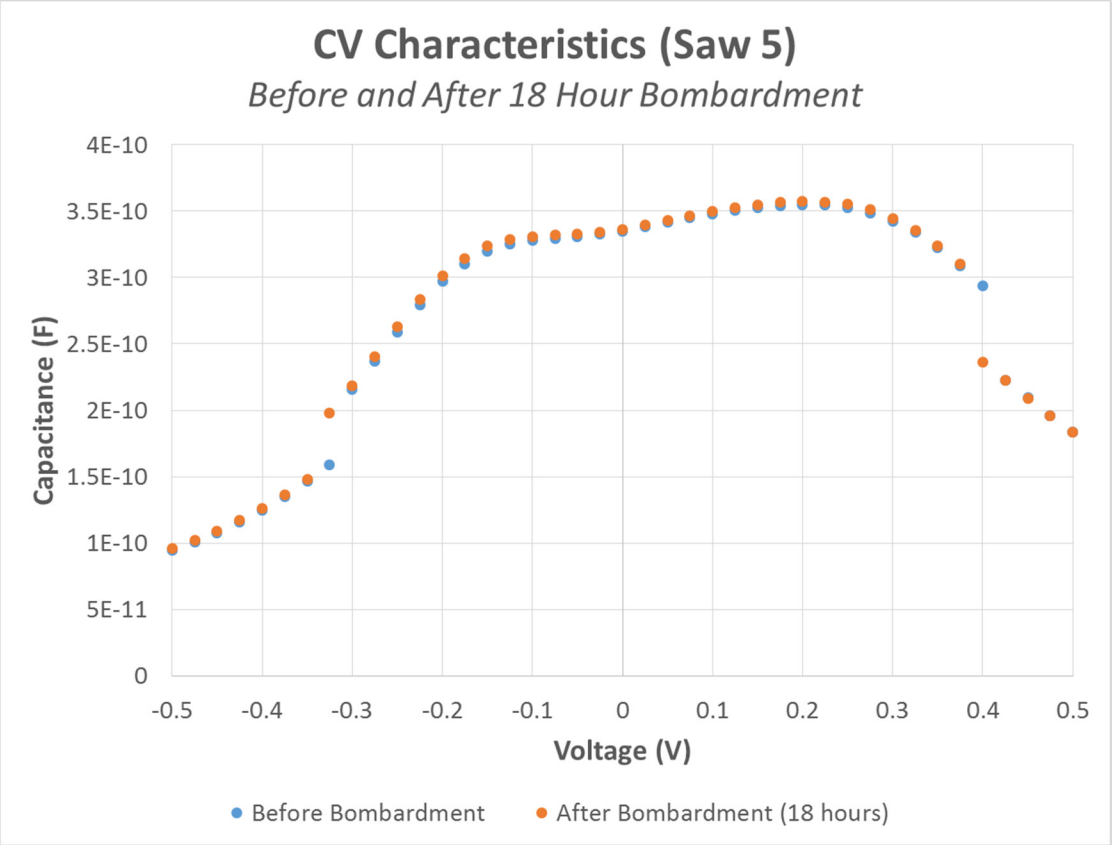

Figure 35: CV characteristics of p-GaN Saw #5 contact bombardment showing no significant change between no bombardment (blue) and the full 18 hour bombardment (orange) -- 10 kHz frequency

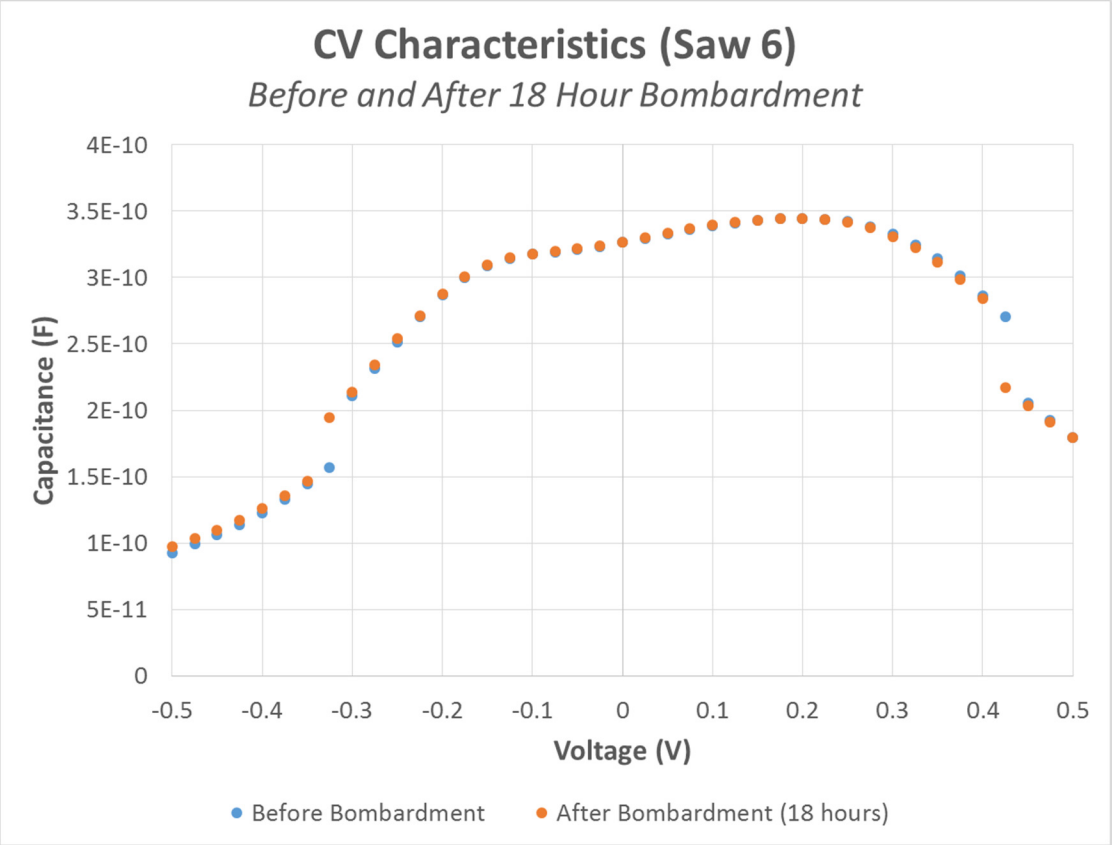

Figure 36: CV characteristics of p-GaN Saw #6 contact bombardment showing no significant change between no bombardment (blue) and the full 18 hour bombardment (orange) -- 10 kHz frequency

In summation, it can be seen from AFM and SEM measurements that we can expect no significant structural changes to both the contacts and semiconductor materials throughout a 100 year equivalent Ni-63-like bombardment. Additionally, CL measurements show that we can expect no major changes to the luminescence profile, and IV/CV measurements clearly show that there should similarly be no significant changes in the electrical properties of the contacts and material.

Controlling for Sample Heating

In order to ensure that the SEM bombardment would not heat our sample up (more than would be expected from Ni-63 exposure) and have an impact on the results of our experiment, some calculations were performed to estimate the maximum temperature

our samples could reach under SEM bombardment. Using an SEM electron energy of 20 keV, a sample current of 5700 pA and an illumination area of approximately 437 x 328 um^2, the energy flux can be calculated as:

$$Energy\ flux = \frac{P}{A} = 795\ \frac{W}{m^2}, \quad (13)$$

Note that the energy from sunlight in Low-Earth Orbit (LEO) is approximately 1350 W/m^2. From this, we can use Stefan–Boltzmann law (Equation 14) to determine the equilibrium temperature that our sample would reach given 795 W/m^2 of energy flux. This equation will give us the equilibrium temperature reached when the rate of energy emitted is equal to the rate of incident energy:

$$j^* = \varepsilon * \sigma * T^4, \quad (14)$$

where $\sigma = 5.670367 \times 10^{-8}$ W m^{-2} K^{-4} and we will assume an ideal radiator (emissivity $\varepsilon = 1$) as the worst-case. Solving for T with an energy flux of 795 W/m^2, we get a theoretically-maximum equilibrium temperature of 70.9 °C. Keep in mind that this is not even considering backscatter and thermal dissipation through the device packaging, which would lower the equilibrium temperature even further.

In summary, considering that the annealing temperature of our contacts is over 400 °C, and the annealing of our p-GaN material is done at over 800 °C, this temperature is low enough to where it should not have a noticeable impact on our experiment. Also note that, for an ideal radiator in LEO exposed to sunlight (1350 W/m^2), we would expect an equilibrium temperature of only around 119.9 °C (which is what we expect satellite equipment that is unprotected in space to undergo).

CHAPTER 4

MATERIAL AND DEVICE STUDY

We now have a working model that includes Ni-63 emission, beta particle absorption into GaN, and the expected device performances taking into account inefficiencies due to material quality and contact defects. At this point we also expect that our GaN material and contacts will be very resilient to exposure to beta particles from our Ni-63 source. The next step is to design the device itself.

In order to increase device efficiency, the electric field spanning our intrinsic region must be strong enough to span the entire region (thus reducing the amount of recombination that occurs in the intrinsic region). As mentioned previously, this can be done either by increasing the carrier concentration of the p-GaN region, or by reducing the carrier concentration in the intrinsic region. Since our p-GaN is already optimized, we have chosen to reduce the i-GaN carrier concentration by using BGaN, a boron-based alloy of GaN.

Carrier Density Study

In order to experimentally verify previous results that have been done [52] with data points closer to our target of around 0.9% boron, and to determine whether or not BGaN grown with hydrogen as a carrier gas has similar material properties as BGaN grown under nitrogen, various BGaN growths were performed and characterized. In Figure 37, we can see four growths made under nitrogen as blue dots: T1344 (0.2%B), T1346 (0.9%B), T1340 (1.4%B) and T1335 (1.7%B). The blue line that has been graphed comes from the previous experimental results. We can see that our experimental data follows the curve nicely, apart from the last two samples, which were too resistive

for our equipment to be able to measure (likely $10^{14}/cm^3$ or below, since we have successfully measured samples that were around $10^{15}/cm^3$).

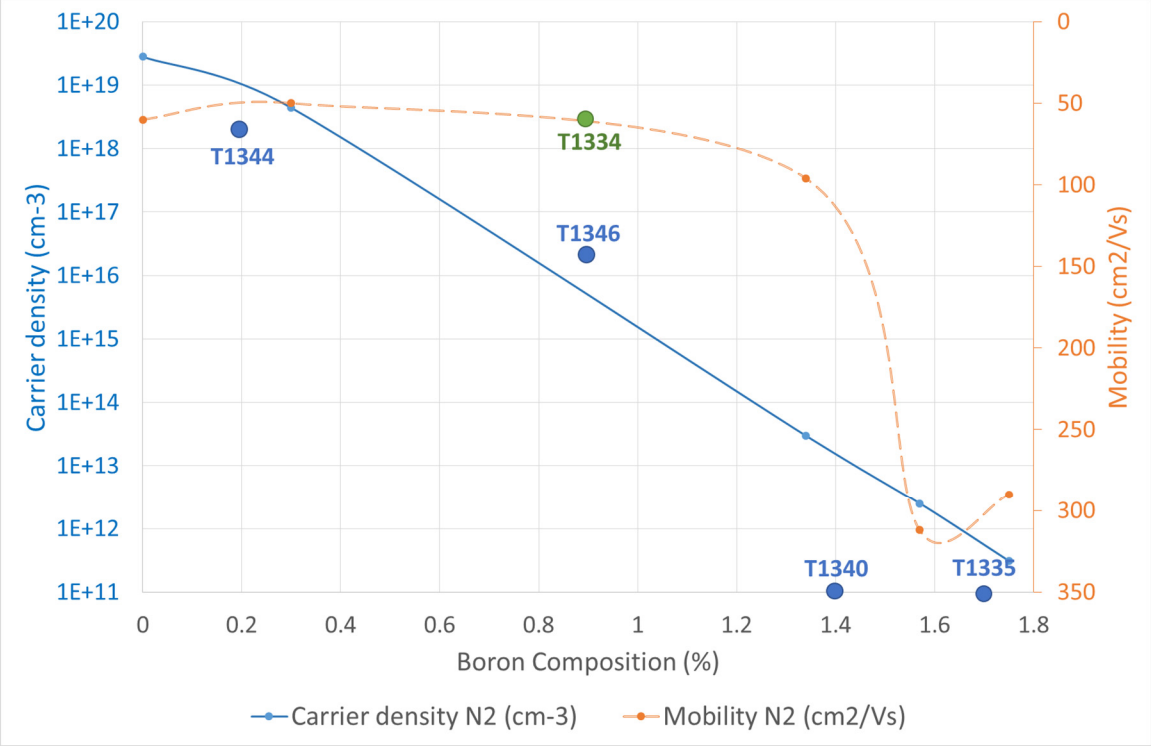

Figure 37: Carrier density and Mobility of BGaN as a function of boron composition. Note that points T1340 and T1335 were too resistive to measure and so are placed at the bottom of the chart.

The green dot is a sample grown with hydrogen as a carrier gas – T1334 (0.9%B), and unfortunately it does not seem to follow the reduced carrier density material property that BGaN grown under nitrogen appears to exhibit. One possible explanation for this is that BGaN grown under hydrogen grows extremely columnar (with nano-columns of BGaN), which could have a strong impact on the resistivity (and thus carrier density calculations) when measured across the material horizontally. This growth property is not seen in BGaN grown under nitrogen to the same extent, as BGaN under nitrogen grows in columnar "clumps" (see Figure 38 and Figure 39).

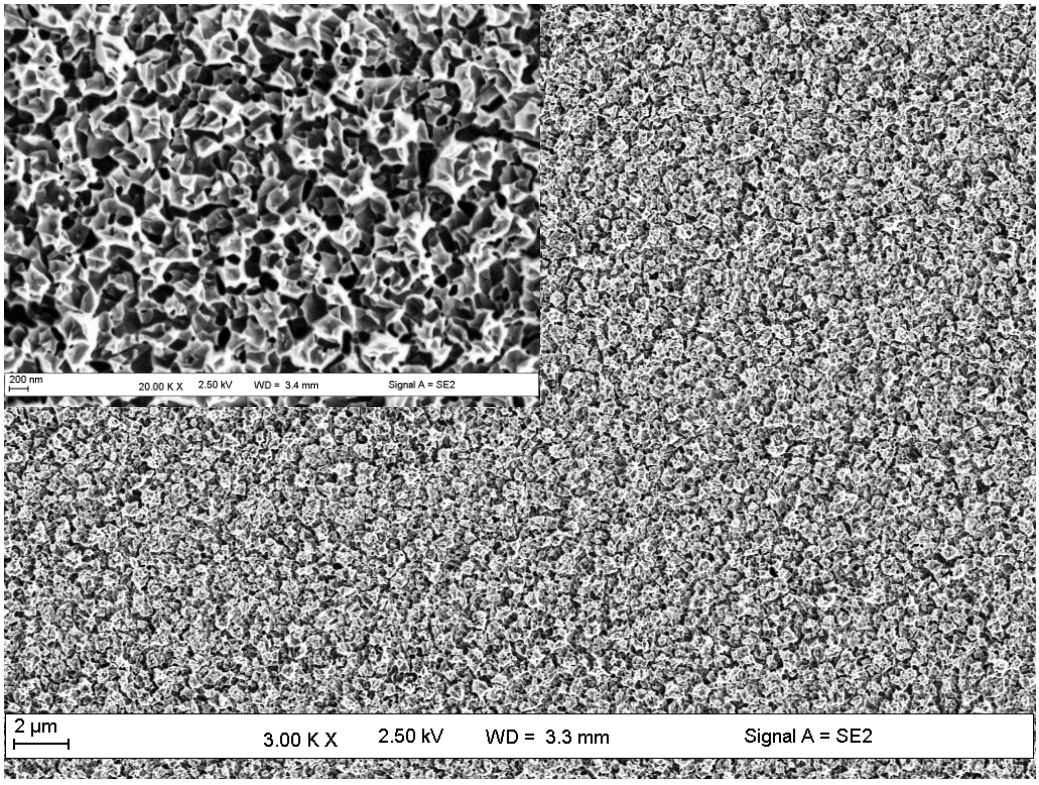

Figure 38: SEM image of T1334 – 0.9% BGaN/GaN STN H2 (350nm) at 3 K X. Inset at 20 K X.

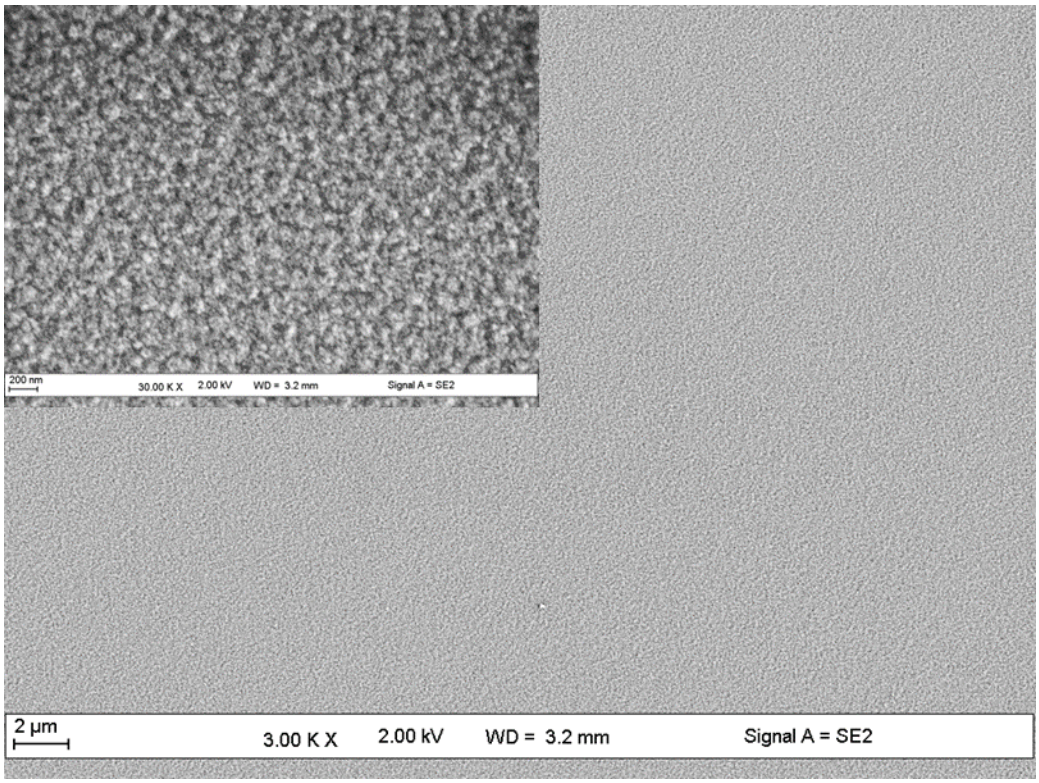

Figure 39: SEM image of T1335 – 1.7% BGaN/GaN STN N2 (450 nm) at 3 K X. Inset at 30 K X.

In Figure 38 and Figure 39 we can see an SEM-image comparison of BGaN grown under hydrogen and BGaN grown under nitrogen, respectively. Notice that, even though T1334 (under H2) has less boron incorporation and is thinner than T1335 (under N2), the surface is noticeably rougher and exhibits nano-column-like structures (with an RMS roughness of around 40 nm). We can see that T1335, on the other hand, is smoother and less columnar, even though it has nearly twice as much boron and is 100 nm thicker.

In a related study, the luminescence peak of BGaN (sample T1346, 0.9%B under N2) was calculated to be around 369 nm. Unfortunately the minority carrier lifetime could not be determined, since the lifetime was too short for our equipment to be able to measure (below 30 ns).

BGaN Smoothing Layer Study (BGaN under H2)

Now that we have confirmed that we expect BGaN grown under nitrogen to have a decreasing carrier density with increasing boron composition, we can grow a device to take advantage of this feature – a BGaN-based PIN. As stated previously, since BGaN grows with a 3D surface morphology with even small amounts of boron incorporated, a smoothing layer will be required to have a PIN device that can have high-quality contacts on the p-GaN cap.

The first BGaN PIN growth was done with a hydrogen carrier gas for BGaN (for comparison purposes), who's structure can be seen in Figure 40 (sample referred to as "T1277"). It includes 400 nm of BGaN (with 0.3% boron) followed by a 100 nm lateral-growth of magnesium-doped GaN in order to act as a smoothing layer for the underlying BGaN layer.

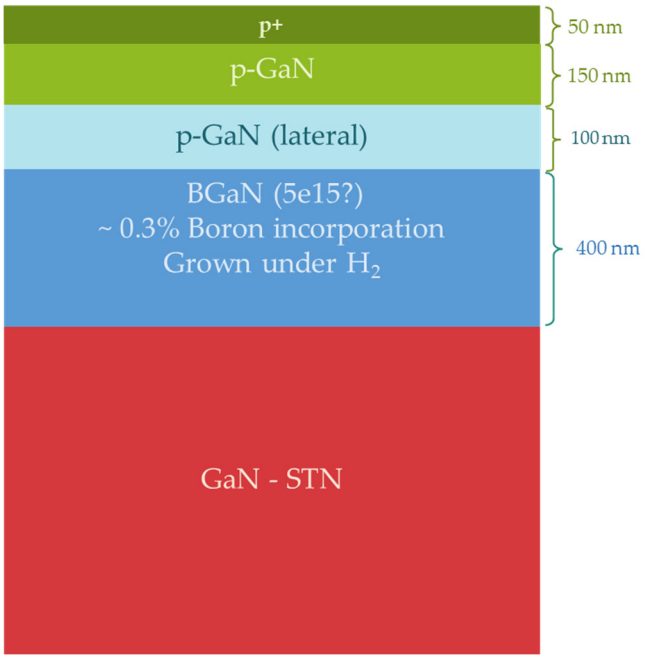

Figure 40: Initial BGaN PIN growth including smoothing layer (T1277).

In Figure 41 and Figure 42 we can see SEM images taken of the T1277 sample. Apart from the V-pits in the surface (which, as we will see later, are likely due to substrate defects and are common with p-GaN), we can visually see a very smooth surface. Compare this to the results from Figure 38, which has a slightly higher boron composition but similar growth conditions under hydrogen.

It should be noted that in Figure 43, particularly, we can see a very smooth growth on the plateaus themselves, with the plateaus acting as the majority of the overall surface roughness.

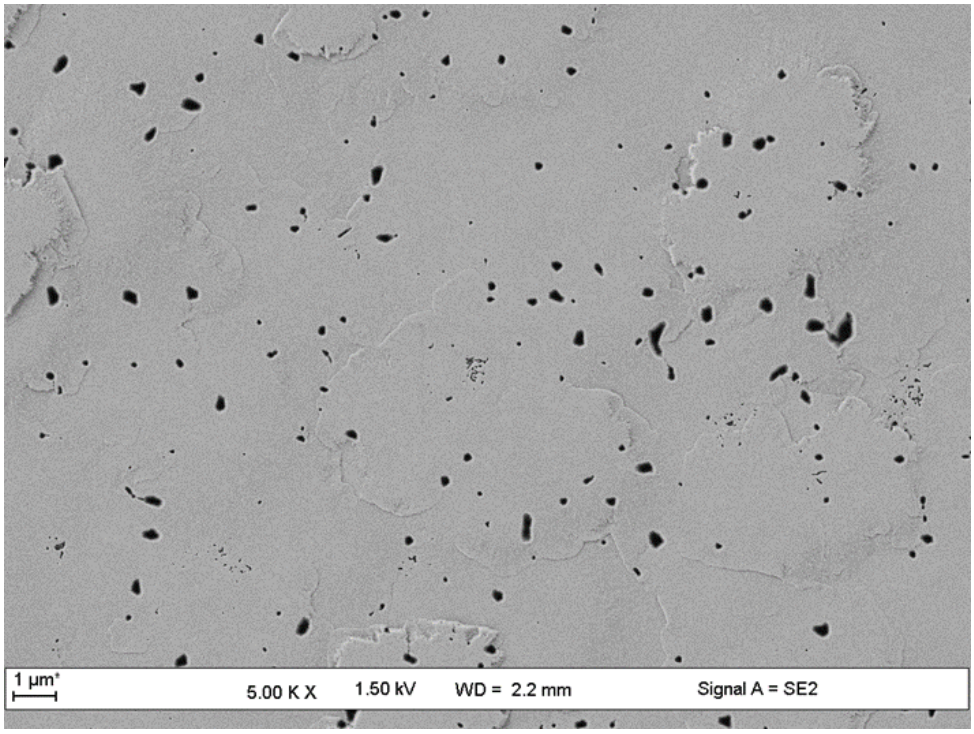

Figure 41: SEM image of T1277, 0.3%B under H2 at 5 K X.

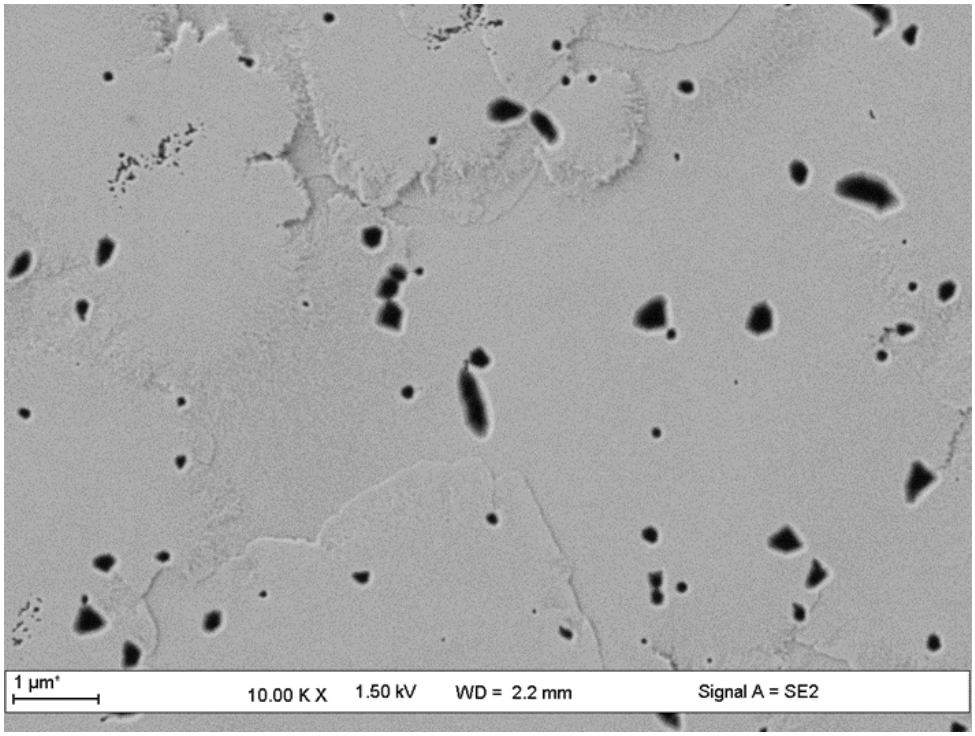

Figure 42: SEM image of T1277, 0.3%B under H2 at 10 K X.

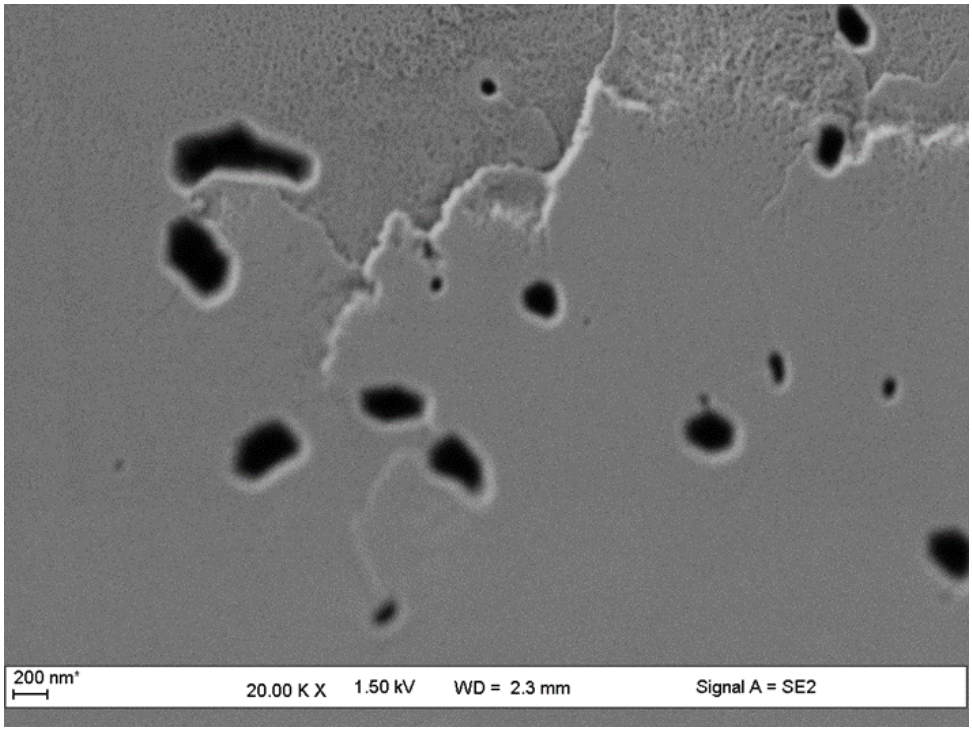

Figure 43: SEM image of T1277, 0.3%B under H2 at 20 K X.

As can be seen from the AFM results in Figure 44, the surface quality of T1277 was extremely good (< 1.2 nm roughness). Keep in mind that, electrically, the lateral growth of GaN behaves similarly to an intrinsic GaN layer, and therefore the T1277 PIN device effectively has an intrinsic region of around 500 nm (with a 200 nm p-GaN region).

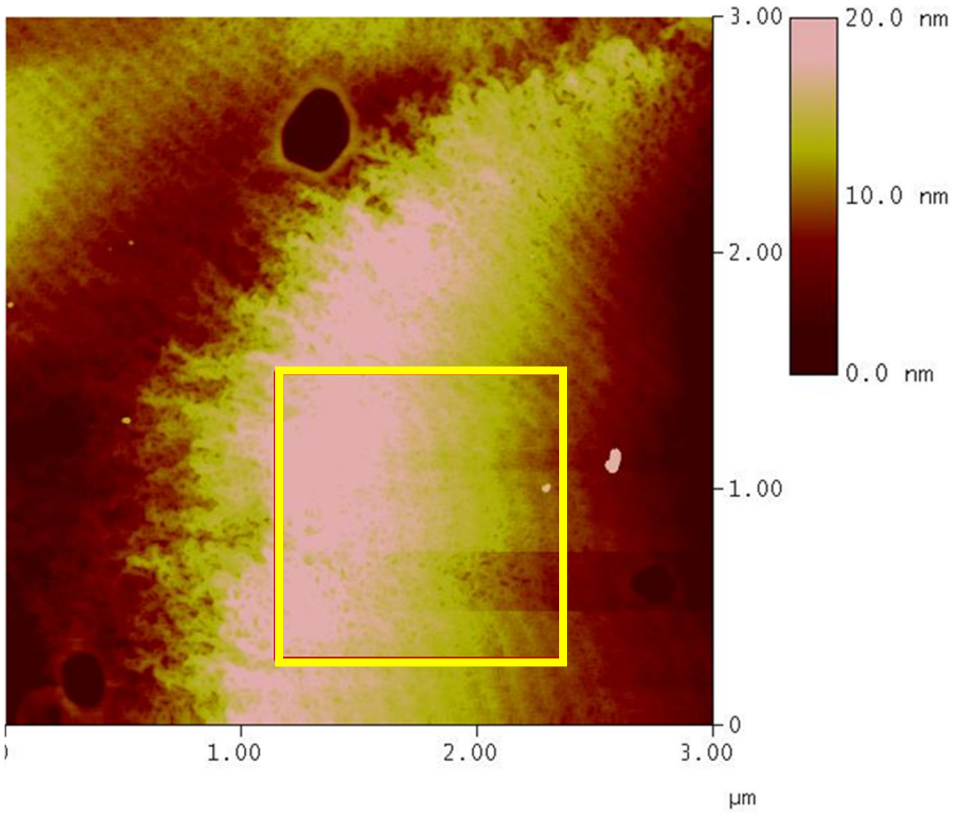

Figure 44: AFM image of T1277 BGaN PIN. The surface roughness between the V-pits (in the yellow box) is around 1.2 nm.

Now that the surface of T1277 has been analyzed, we can move on to looking at the material of the sample from a cross-section perspective. To do this, STEM was performed on the sample, as can be seen in Figure 45. The 100 nm lateral-growth layer is very clearly visible in this image (marked in red), since it is the only area of the material

with noticeable defects. These defects are likely due to the lateral-growth layer having been performed too quickly, and could be fixed in future growths by reducing the growth rate during this phase.

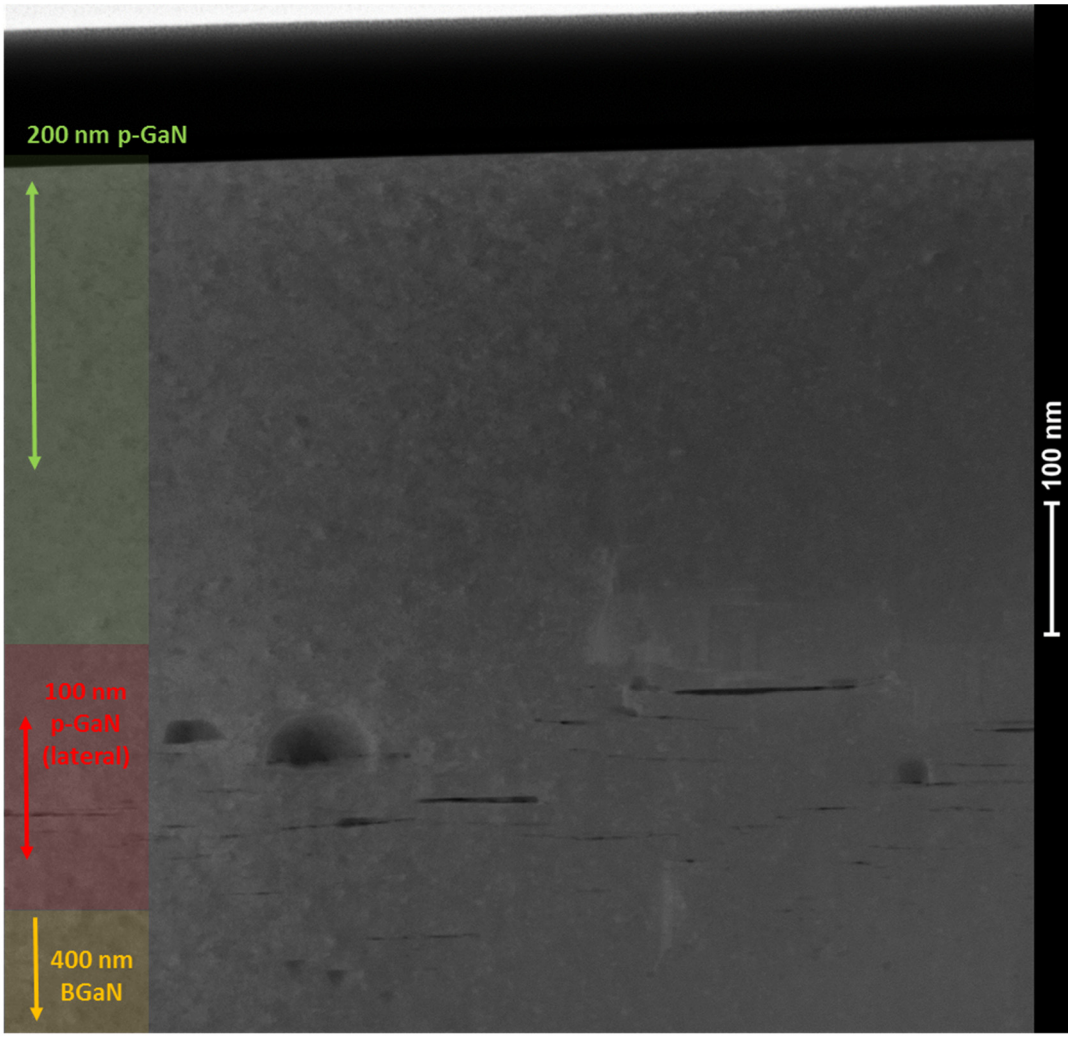

Figure 45: STEM HAADF image of T1277 BGaN PIN under hydrogen.

It can also be seen here that the p-GaN layer has grown thicker than predicted, and is actually closer to around 300 nm instead of the expected 200 nm. This means that the p-GaN grew at a faster rate than during previous calibrations, and the growth rate needs to be reduced for future runs of p-GaN.

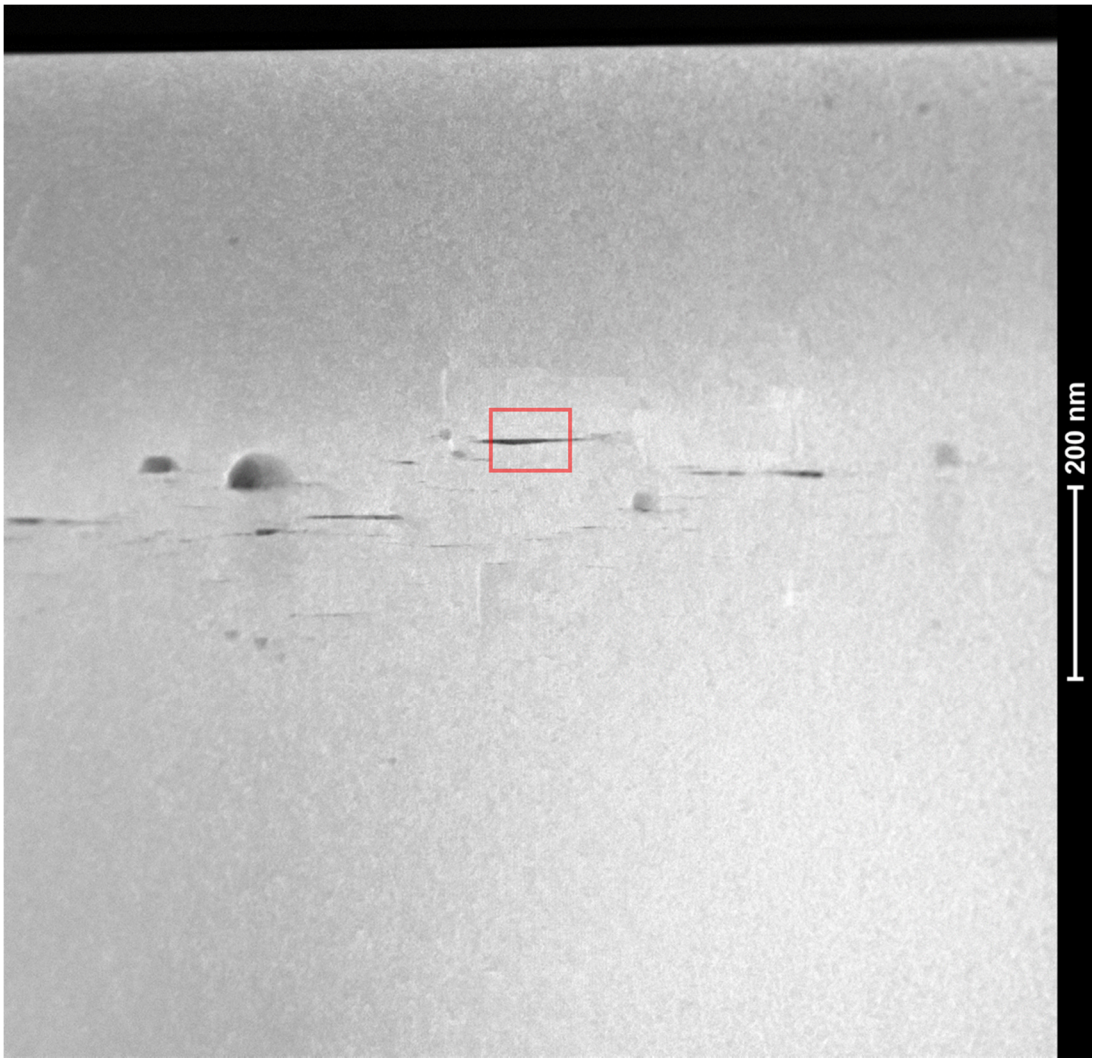

Figure 46: STEM HAADF image of T1277 showing a high quality material above and below GaN smoothing layer. Red box denotes area where Figure 47 is taken.

In Figure 46 we can see very clearly that the BGaN growth quality was very good, since the incorporation of boron was very low (only around 0.3%). Again, the only defects visible in the image are due to the lateral-growth layer. The red box in this figure denotes the area where Figure 47 was taken at a much higher zoom (~10 nm resolution).

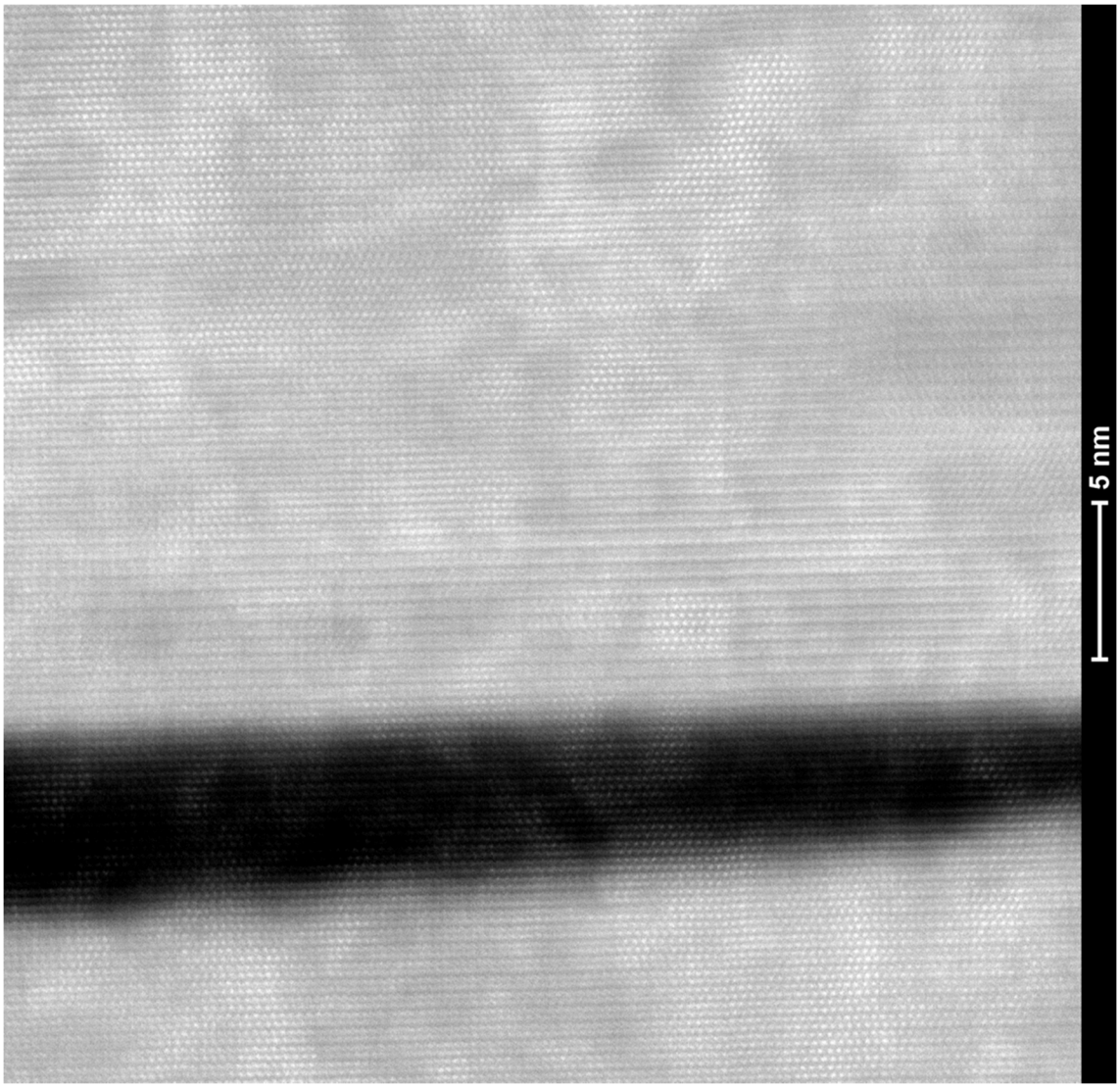

Figure 47: STEM HAADF close-up of T1277 showing a good crystalline structure in the lateral-growth region above and below gaps.

This image shows us that the crystalline quality of the lateral-growth layer is good outside the area of the gaps (black, where the material density is very low). We can confirm this by performing a FFT of Figure 47, seen in Figure 48, to get a reciprocal space mapping. The periodic crystalline structure can be noted, along with a relatively strong central peak.

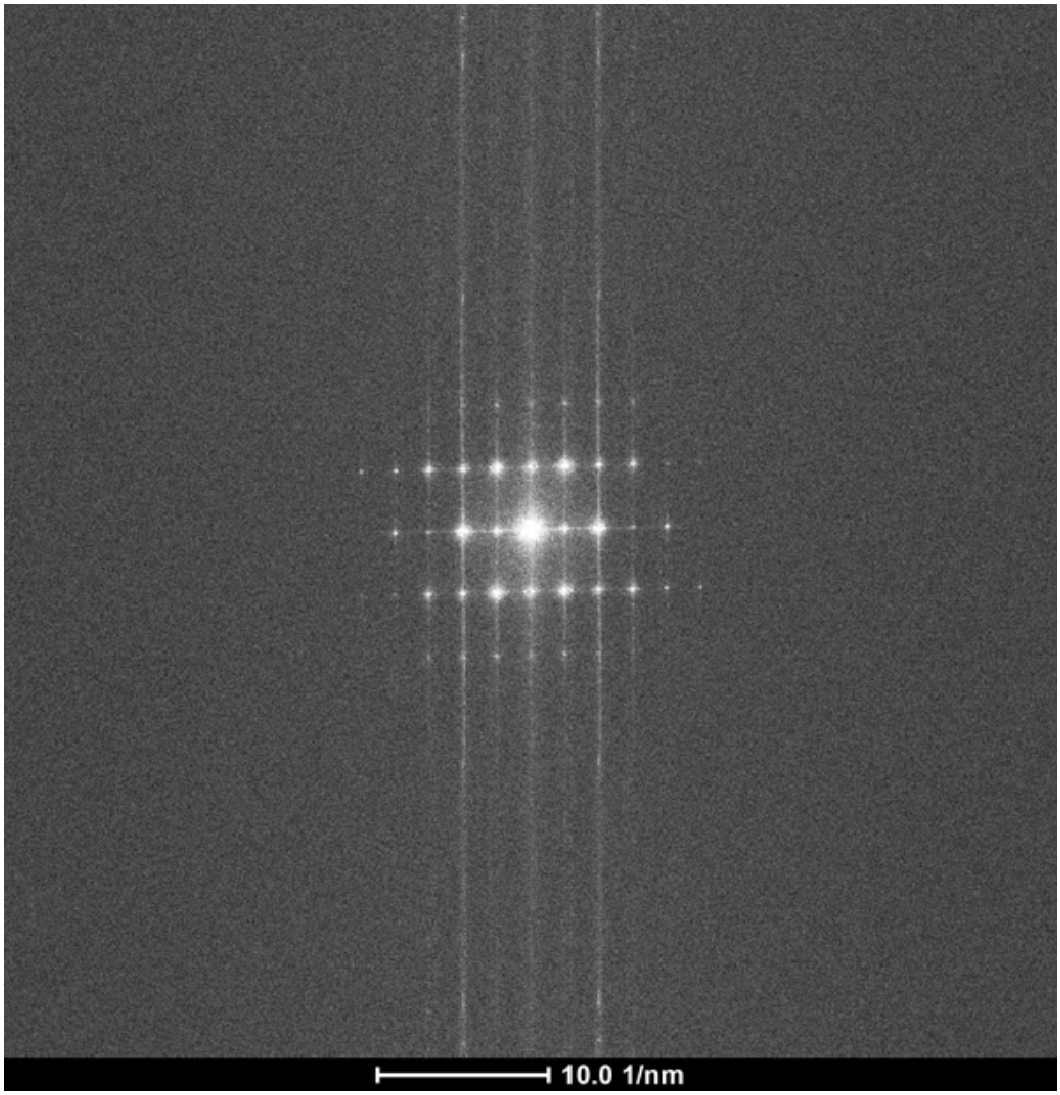

Figure 48: FFT from STEM of T1277 performed in lateral-growth region of PIN (from Figure 47).

The T1277 device was the first time a BGaN-based PIN has ever been constructed, as far as we are aware. It serves as a proof-of-concept that a lateral-growth layer can successfully smooth the 3D surface roughness witnessed in BGaN, and can act as a nice surface for depositing contacts. The T1277 device was not, however, processed, since material analysis results (as discussed before) for BGaN grown under hydrogen are not expected to have a low carrier concentration. It is therefore expected that T1277 would not make a good-quality PIN device. Later growths of BGaN PINs were all done

with BGaN grown under nitrogen, which does exhibit the desired low carrier-concentration.

BGaN Smoothing Layer Study (BGaN under N2)

In Figure 49 we can see the structure of T1353, the first BGaN PIN grown under nitrogen. Two subsequent growths were also performed with the same structure but differing boron incorporations: T1379 (1.24% boron) and T1382 (1.2% boron) and had a BGaN intrinsic region of 500 nm (instead of 400 nm). An additional growth was also attempted, labeled T1403, but with an unknown BGaN thickness (though at least 500 nm) and a 1% boron incorporation. One final growth, T1405, was grown with the exact same specifications as T1353. This section will detail and discuss the results of all of these growths.

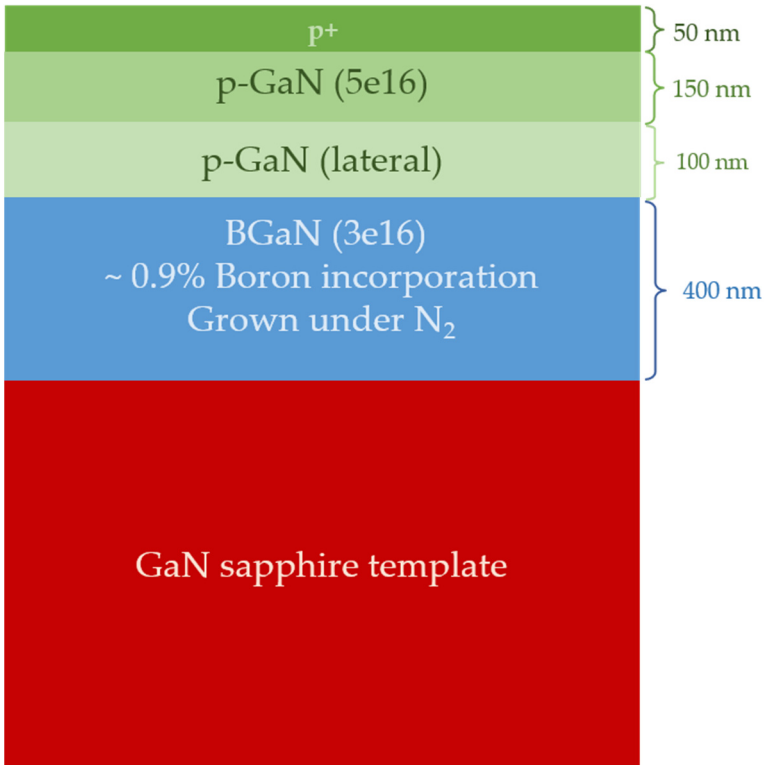

Figure 49: BGaN PIN T1353 with lateral-growth smoothing layer.

SEM results for these growths can be seen in the following figures. In Figure 50 and Figure 51 we can see results for T1353b at 5 K X and 50 K X magnification, respectively. The typical p-GaN V-pits (as seen earlier in T1277) are also seen in T1353 (which we will see in more detail in the STEM results for this sample). These pits are not noticed in the T1379 and T1382 samples, however, as witnessed from SEM results in Figure 52 and Figure 54, respectively. It is possible that this is due to the fact that the strains which caused the V-pits in T1353 were released as cracks in the samples for T1379 and T1382 (cracking was rarely seen in T1353, but was prevalent in T1379 and T1382).

The rougher-appearing surface in T1379 and T1382 (most evident in Figure 53 and Figure 55) can be explained by the fact that they were grown with 500 nm of BGaN instead of 400 nm as with T1353. If the BGaN layer is grown thicker, then a thicker lateral-growth smoothing layer could be required to obtain a similarly-high-quality surface.

This is exemplified in Figure 56 and Figure 57, which shows SEM results for sample T1403 at 10 K X and 50 K X, respectively. This growth had less boron than T1379 and T1382 – only 1%, but was likely grown thicker, with a BGaN layer of at least 500 nm. Reflectivity was lost during this growth, so it was not possible to get a good estimate of the growth thickness. The sample has a similar roughness to T1379 and T1382, but with more pronounced islands.

Finally we can see in Figure 58 and Figure 59 the SEM results for T1405b at 10 K X and 20 K X, respectively. These results show a similar quality to T1353b. Note here that there were very few V-pits in this sample, and also very little cracking. This might be due to the smoothing layer covering and burying any cracking that may have occurred, the sample might have been grown to an optimal thickness and boron concentration which did not have excessive strain resulting in cracking and V-pits, or the substrate may have had fewer defects than in the previous run. A STEM study could be done in the future to confirm these suspicions.

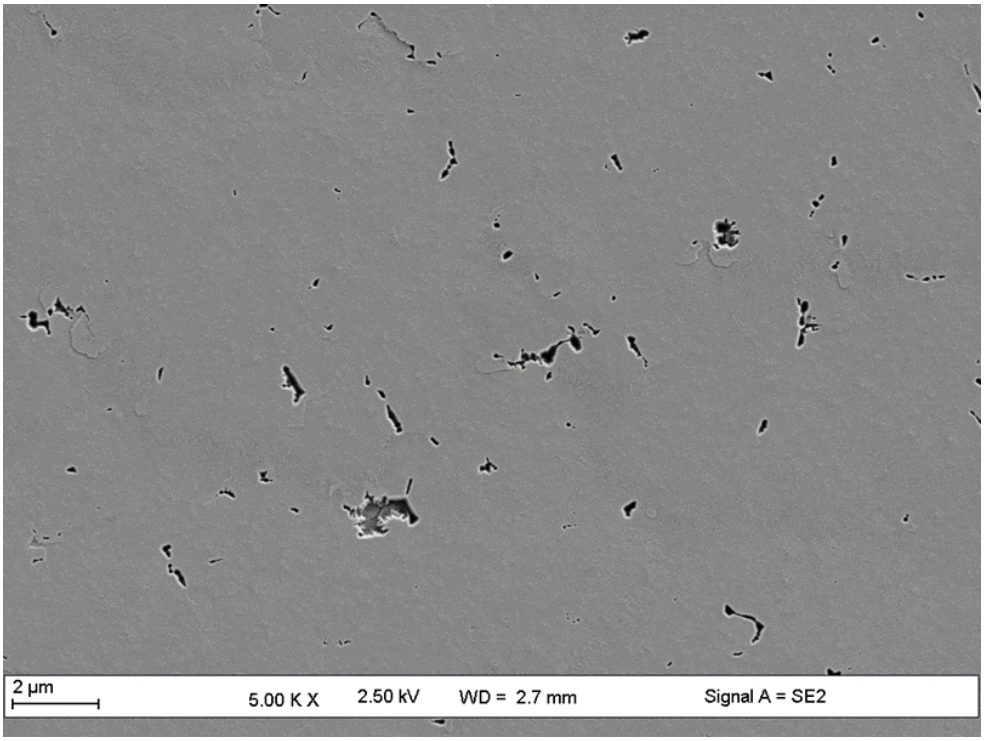

Figure 50: SEM image of T1353b (0.9% boron) at 5 K X.

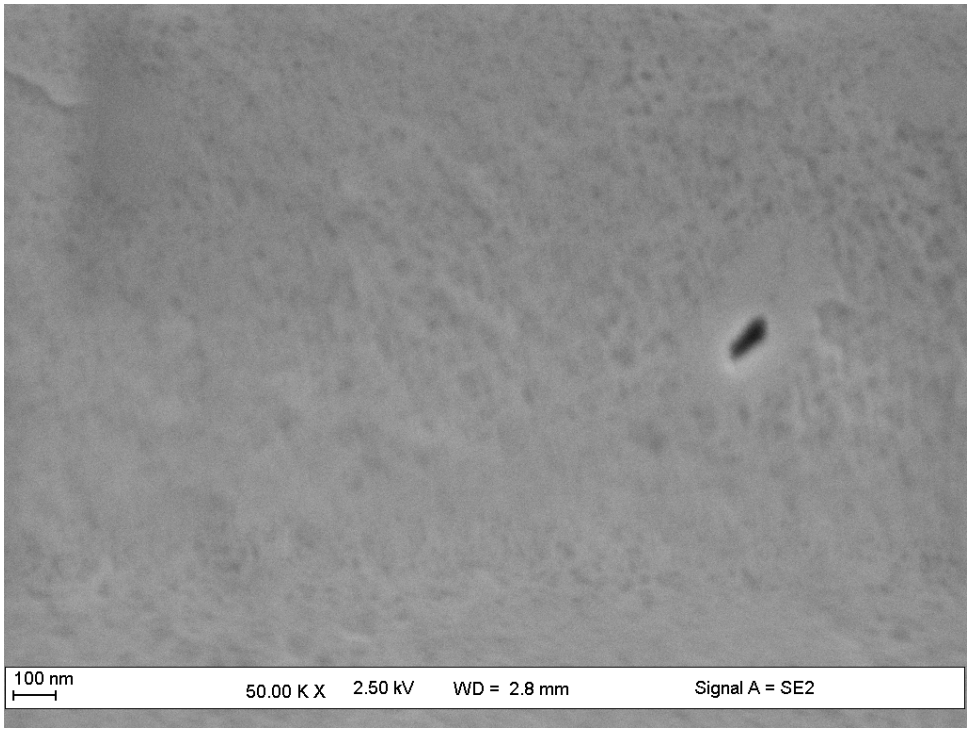

Figure 51: SEM image of T1353b (0.9% boron) at 50 K X.

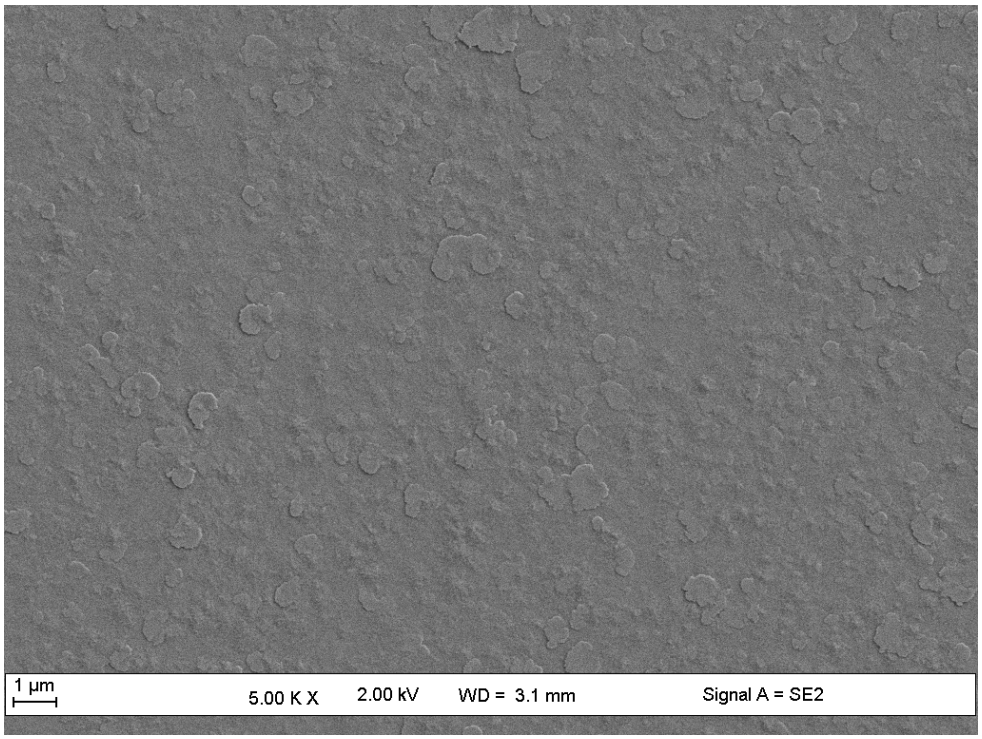

Figure 52: SEM image of T1379 (1.24% boron) at 5 K X.

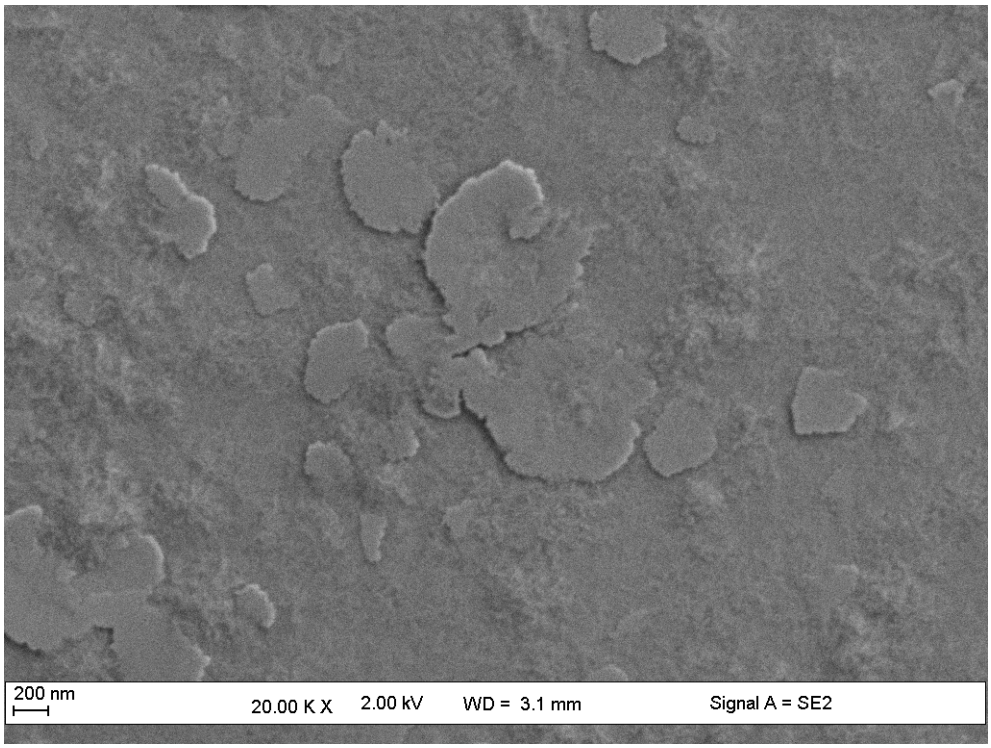

Figure 53: SEM image of T1379 (1.24% boron) at 20 K X.

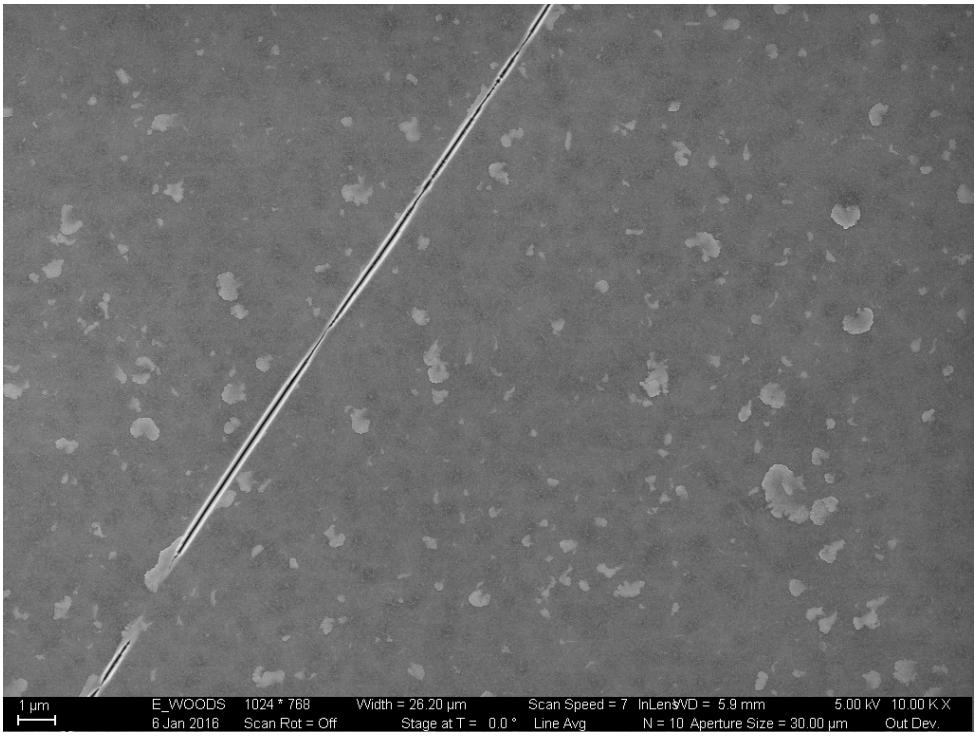

Figure 54: SEM image of T1382 (1.2% boron) at 10 K X.

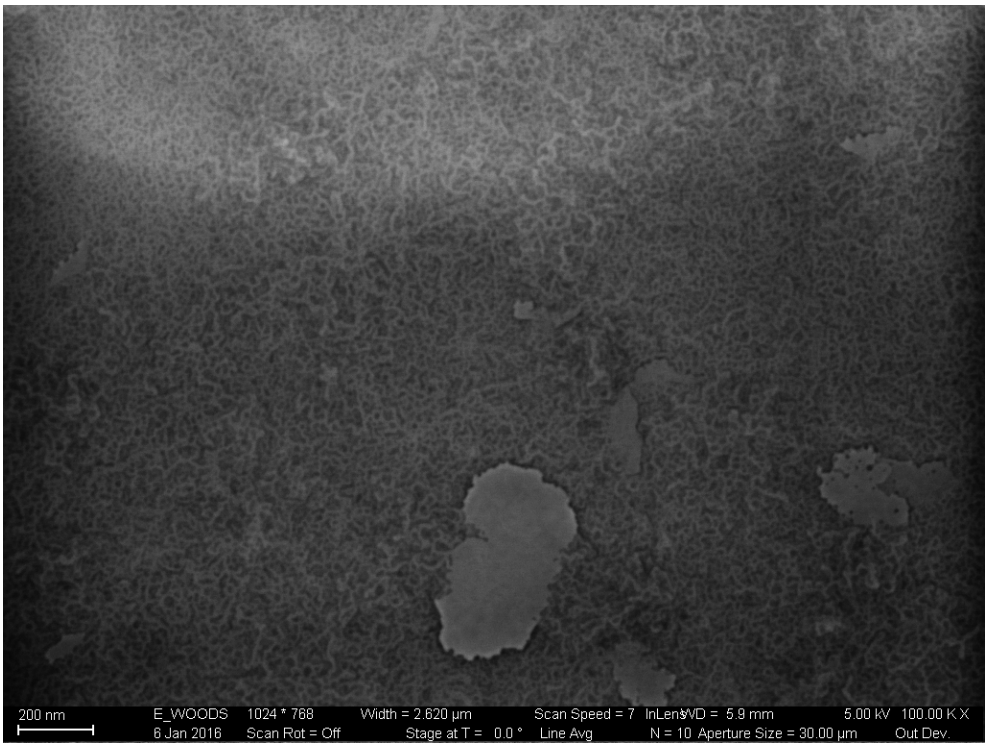

Figure 55: SEM image of T1382 (1.2% boron) at 100 K X.

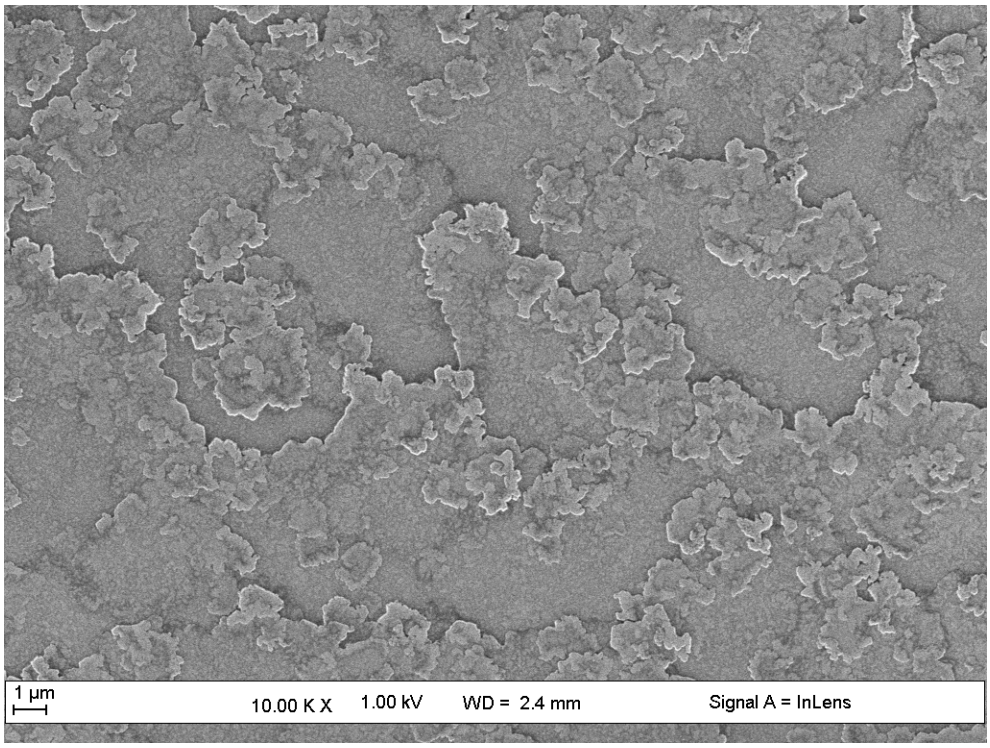

Figure 56: SEM image of T1403 (1% boron) at 10 K X.

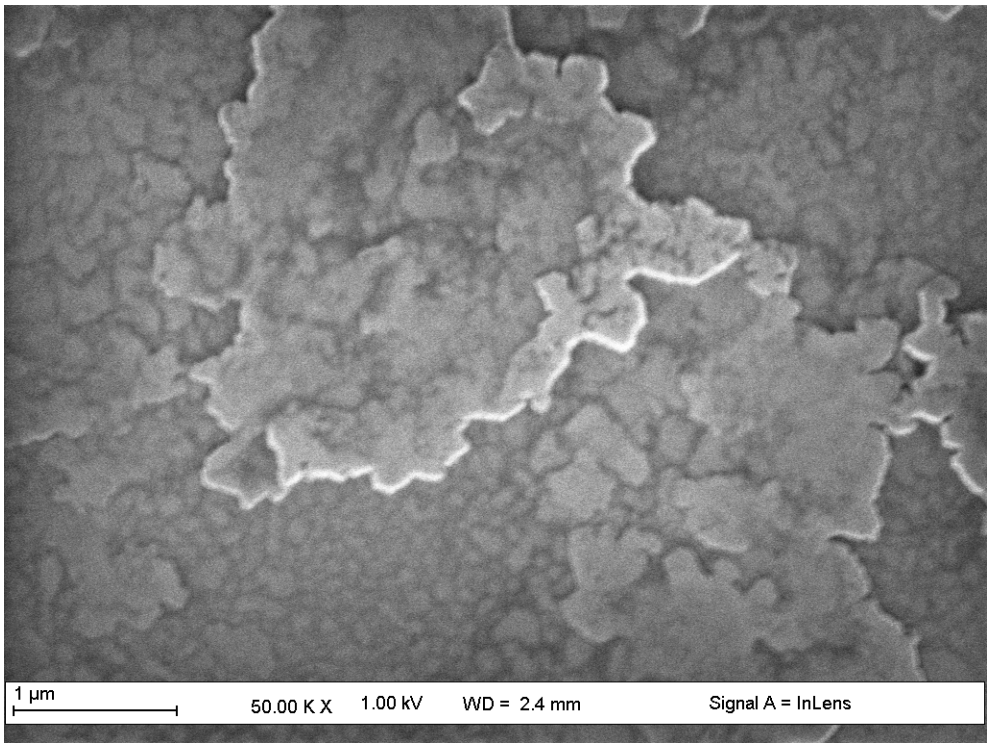

Figure 57: SEM image of T1403 (1% boron) at 50 K X.

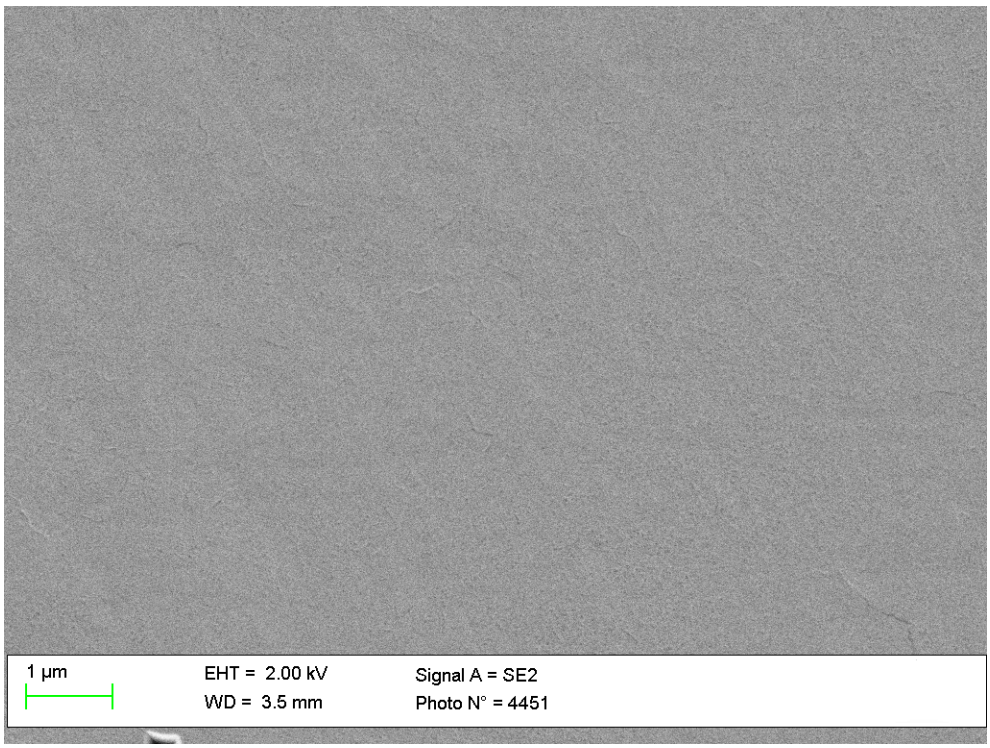

Figure 58: SEM image of T1405b (0.9% boron) at 10 K X.

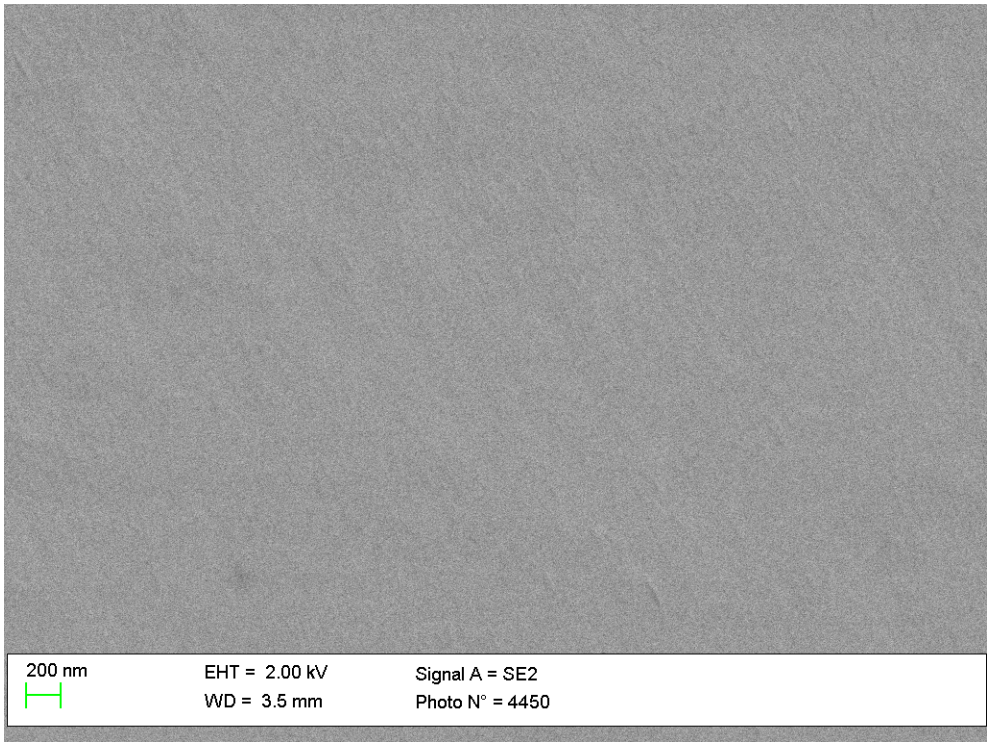

Figure 59: SEM image of T1405b (0.9% boron) at 20 K X.

In Figure 60 we can see an optical microscope image of the T1353 sample, showing a relatively smooth surface with very little surface cracking. A few cracks can be seen in T1353, as in Figure 61, often originating from defects, though these cracks are uncommon.

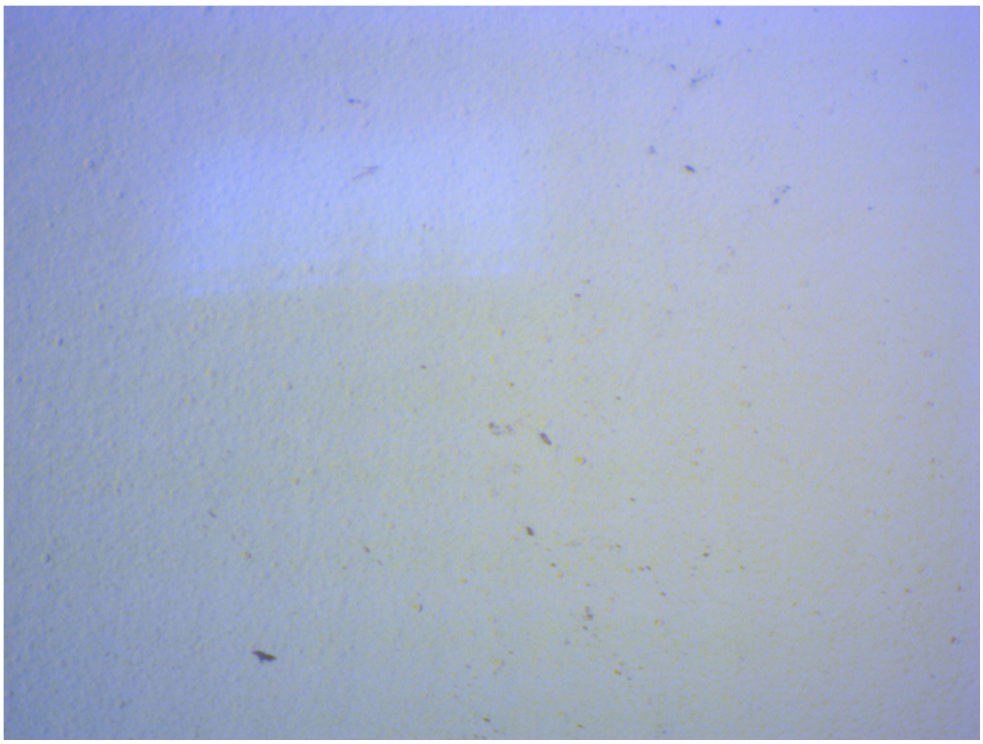

Figure 60: Optical microscope image of T1353b. 10x magnification

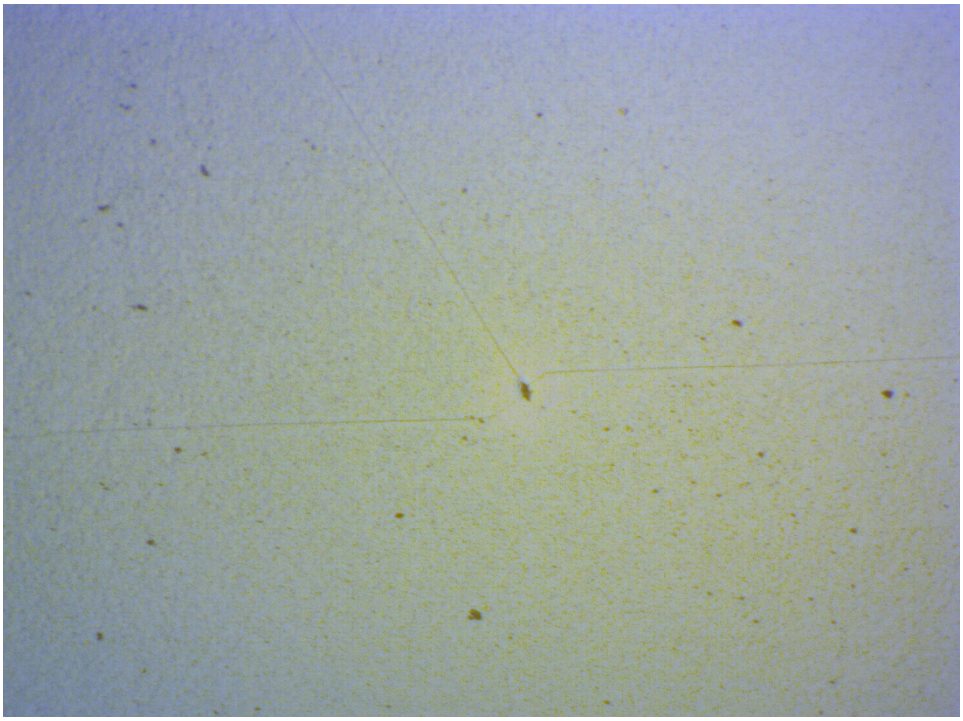

Figure 61: Optical microscopy image of T1353b showing cracks on surface. 10x magnification

Comparing this to T1379 and T1382, for example in Figure 62 and Figure 63, it becomes clear that cracking is much more commonly seen in these samples. This could be due to the fact that their boron concentrations were higher (0.9% for T1353 vs. over 1.2% for T1379 and T1382), and also because the thicknesses of T1379 and T1382 were 100 nm more than T1353. The increased lattice mismatch between a higher boron BGaN layer and the n-GaN template, along with the increased thickness of the BGaN layer, could be making the sample more susceptible to crack formation [63].

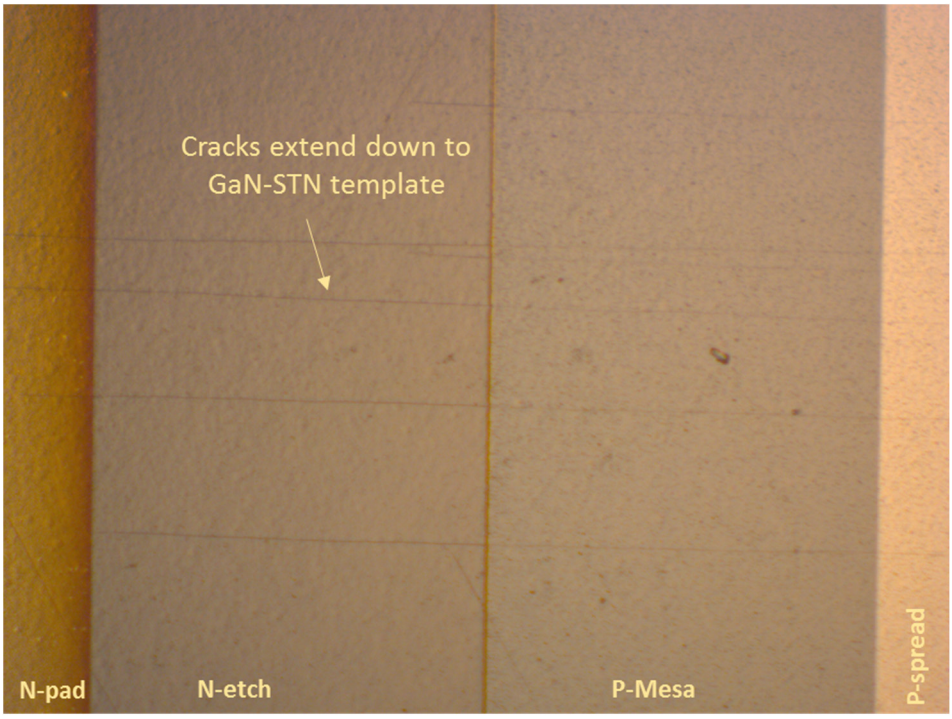

Figure 62: Optical microscopy image of T1379 after processing, showing cracks that extend down to the GaN-STN template. 10x magnification

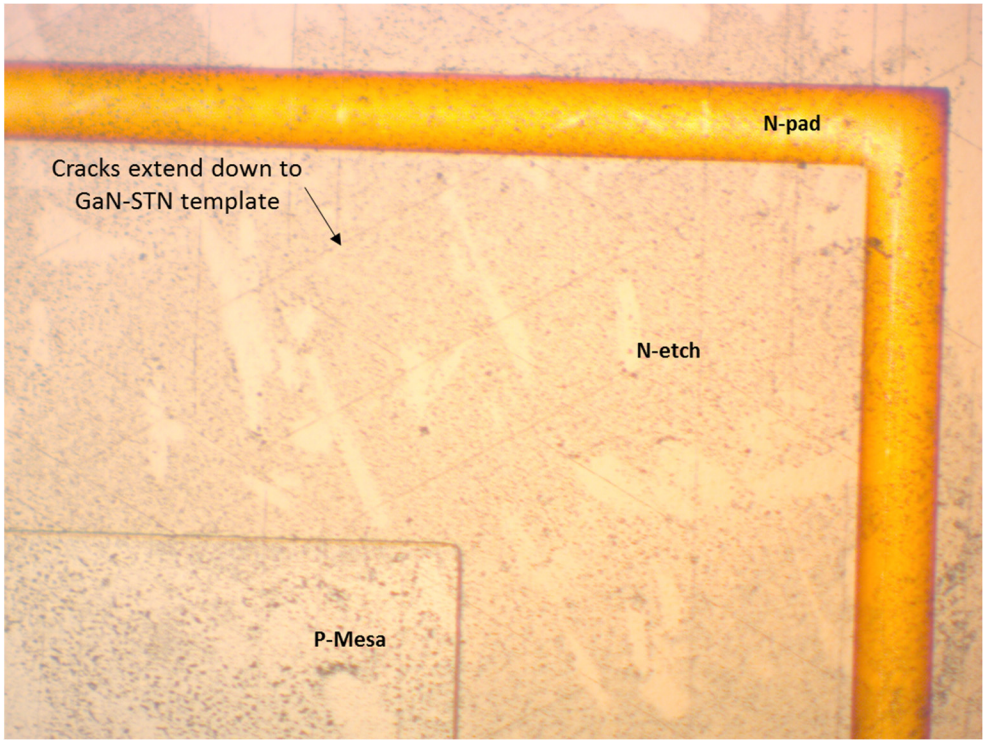

Figure 63: Optical microscope image of T1382 after processing, showing cracks extending down to the GaN-STN template. 10x magnification

Likewise, Figure 64 shows the T1403 sample with similar cracking to the T1379 and T1382 samples. In Figure 65 we can see a 100x magnification close-up which highlights the rough surface (similar with what is seen in the SEM images).

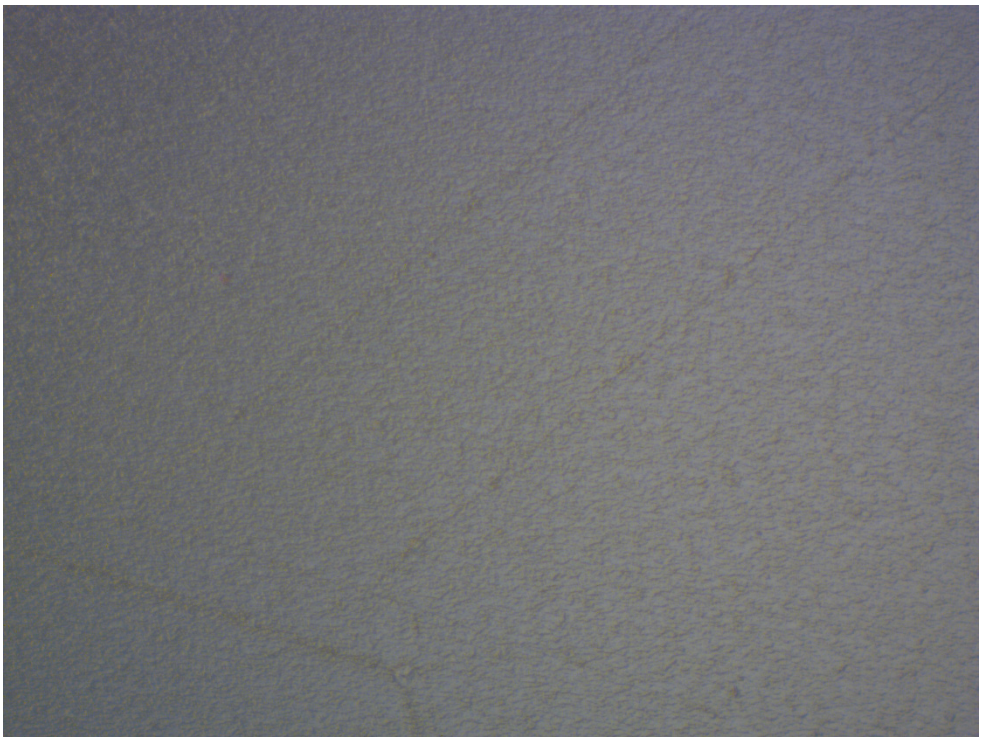

Figure 64: Optical microscope image of T1403 showing cracks on surface. 10x magnification

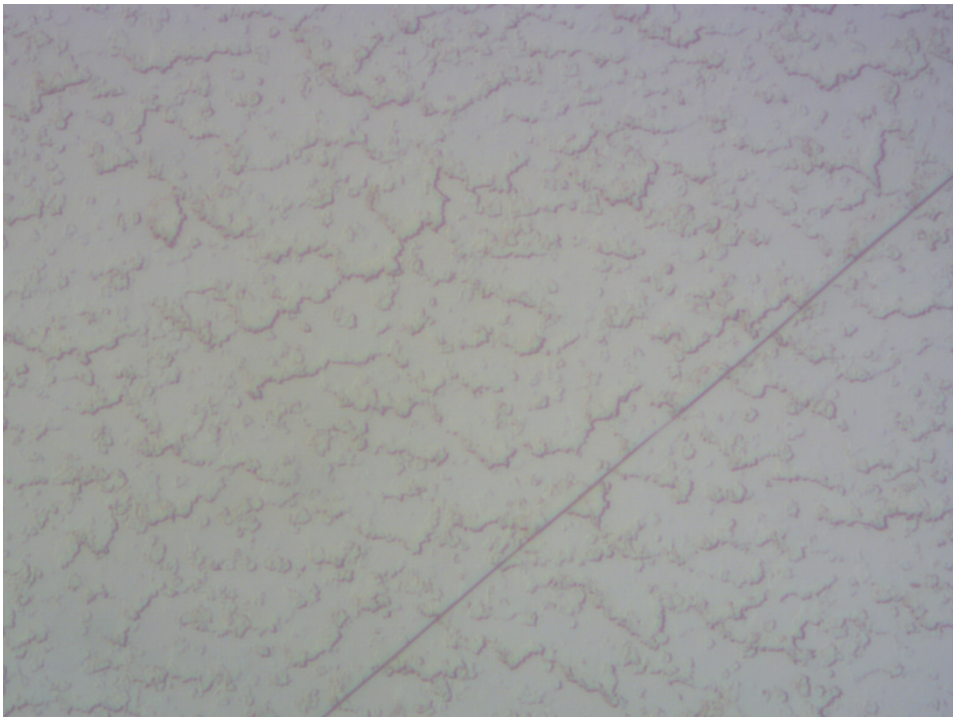

Figure 65: Optical microscopy image of T1403 highlighting surface roughness. 100x magnification

Lastly, the T1405 growth consisted of two quarter pieces of a 2-inch wafer (labeled as T1405a and T1405b). One can see the T1405a sample in Figure 66, bearing a close resemblance to T1353 (as expected, since it is the same growth parameters). The entire surface is crack-free near the center of the sample, but exhibits some edge cracking as seen in Figure 67. In Figure 68 and Figure 69, one can see what is potentially a crack that has been covered by the lateral-growth layer. In Figure 70, sample T1405b is shown with no cracking anywhere on the sample, except for some light cracks near the edge (as seen in Figure 71), likely due to cutting the wafer.

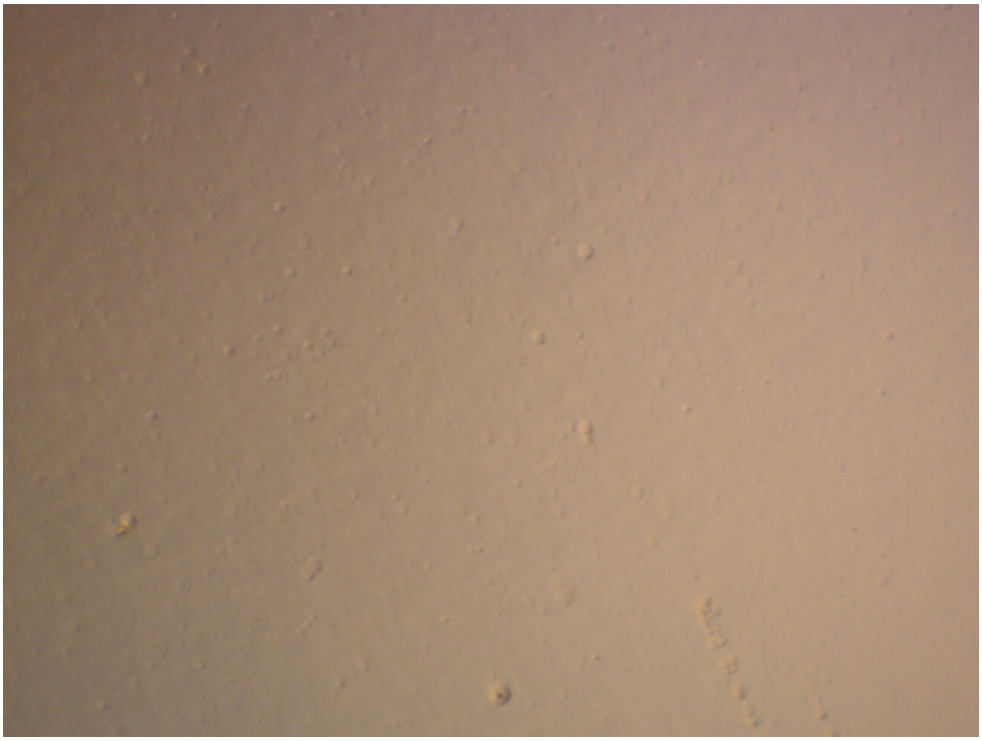

Figure 66: Optical microscope image of T1405a showing smooth surface near center. 10x magnification

Figure 67: Optical microscope image of T1405a showing cracking near edge. 10x magnification

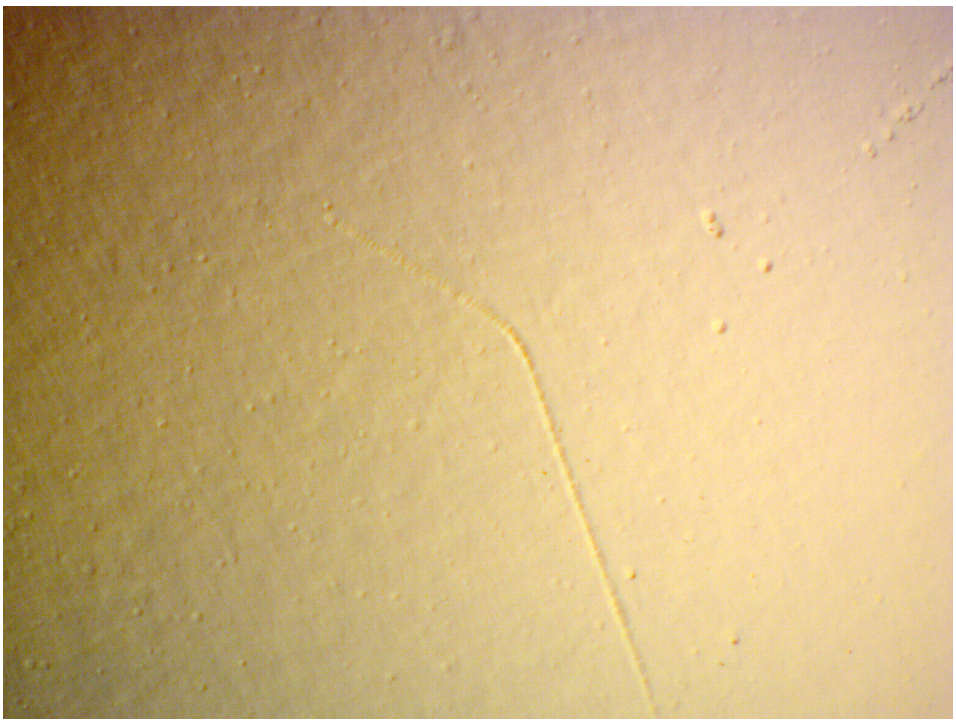

Figure 68: Optical microscopy image of T1405a showing potentially-covered crack by lateral-growth layer. 10x magnification

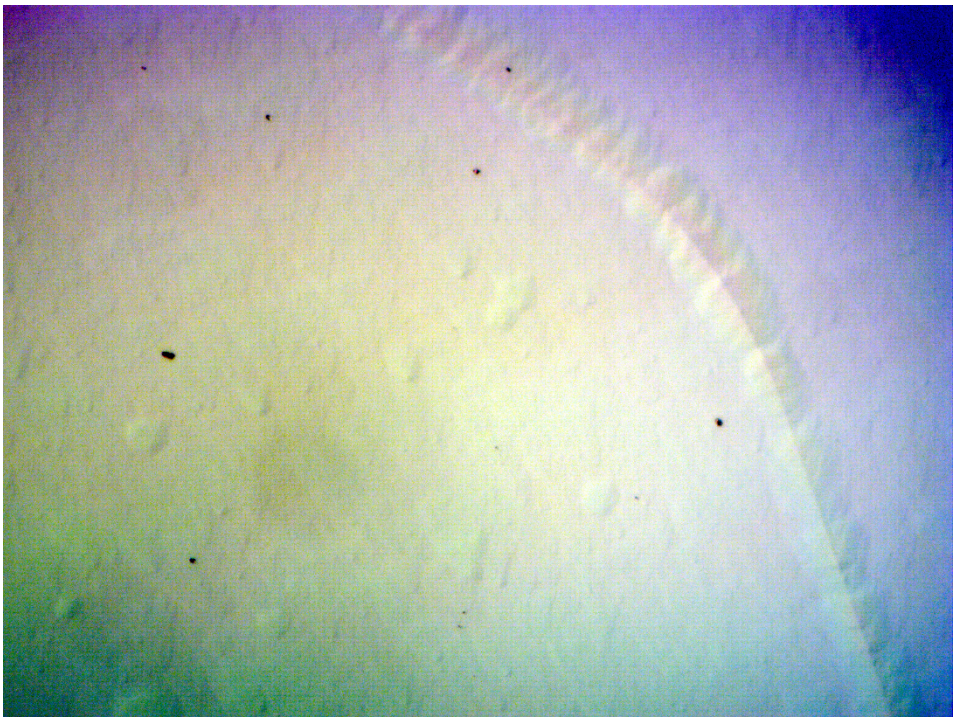

Figure 69: Optical microscopy image of T1405a showing potentially-covered crack by lateral-growth layer. 50x magnification

Figure 70: Optical microscope image of T1405b showing a crack-free surface. 10x magnification

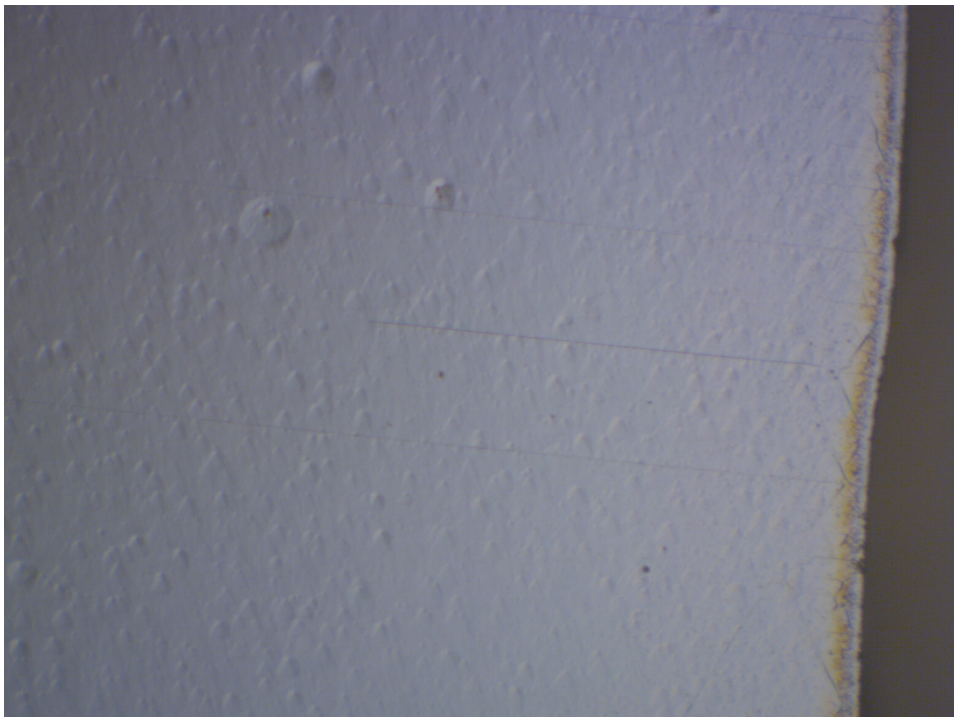

Figure 71: Optical microscopy image of T1405b showing light cracking on edge of sample, likely due to wafer cutting. 10x magnification

Figure 73 shows the AFM image for a 5 um x 5 um square piece of sample T1353b, which displays a very high quality surface of around 1.1 nm roughness (inside the yellow box) or around 1.5 nm roughness overall. One can compare this with Figure 72, which is the same growth as T1353 but without the smoothing and p-GaN layers. The roughness has essentially been reduced from over 5 nm RMS to around 1 nm RMS roughness due to the smoothing layer growth and p-GaN cap.

T1353 can also be compared with samples T1379 in Figure 74 and T1382 in Figure 75, which show a roughness of around 5.6 nm overall (6 nm in the box) and 11 nm overall (3.3 nm in the box), respectively. Note again that these two samples have a higher boron concentration than T1353b and were also grown to be 100 nm thicker, which could explain the slightly increased surface roughness that we see here.

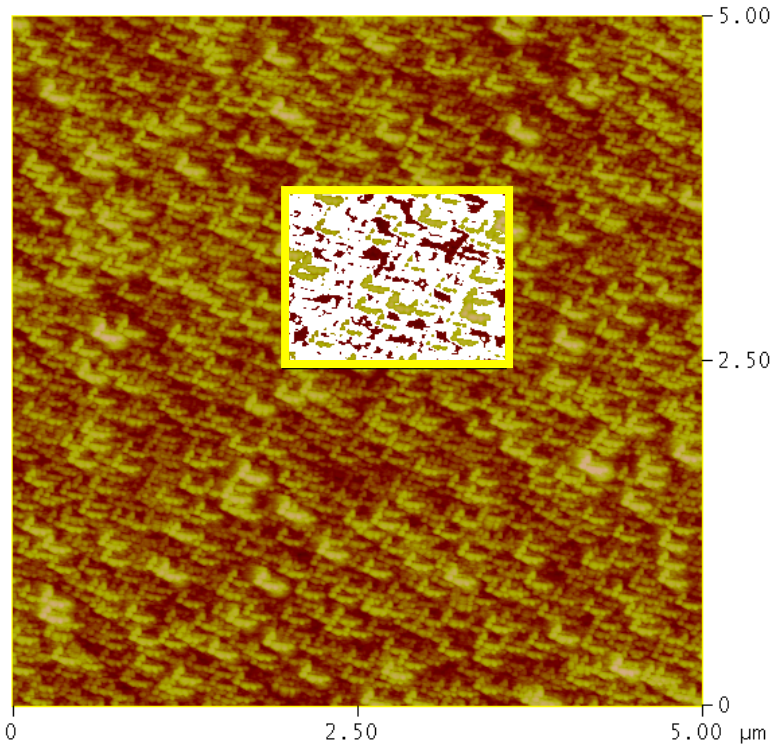

Figure 72: AFM image of T1346 (400 nm bulk BGaN with 0.9% boron – no smoothing or p-GaN cap) showing an RMS surface roughness of 5.301 nm (5.539 nm inside yellow box).

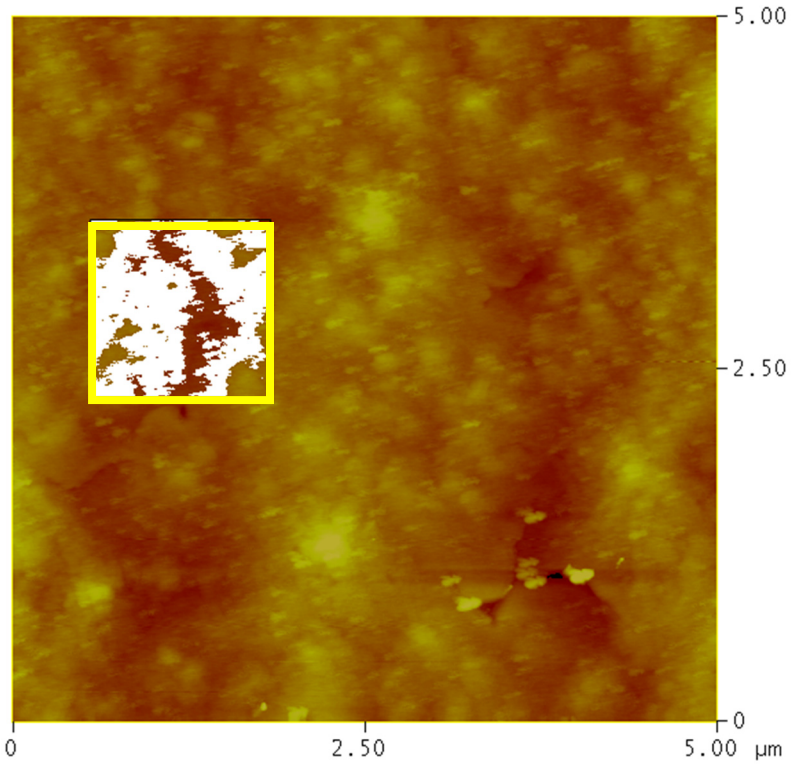

Figure 73: AFM image of T1353b (0.9% boron) showing an RMS surface roughness of 1.566 nm (1.099 nm inside yellow box).

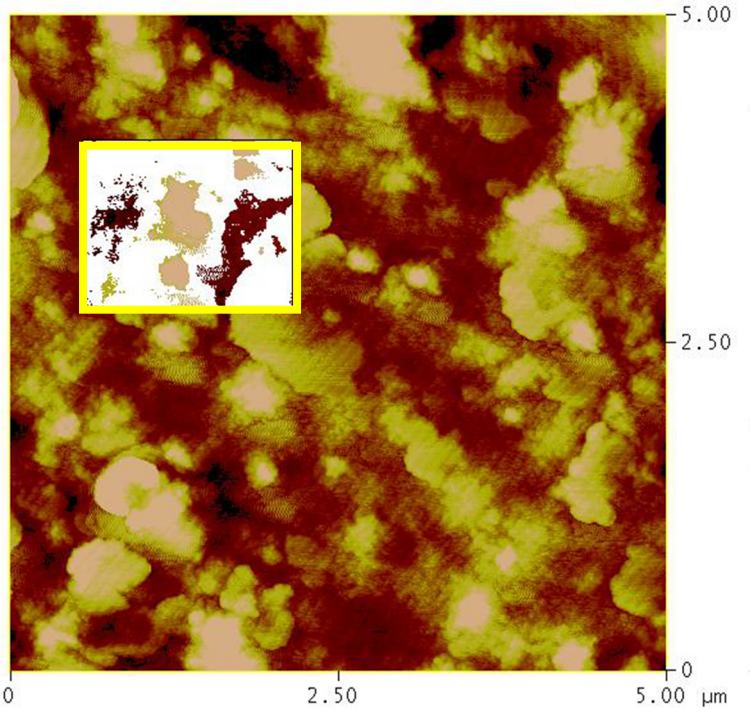

Figure 74: AFM image of T1379 (1.24% boron) showing an RMS surface roughness of 5.57 nm (6.02 nm inside yellow box).

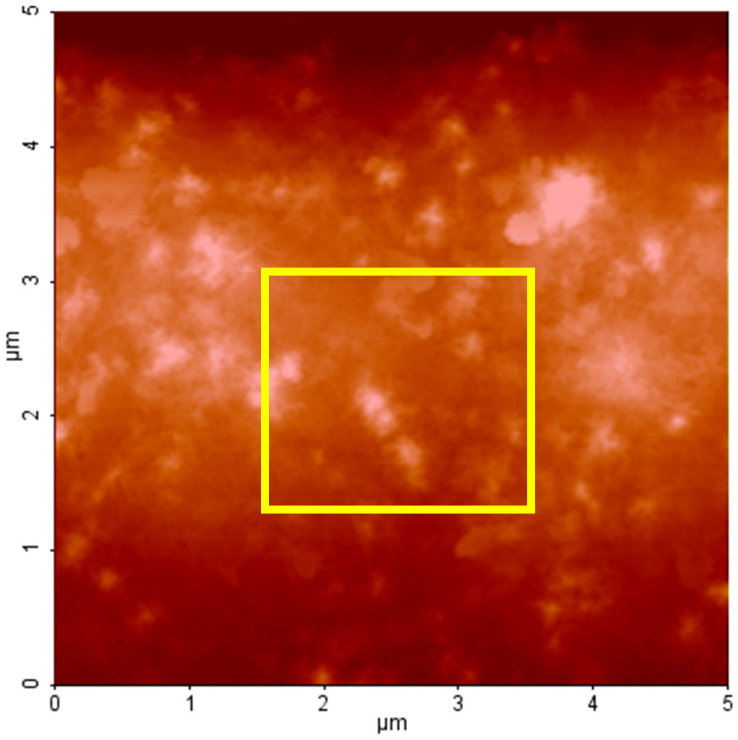

Figure 75: AFM image of T1382 (1.2% boron) showing an RMS surface roughness of 10.99 nm (3.3 nm inside yellow box).

In Figure 76 one can see the AFM results for T1403, which shows a very rough surface of around 34 nm RMS roughness (and about 32 nm roughness inside the yellow box). Again, this sample had a very thick BGaN intrinsic region (likely over 500 nm) and had a higher boron concentration than our good-quality T1353b sample. It is possible that, with a thicker smoothing layer (maybe 200 nm instead of 100 nm), this could have been smoothed out better. The issue of a high-incidence of cracking, however, would not have been solved by a thicker smoothing layer, of course.

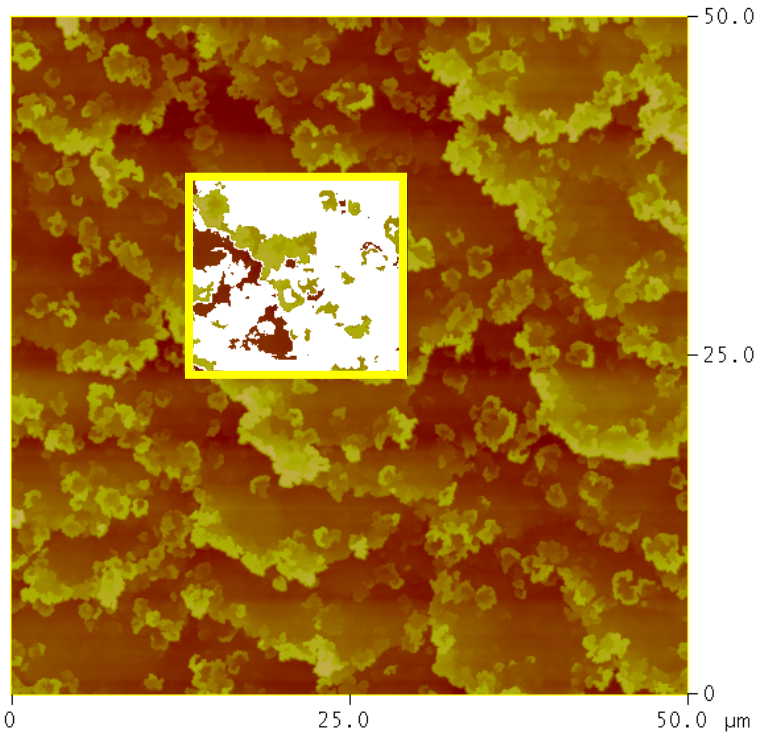

Figure 76: AFM image of T1403 (1% boron) showing an RMS surface roughness of 34.151 nm (31.789 nm inside yellow box).

Finally we can see in Figure 77 the AFM results for T1405b, which shows a similarly high-quality surface that was seen in T1353b. The RMS roughness here was about 3 nm overall, or 1.2 nm in the yellow box. This is not surprising, since T1405b and T1353b were grown to similar specifications.

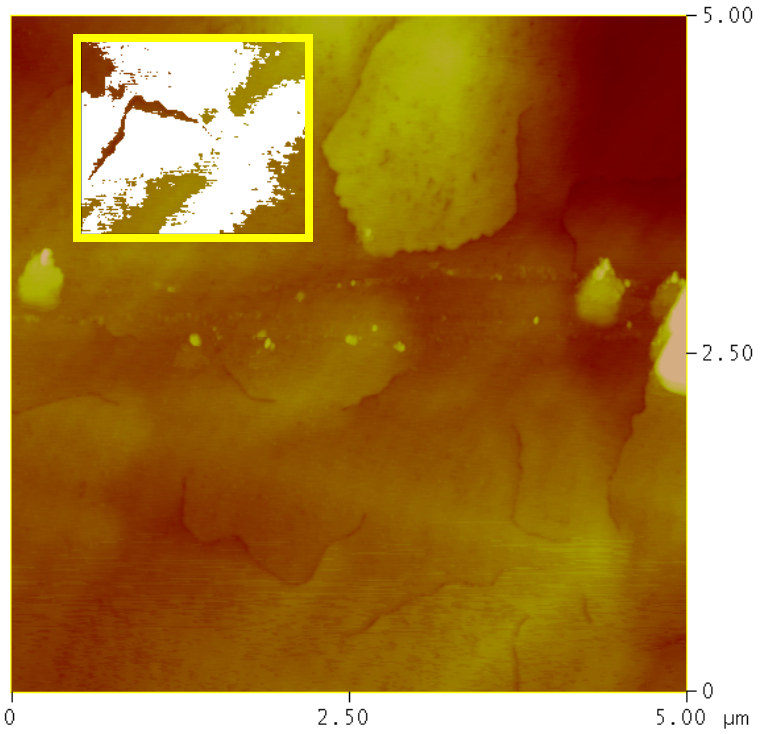

Figure 77: AFM image of T1405b (0.9% boron) showing an RMS surface roughness of 3.250 nm (1.257 nm inside yellow box).

A STEM study for T1353b was also performed in order to get a better idea of the material quality itself as it was grown. For instance, in Figure 78 one can clearly see the general boundaries between the BGaN (around 400 nm - yellow), p-GaN lateral growth layer (around 100 nm - red) and p-GaN cap (around 200 nm - green). Also seen here is a discoloration (marked with a white arrow) that denotes where the surface V defect originates deep within the substrate.

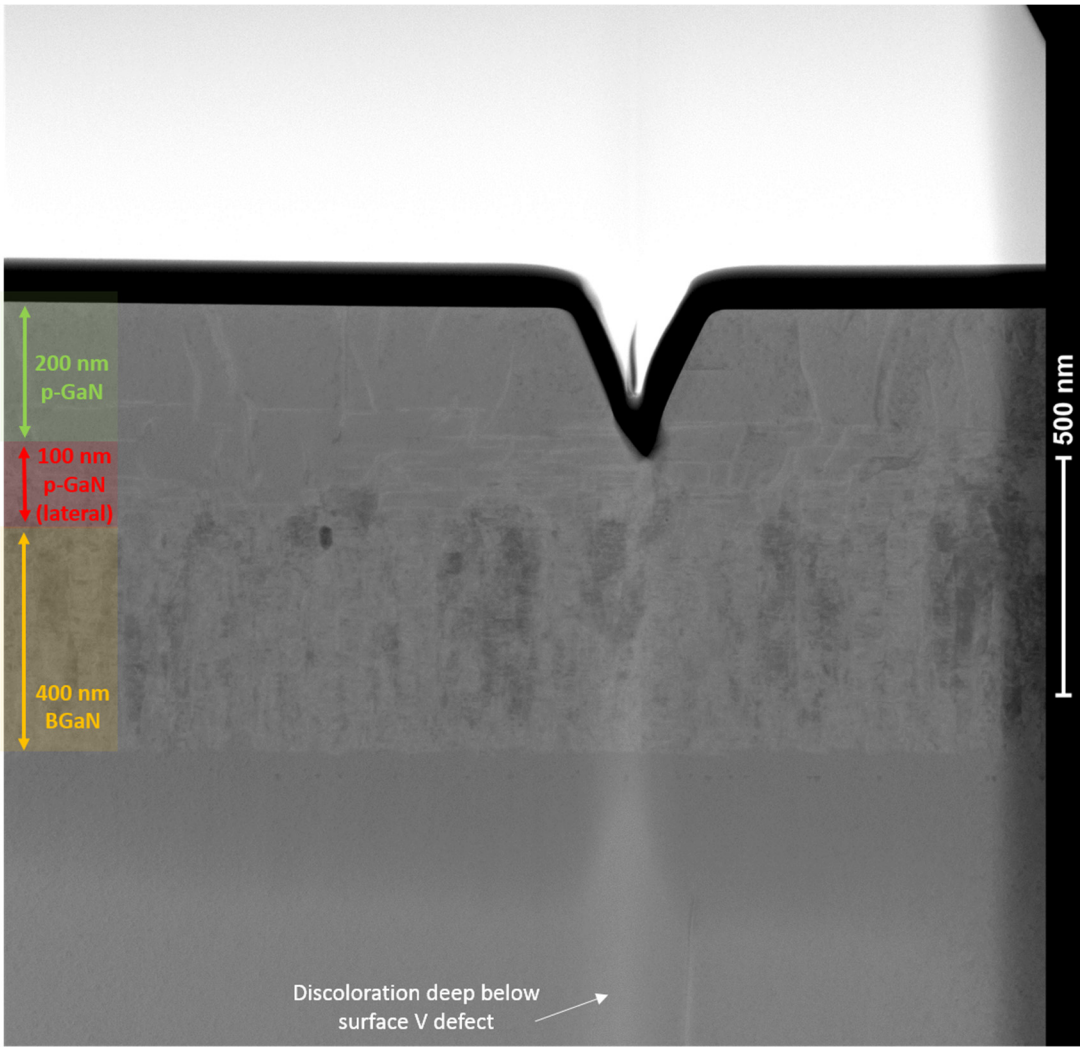

Figure 78: STEM HAADF image of T1353b showing effectiveness of BGaN smoothing layer.

A close-up can be seen in Figure 79, which shows that only a few defects are able to propagate to the surface through the later growth layer. This shows that the lateral growth layer is effective at stopping defects from propagating to the surface, and also that it effectively acts as a smoothing layer for the visibly-rougher BGaN region of the device.

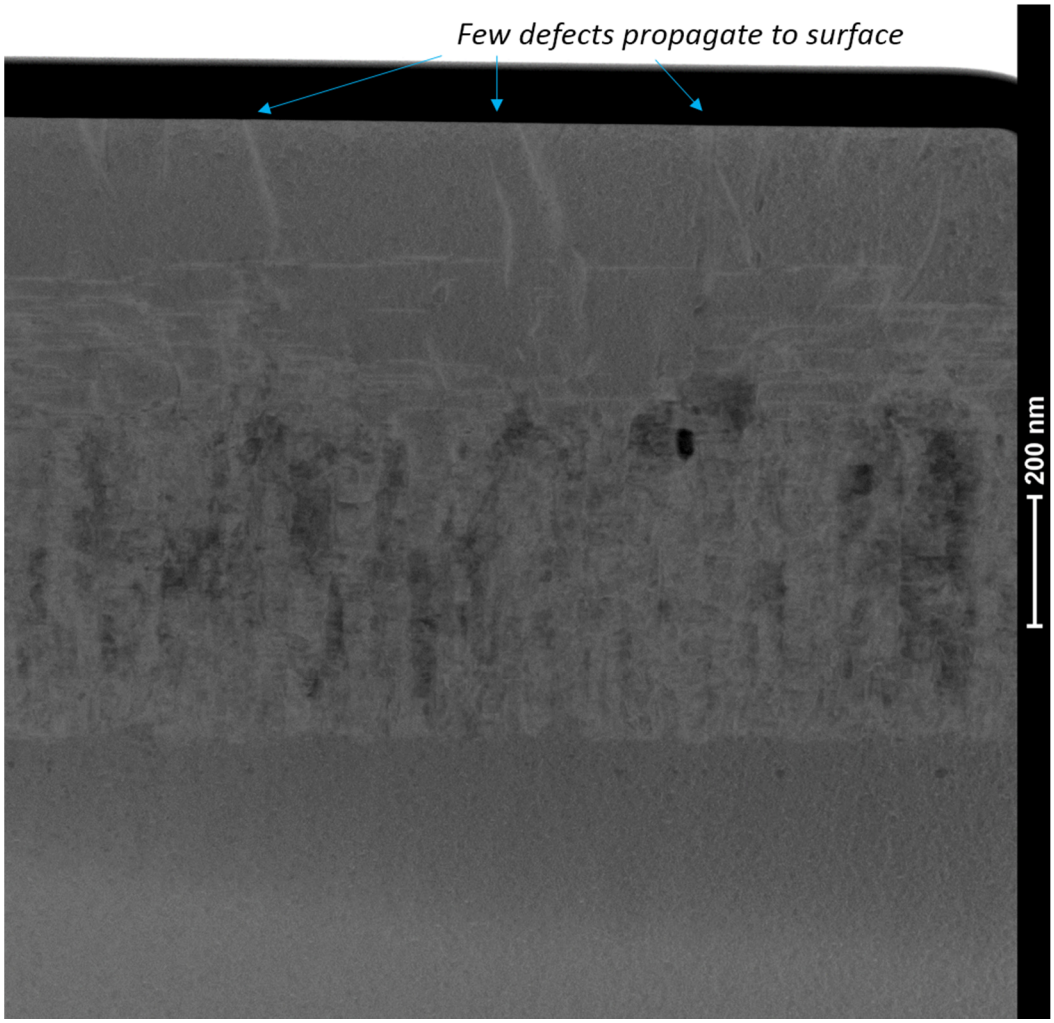

Figure 79: STEM HAADF image of T1353b showing defects successfully blocked by lateral growth layer, with very few making it to the device surface.

A close-up focusing on the BGaN-lateral growth interface can be seen in Figure 80, where the green arrow indicates the lateral-growth region, and the blue arrows indicate the BGaN region. One particular thing to note here is just how quickly the lateral-growth layer smooths out the rough BGaN surface – it can be seen that after only about 100 nm of lateral growth, the surface already looks very consistent and of a good quality.

Additionally, one can see here that the quality of the BGaN growth itself appears to be constant regardless of the thickness that the BGaN is grown: from within the first 100 nm onward, the BGaN material exhibits an amorphous appearance that maintains relatively the same appearance even after 400 nm of growth.

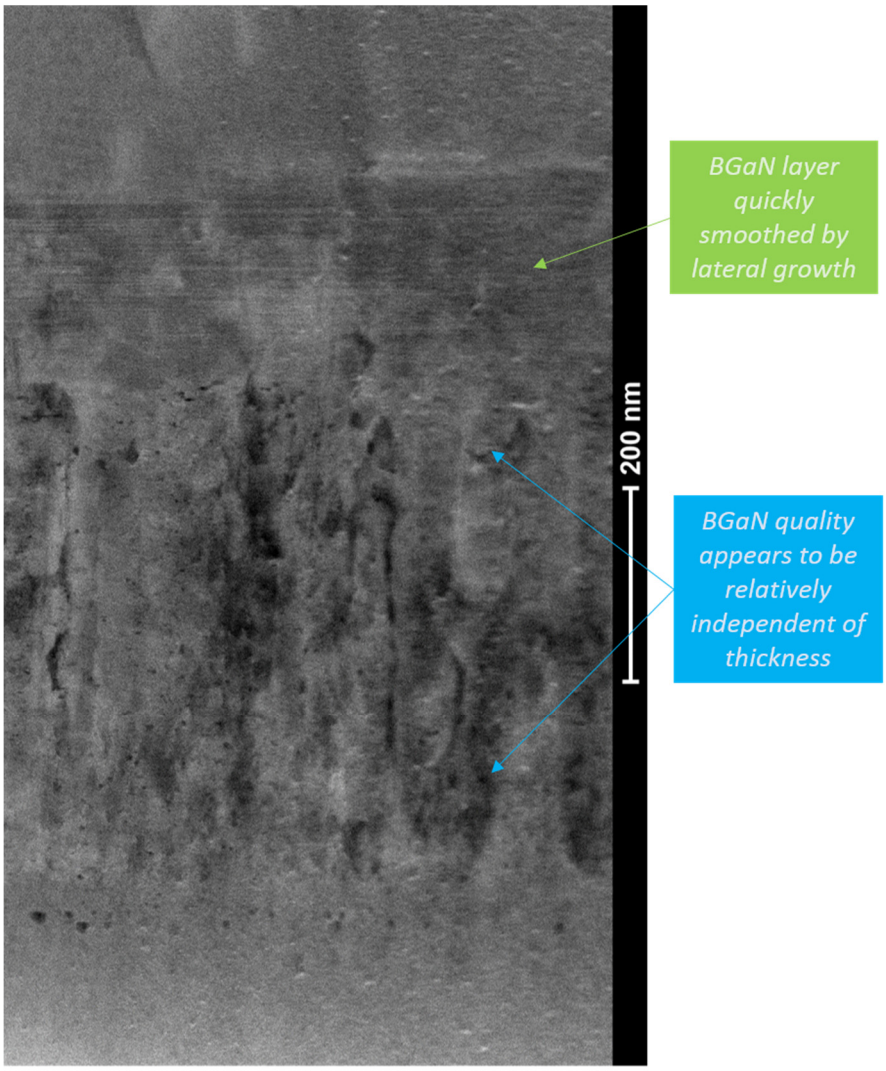

Figure 80: STEM HAADF image of T1353b showing consistent BGaN quality independent of BGaN thickness, and GaN smoothing layer clearly shown.

In Figure 81 we can see a similar image, but one which highlights the blockage of defects in the lateral-growth layer. As can be seen highlighted by the yellow arrow here, a defect originating from the BGaN layer is successfully blocked by the lateral-growth p-GaN layer. The red box in this figure denotes the close-up area on which Figure 82 is based.

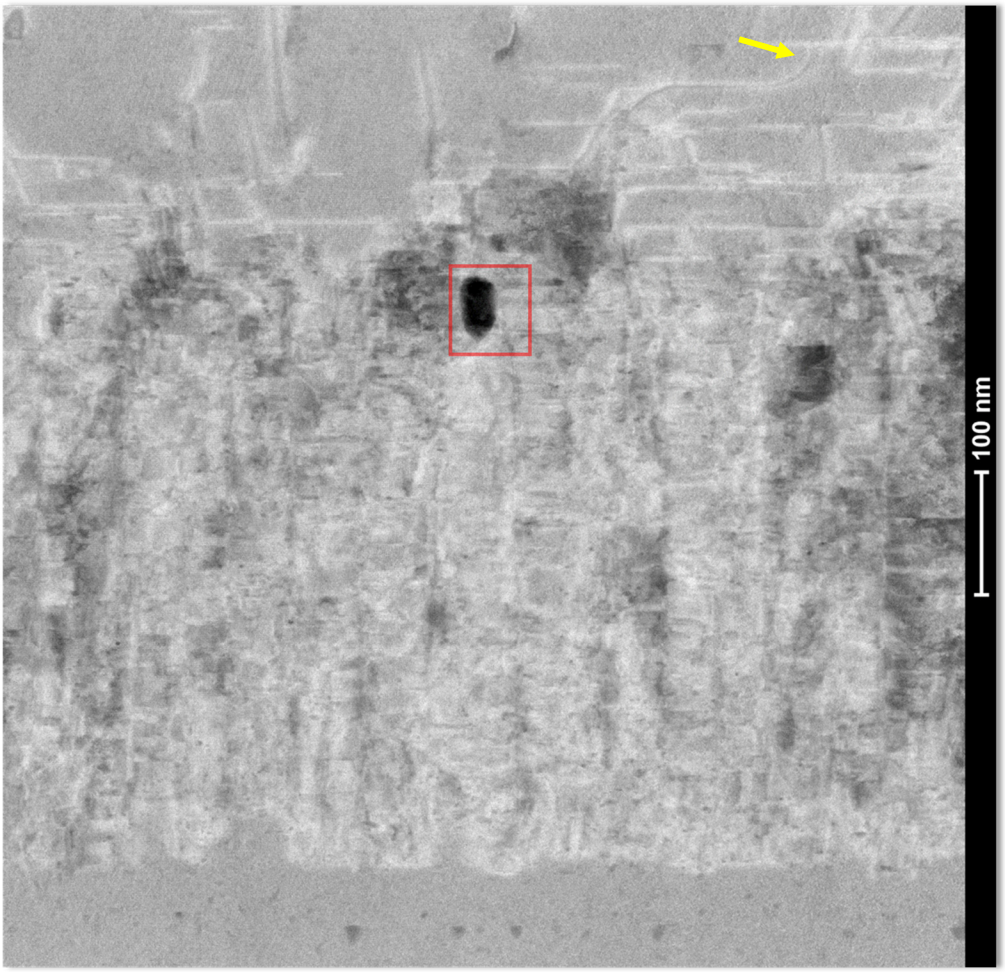

Figure 81: STEM HAADF image from T1353b showing blockage of defects during lateral growth phase. Yellow arrow highlights a blocked defect. Red box denotes area where Figure 82 is taken.

In Figure 82 one can see a close-up of the material gap (dark colored spot) from Figure 81. It should be noted that the crystalline quality of the BGaN is still clearly of a high quality here, even in the presence of a gap in the material.

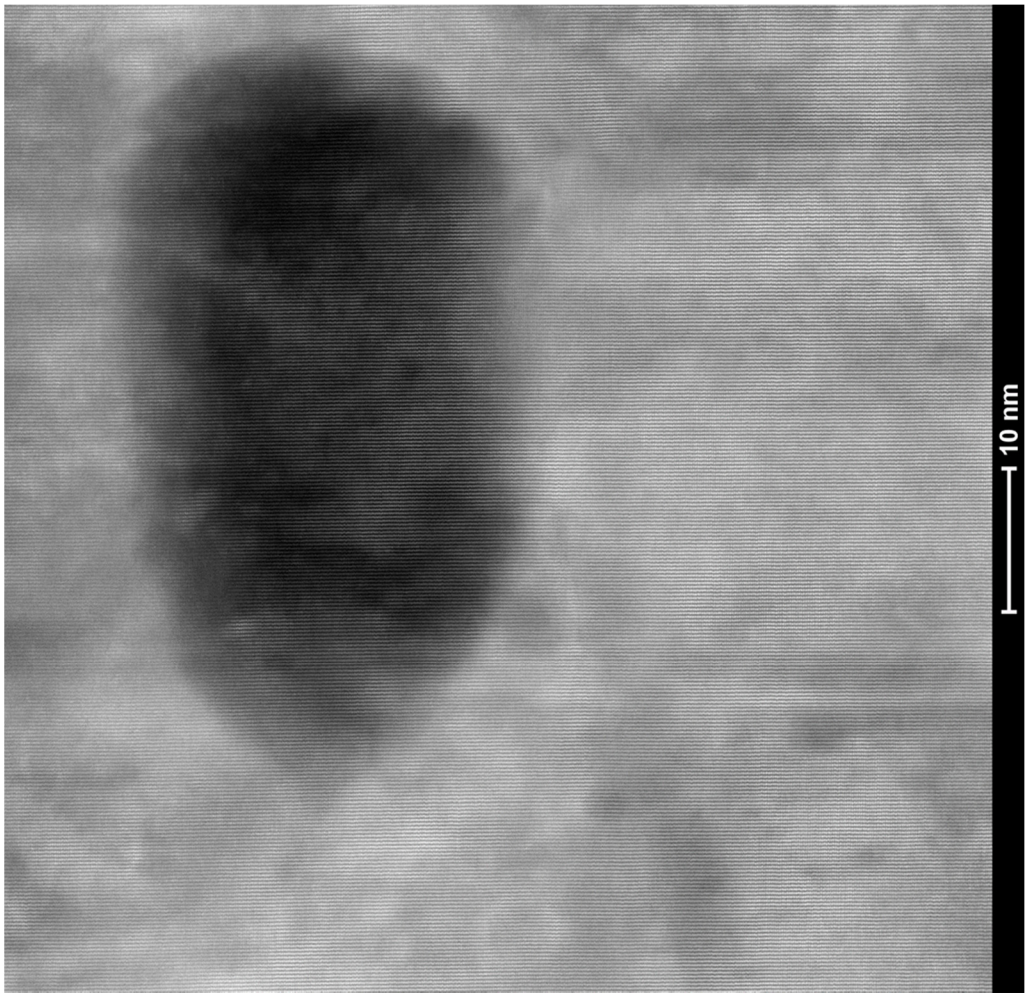

Figure 82: Close up STEM HAADF image of T1353b showing good crystalline quality of BGaN material even around gap in material (dark area).

Finally, Figure 83 shows the FFT plot based on the BGaN region as depicted in Figure 82. Similarly with the T1277 BGaN PIN sample (grown under H2), we can see a high-quality crystalline structure and a strong central peak, although it is clearly not as

high of a quality crystalline structure as T1277 was (since we have more extraneous strong peaks here).

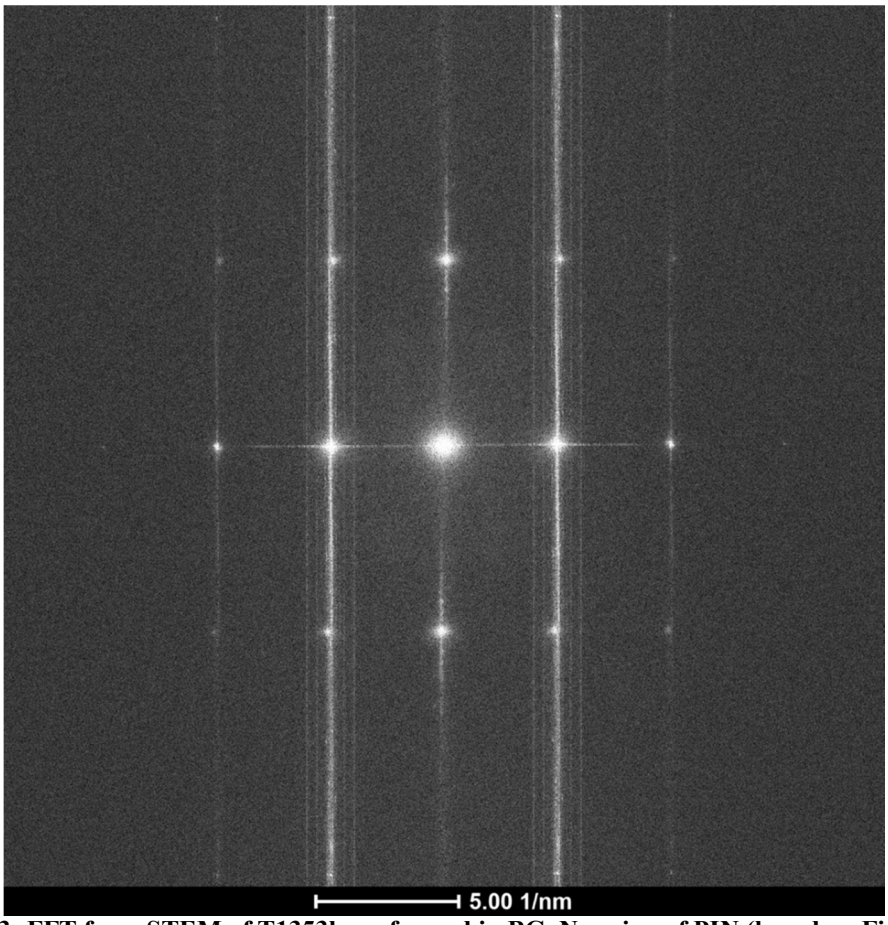

Figure 83: FFT from STEM of T1353b performed in BGaN region of PIN (based on Figure 82).

In summary, we have demonstrated the successful growth of a BGaN-based PIN structure grown under both hydrogen and nitrogen carrier gasses. The smoothing, lateral p-GaN growth layer was successful at smoothing out the rough BGaN surface and provides a good quality surface to perform p-GaN contacting on.

CHAPTER 5

FINAL DEVICE PROCESSING AND PACKAGING

Now that we have come up with various potential designs for a Ni-63 betavoltaic battery, the next step is to process and test these designs electrically. In the following sections we will discuss the designs that were used for battery testing, some processing techniques used, as well as the final product packaging.

Device Processing

Three different GaN-based PINs were grown, as seen in Figure 84, with a 200 nm intrinsic region (samples S0071 and S0109) and with a 600 nm intrinsic region (S0110). Our GaN material had an intrinsic carrier concentration that could only realistically support a thickness of up to approximately 200 nm, which is why such a thin intrinsic region was used in these devices. The 600 nm intrinsic region device was created as a "reach" device, though performance was expected to be poor due to a high recombination rate in the intrinsic region (since the built-in electric field would not be strong enough to span the entire intrinsic region).

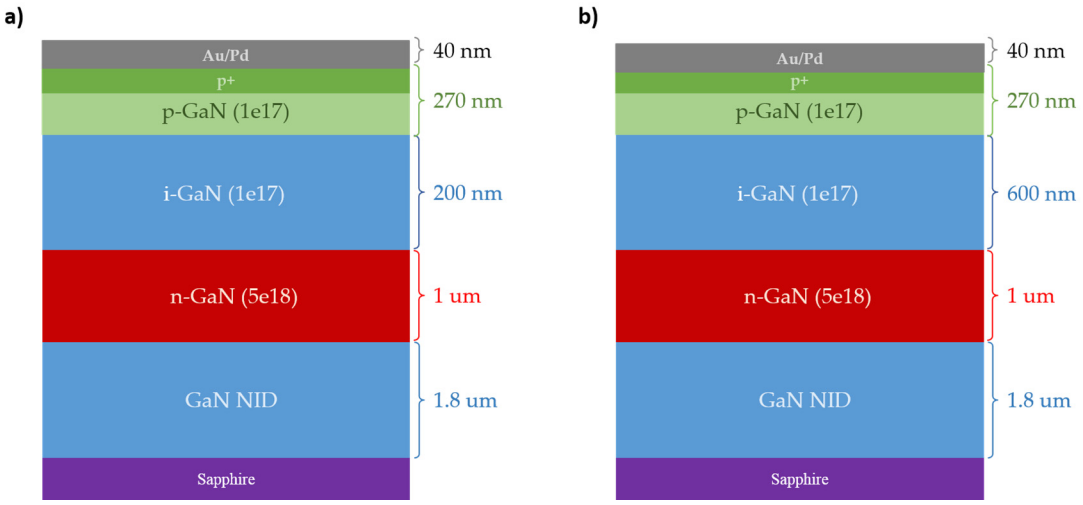

Figure 84: Device structures for a) S0071 and S0109 and b) S0110 GaN PIN devices.

In Figure 85, one can see the aforementioned T1405 BGaN PIN structure, with a 500 nm intrinsic region (400 nm BGaN and a 100 nm lateral-growth GaN region).

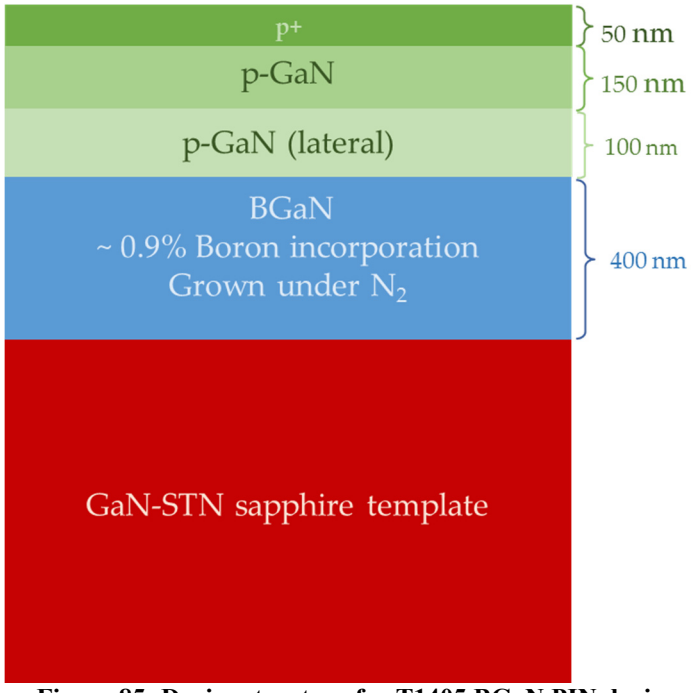

Figure 85: Device structure for T1405 BGaN PIN device.

Finally, in Figure 86 and Figure 87, one can see the processing design used for the S0071 sample. This device was processed in the Georgia Tech lab facilities in Atlanta, GA, and features Ti/Al n-GaN contacts and Ni/Au p-GaN contacts. The spreading layer here is 30 nm thick, in order to minimize Ni-63 absorption.

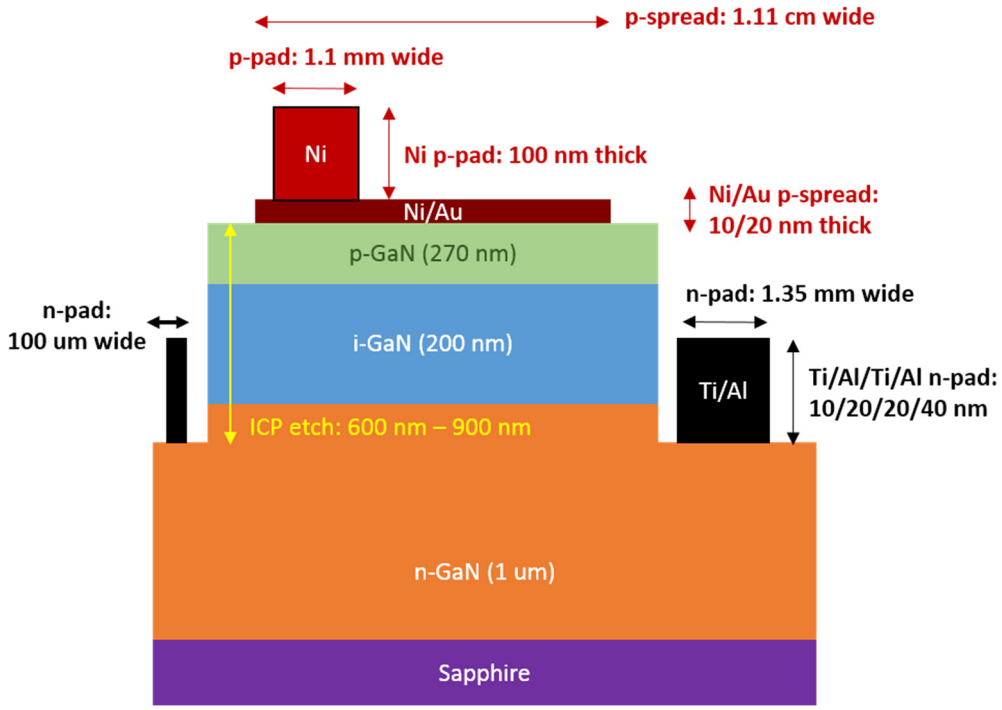

Figure 86: Processing and contacting for S0071 GaN PIN samples (side view) – not to scale.

The surface area of the spreading layer of the device (where the majority of the beta particles will enter through) is designed to be very large (approximately 1 cm^2) in order to match the size of our Ni-63 source, which is slightly larger than 1 cm^2, and to maximize power flux through the device.

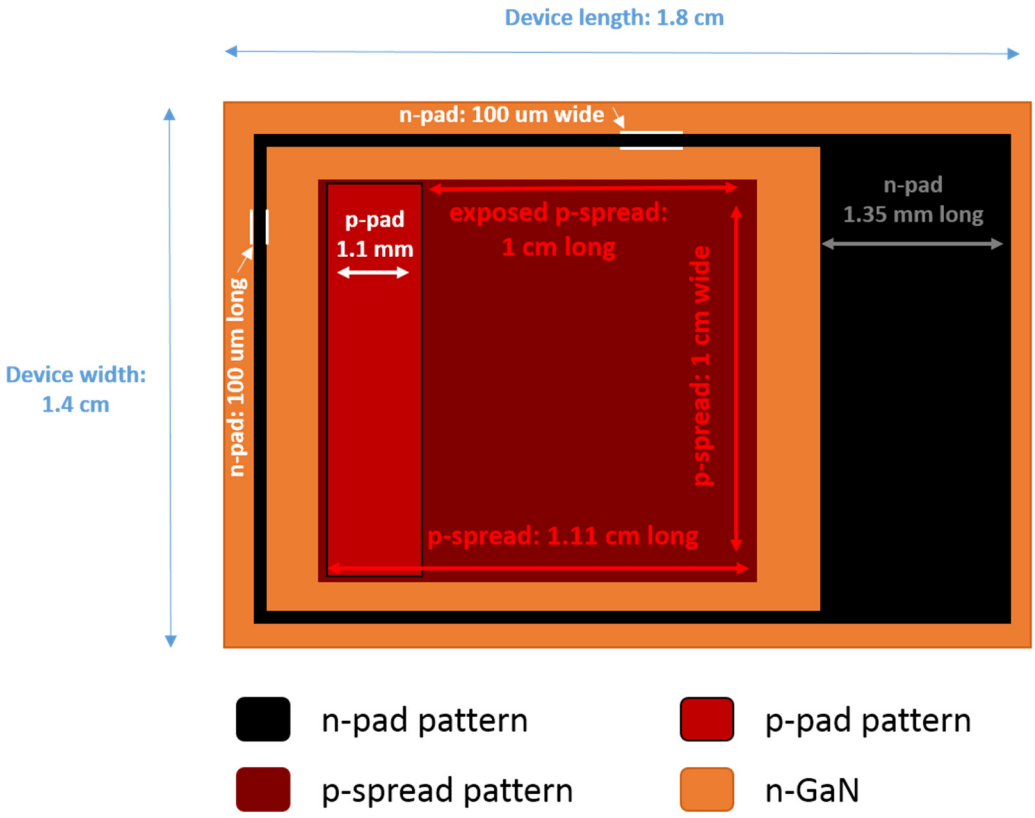

Figure 87: Processing and contacting for S0071 GaN PIN samples (top view) – not to scale.

The S0109, S0110 and T1405 devices were process by our partner lab, LPN, and we therefore do not have access to these designs as they are proprietary.

A photograph of an S0071 device can be seen in Figure 88, where the device has been mounted on a PCB board and wire bonded to the PCB contacting pads. Similarly, Figure 89 and Figure 90 show the GaN-based PINs of S0109 and S0110, respectively. Although the specifics of the design are different, the dimensions are similar (notably, the spreading layer is approximately 1 cm^2 in size).

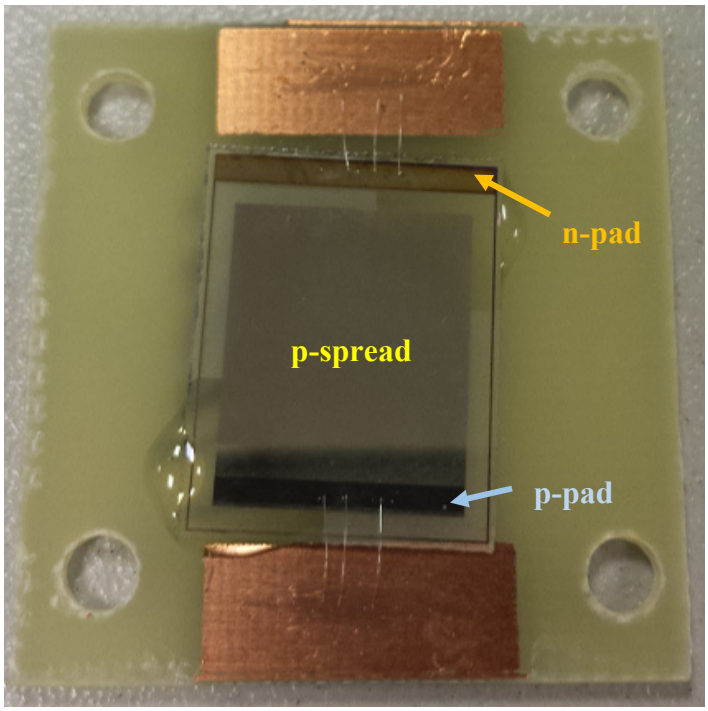

Figure 88: An S0071 GaN PIN device after processing, contacting and being wire-bonded and mounted on a PCB board.

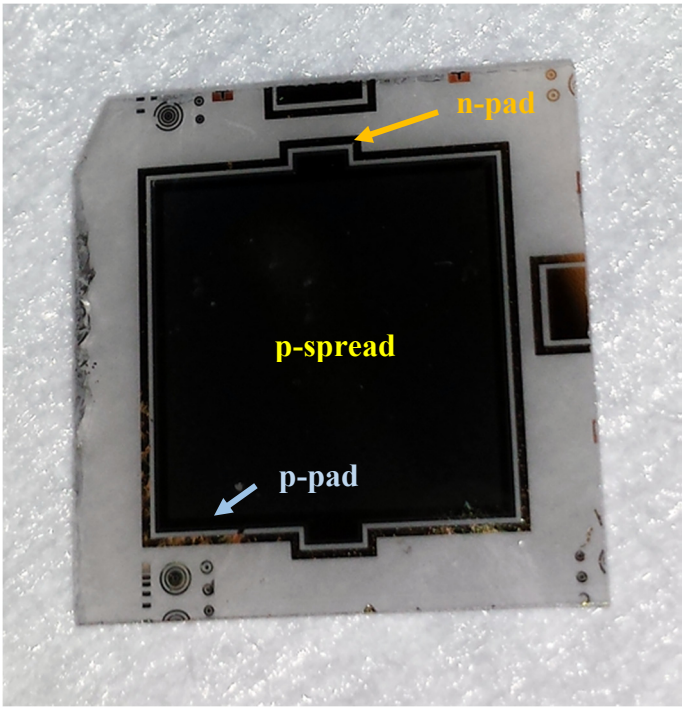

Figure 89: An S0109 GaN PIN device after processing and contacting (non-annealed).

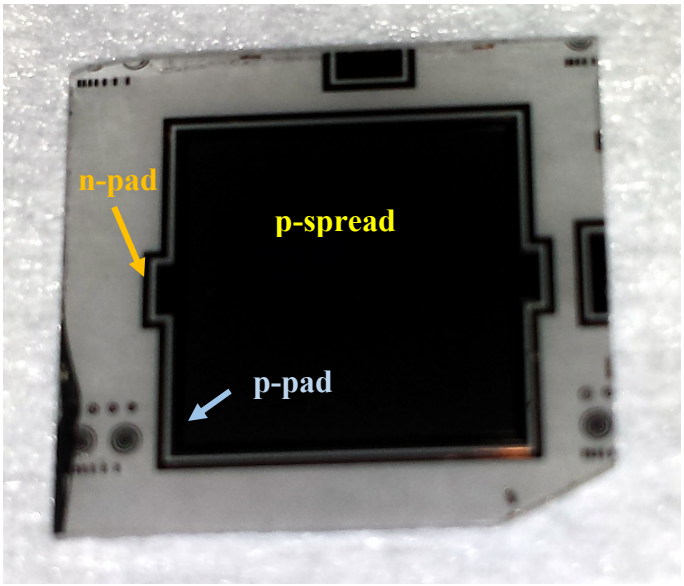

Figure 90: An S0110 GaN PIN device after processing and contacting (non-annealed).

Finally, Figure 91 shows a BGaN PIN device, processed similarly to S0109 and S0110, except the device is approximately 4x4 mm^2. A smaller size was used because only two ¼ wafers were grown due to time constraints (rather than a full 2" wafer). The sample shown has been both annealed and baked (thus giving it a darker color).

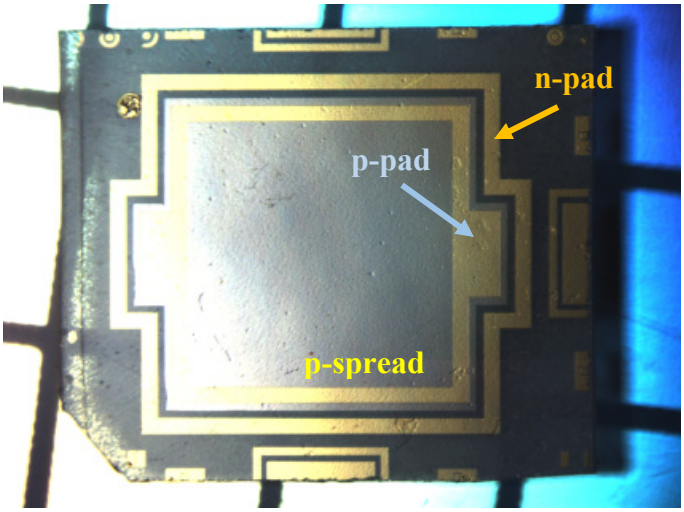

Figure 91: A T1405 BGaN PIN device after processing and contacting (after annealing and baking).

3D-Printed Experimental Package

In order to have an easy testbed for the real Ni-63 betacurrent tests, a convenient package had to be created that would allow efficient glovebox operation. This section will detail some 3D printed designs that were created for the BATGaN project in order to fulfill this requirement.

In Figure 92, an angled view of the 3D printed package can be seen. Notice here that the Ni-63 holder can be slid in and out of the package via the tray (bottom left). The package has a device on both the top and bottom halves of the package. This can be seen more clearly in Figure 93 (side view), where the top and bottom halves are sandwiched around the Ni-63 source.

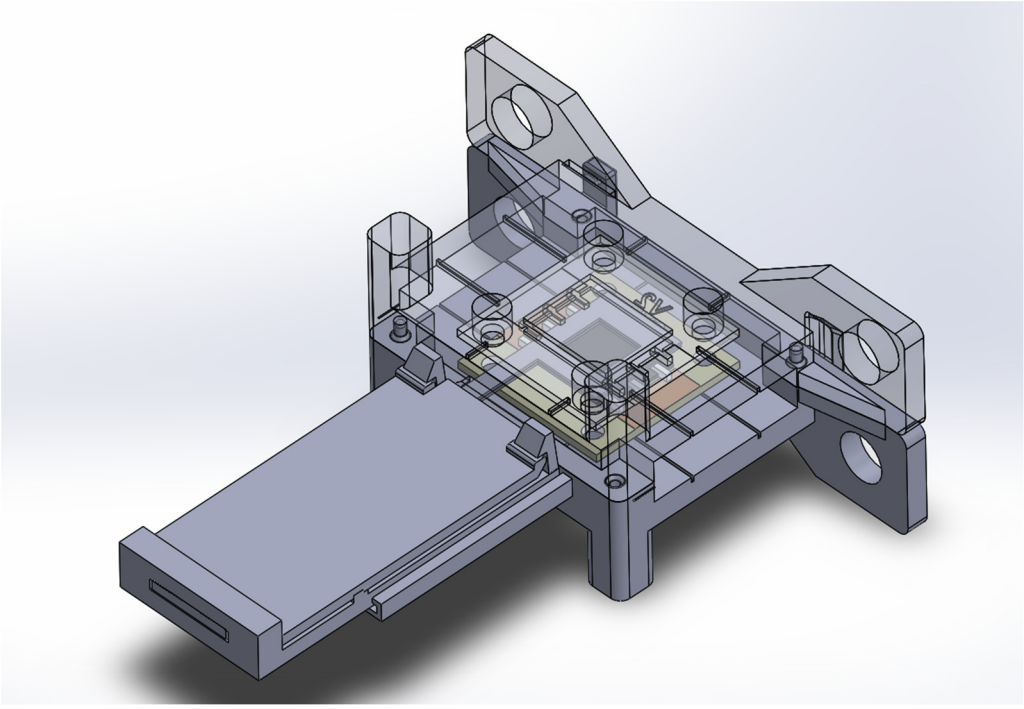

Figure 92: A 3D model of the 3D-printed testing box design (angled view).

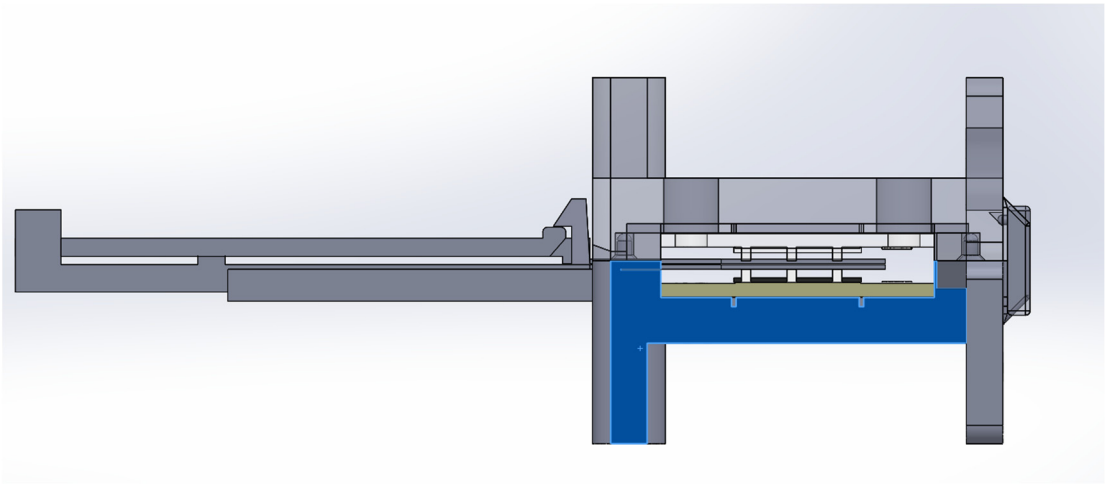

Figure 93: A 3D model of the 3D-printed testing box design (side view).

Finally, Figure 94 shows a top view of the 3D printed device design, which more clearly shows the device PCB (yellow) and the Ni-63 holder position relative to the device.

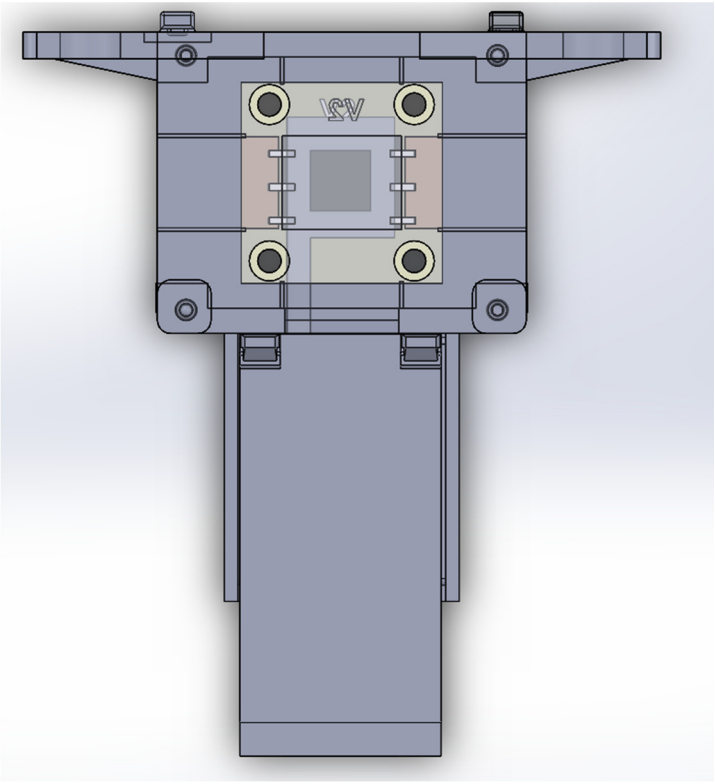

Figure 94: A 3D model of the 3D-printed testing box design (top view).

Fully-Assembled Packages

The aforementioned designs were next sent to the 3D printer at our partner research company Institut Lafayette, in order to be fabricated. The end result can be seen in Figure 95, which shows the top box (left), bottom box with Ni-63 holder inserted (right) and screw mechanism. Here the S0071 GaN PIN devices were mounted onto PCB boards and inserted into the 3D printed packaging.

Note that the screw mechanism here allows for the devices to be raised and lowered so that they are closer to or farther from the Ni-63 source holder. This allows us to vary the distance, and thus the power, delivered to the devices. It also allows for easier loading of the devices and Ni-63 source, and to help prevent damage to the wire bonding upon loading.

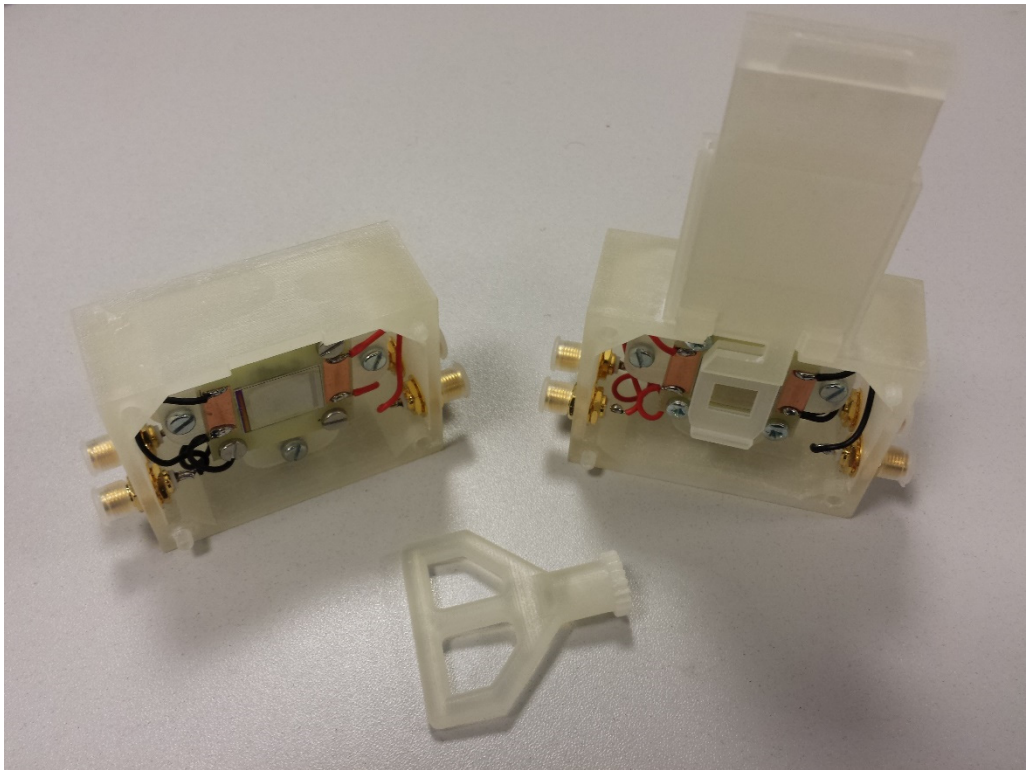

Figure 95: Testing box, allowing for raising and lowering of device platforms and thereby increasing or decreasing distance to Ni-63 source. S0071 devices shown installed.

The top and bottom boxes can be seen in Figure 96, but this time with the S0109 devices loaded. Note here that insulated cables were used to prevent signal noise during the measurements.

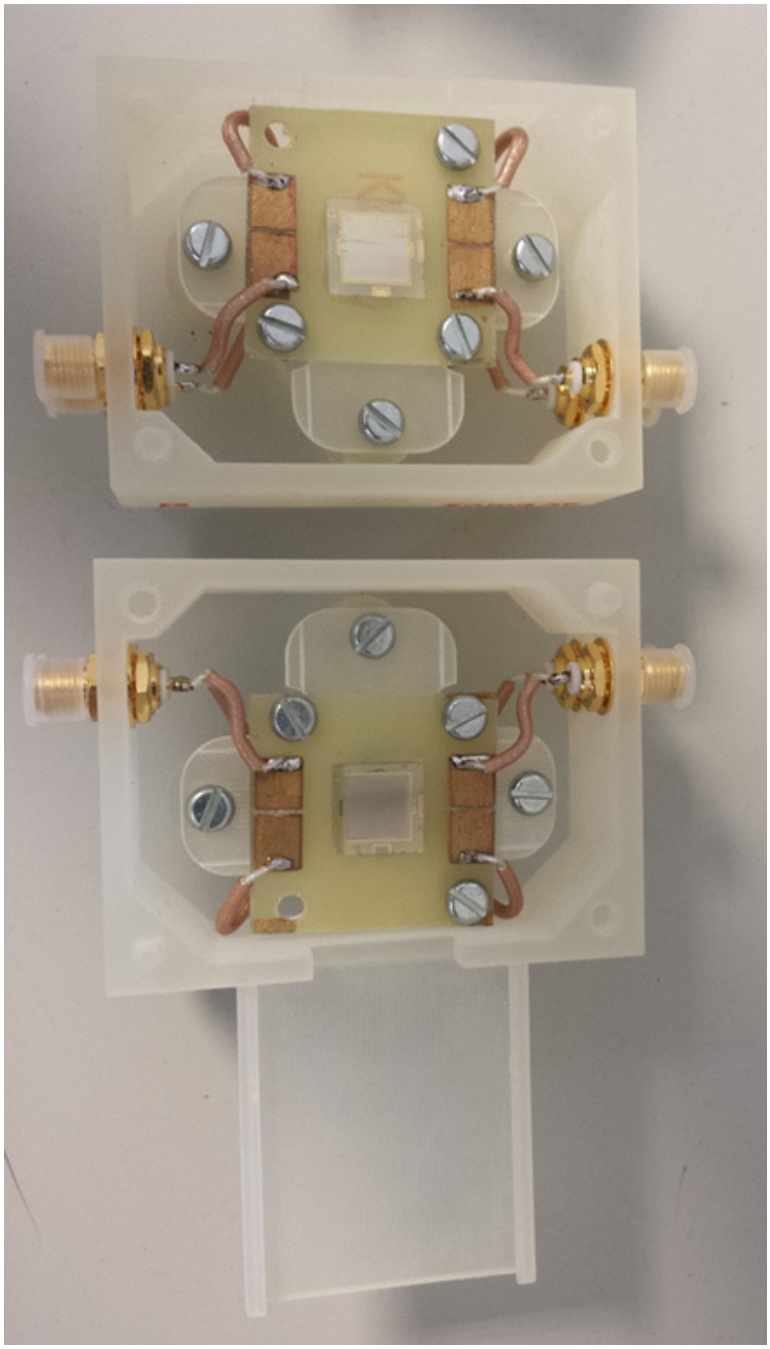

Figure 96: Testing box, S0109 devices shown installed (before wire bonding).

Figure 97: Ni-63 holder, with mock Ni-63 sample enclosed (in purple).

In Figure 97 one can see a close-up of the Ni-63 holder. The holder is designed to snugly fit a thin layer of Ni-63 foil and slide into the tray (as seen in Figure 96).

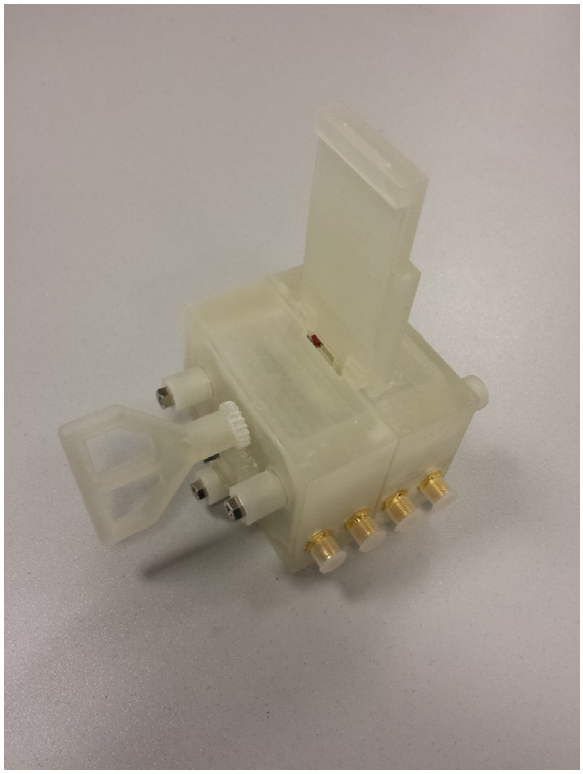

Figure 98: Testing box, closed. Shows screw mechanism in place that allows for raising and lowering of device platforms.

And finally, Figure 98 shows the fully-assembled 3D printed package, with both screw mechanism and Ni-63 holder inserted.

In conclusion, in this chapter we have discussed the devices that will be used for the final device testing, as well as gave an overview of the 3D printed packaging that was designed to help streamline glovebox testing for the official Ni-63 tests.

CHAPTER 6

STUDY OF FINAL DEVICE ELECTRICAL PROPERTIES

In this chapter we will discuss the electrical characterizations of the devices that were discussed in the previous chapter. This includes the device IV characteristics, SEM and EBIC-based characterizations, and Ni-63 tests that were performed.

Device Dark IV Characteristics

In order to get a baseline of the device performances, dark IV testing had to be done. The IV characteristics for the S0071.1 (first 2" wafer) GaN PIN (200 nm intrinsic) can be seen in Figure 99 and Figure 100, showing the IV and log-IV curves, respectively.

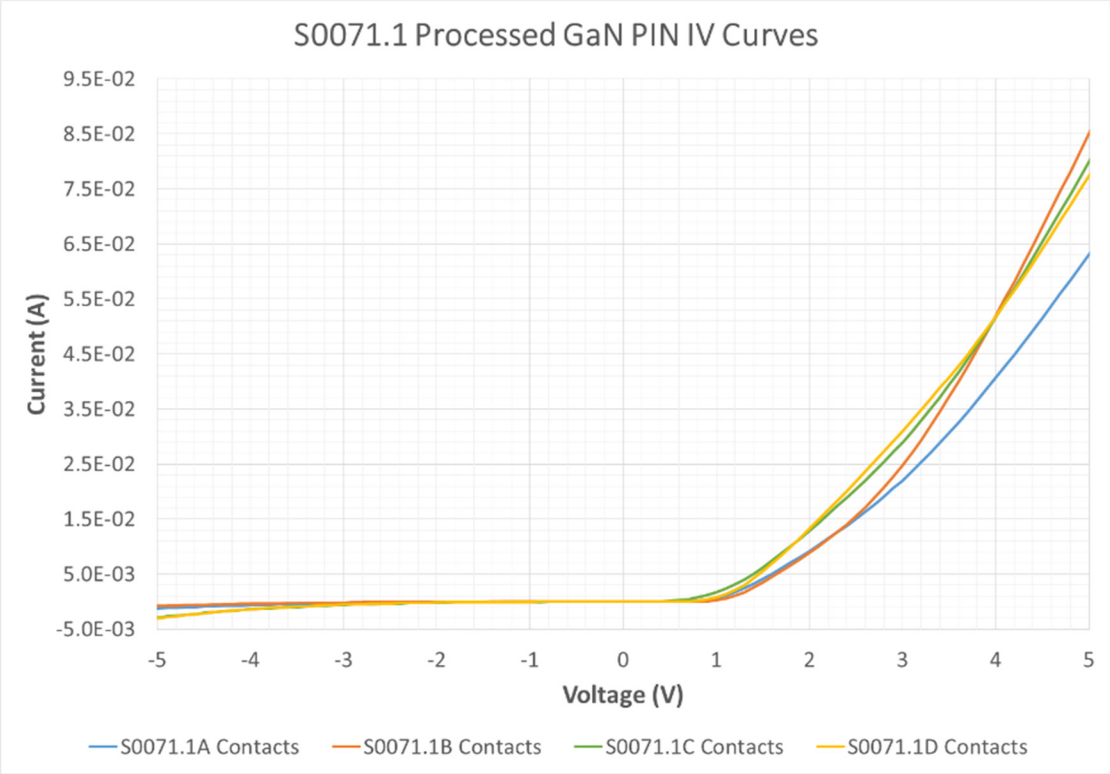

Figure 99: Dark IV Curves for GaN PIN S0071.1.

Note that S0071.1 was cut into four devices (A, B, C and D). For these devices, it can be see that the turn on voltage is quite low (around 1 V) and the leakage current is rather high (approximately 10 nA). This is likely due to issues with processing, since no passivation was used (due to time constraints), which resulted in a high leakage of the PIN.

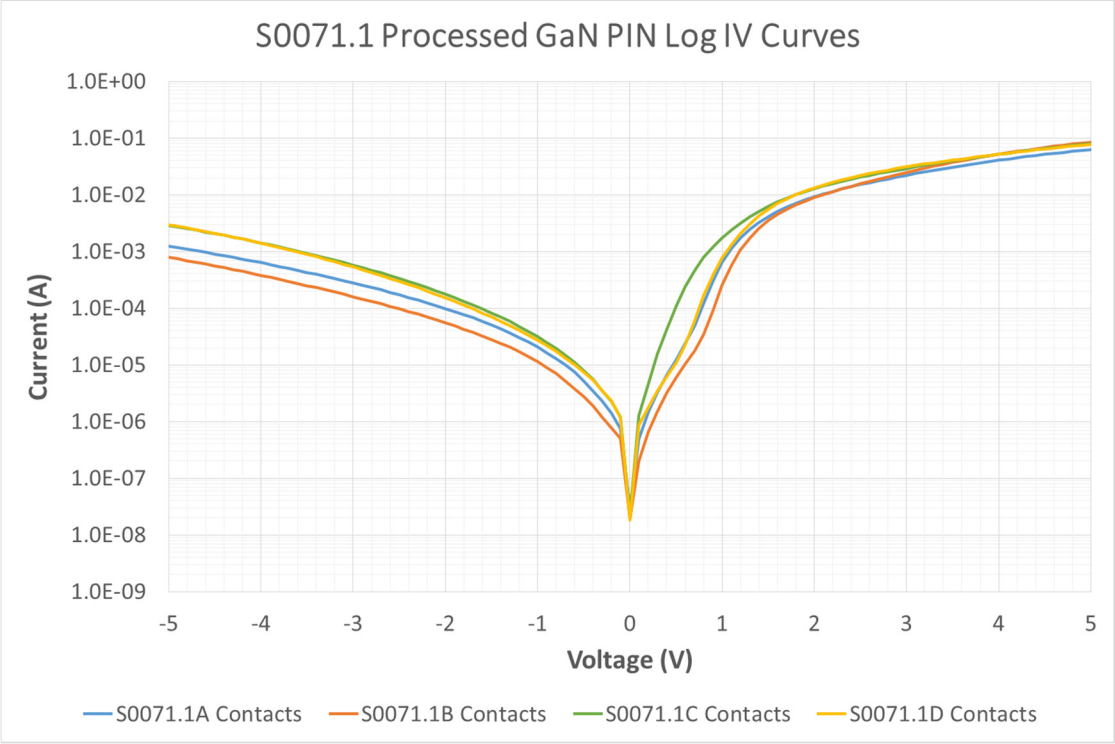

Figure 100: Log-IV Curves for GaN PIN S0071.1.

Similarly, Figure 101 and Figure 102 show the IV and log-IV curves for S0071.2 (second 2" wafer), respectively. Note here a very similar performance (as expected) with the S0071.1 devices, except S0071.2C (in green), which had a point defect which significantly reduced its performance.

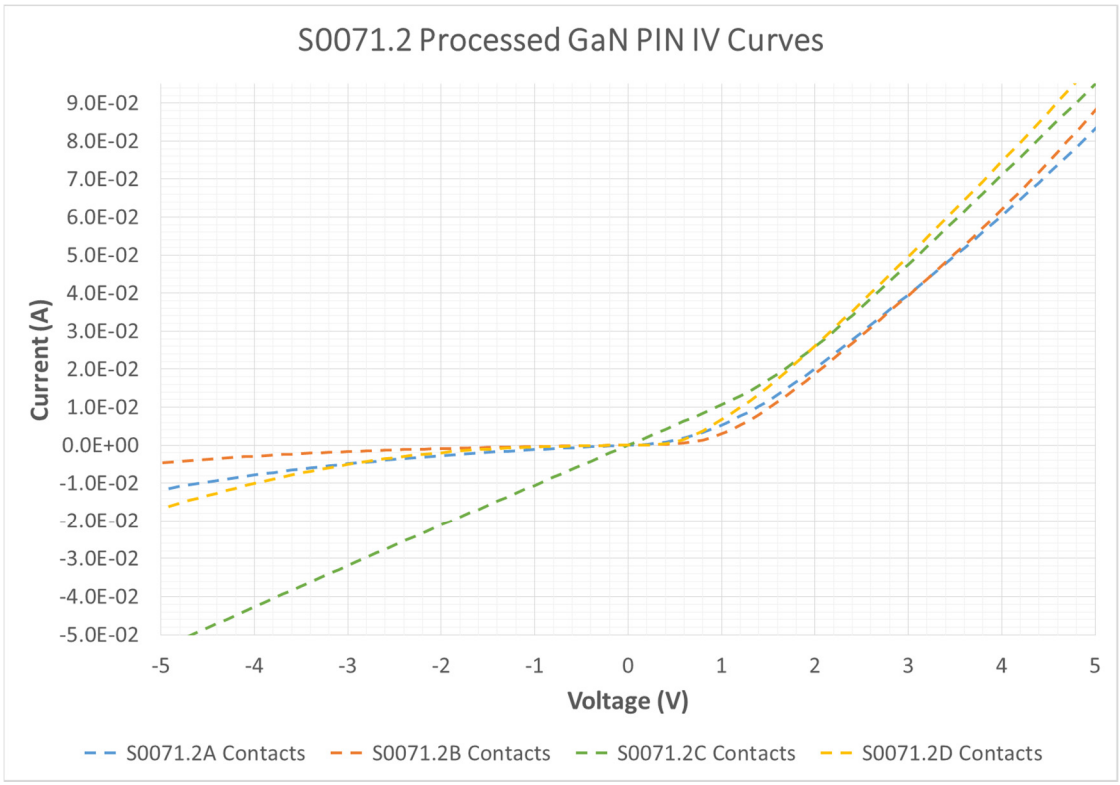

Figure 101: Dark IV Curves for GaN PIN S0071.2.

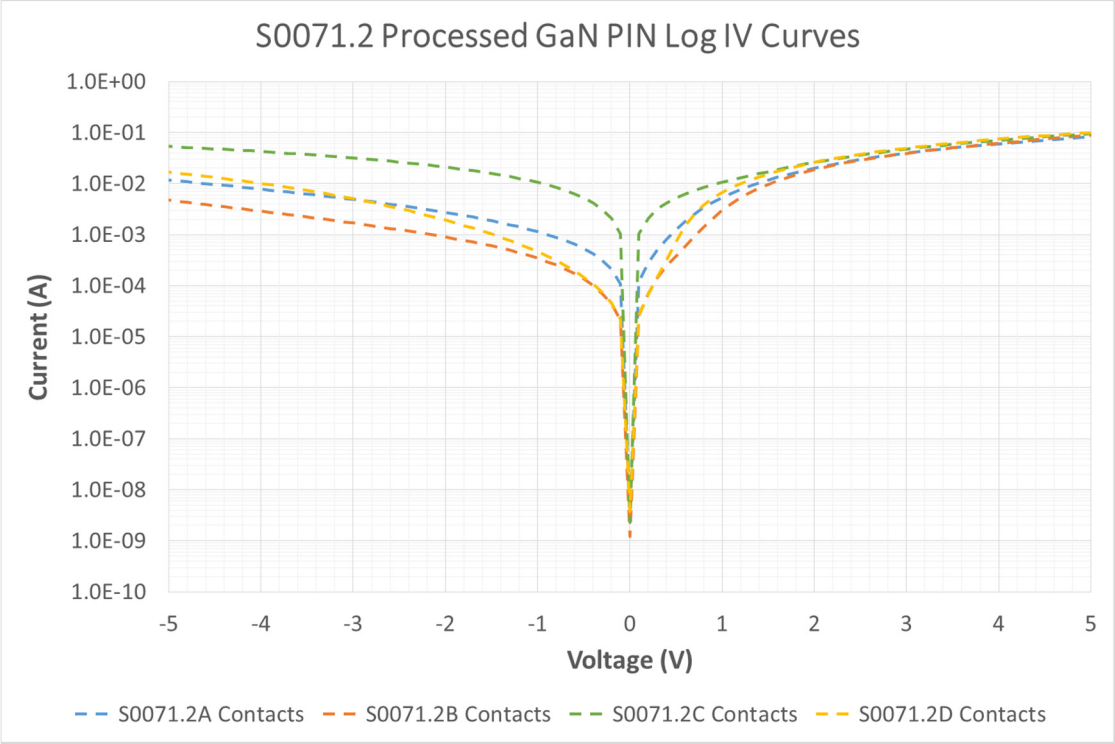

Figure 102: Log-IV Curves for GaN PIN S0071.2.

The S0109A and S0110A (200 nm intrinsic and 600 nm intrinsic PIN devices, respectively) can be seen in Figure 103 (IV) and Figure 104 (log-IV). These devices were processed by our partner lab, LPN, and exhibits a significantly improved performance. Note that S0109A has a turn on voltage around 2.5 V, and a leakage current of around 10 pA. The S0110A device, however, has a turn on voltage that is closer to only 1 V and a leakage around 10 nA. This is in line with expectations, since the intrinsic region is too thick for our material quality and thus there is a high amount of recombination.

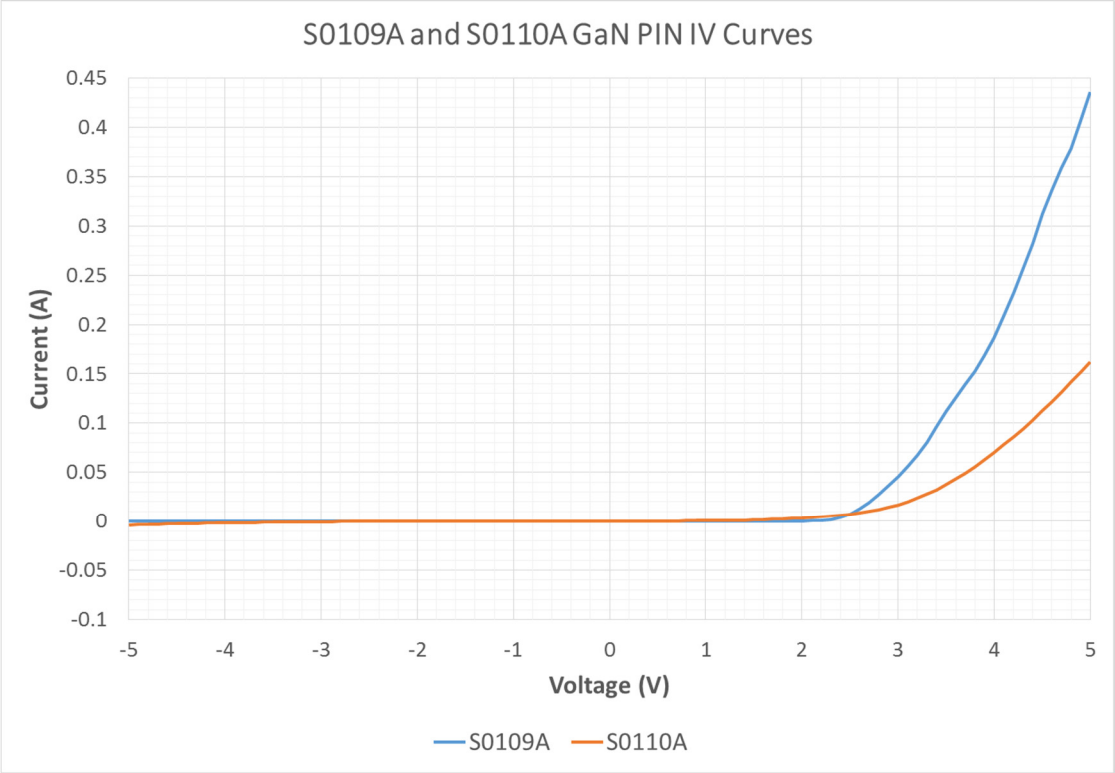

Figure 103: Dark IV Curves for GaN PINs S0109A and S0110A.

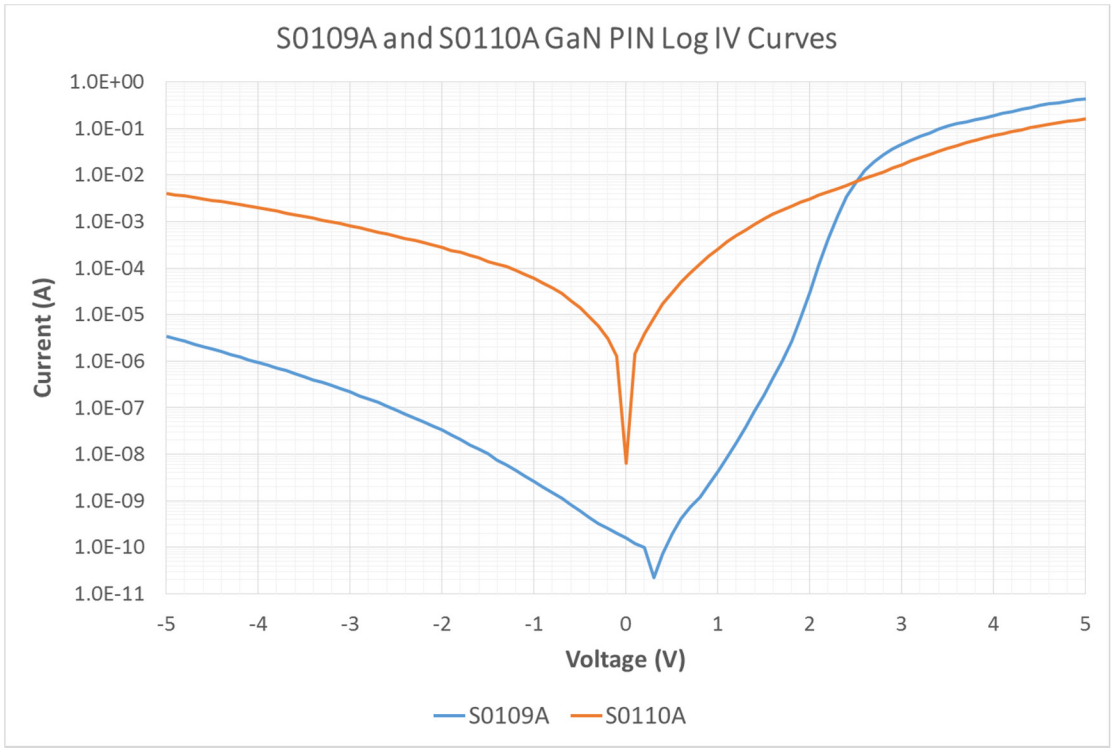

Figure 104: Log-IV Curves for GaN PINs S0109A and S0110A.

A second wafer of S0109 and S0110 (denoted as S0109B and S0110B) were also processed by our partner lab, LPN. The IV and log-IV curves for these devices can similarly be seen in Figure 105 and Figure 106, respectively. Note the similar performance with the first wafer (A), though a higher leakage current for S0109B (versus S0109A) of approximately 1 nA (instead of 10 pA). This difference is possibly due to scratches that occurred to the contacts during EBIC testing, which may have resulted in a small short circuit between the n and p contacts. A difference in processing or material quality could also explain the difference between these two devices.

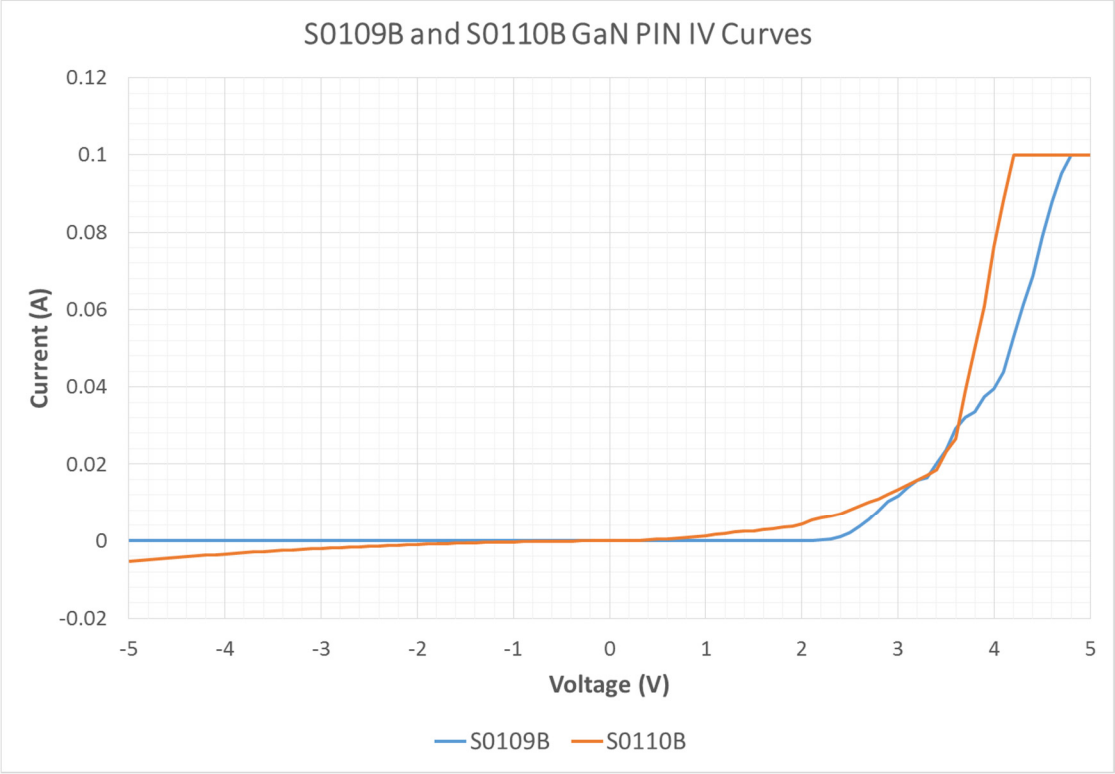

Figure 105: Dark IV Curves for GaN PINs S0109B (non-annealed) and S0110B (non-annealed).

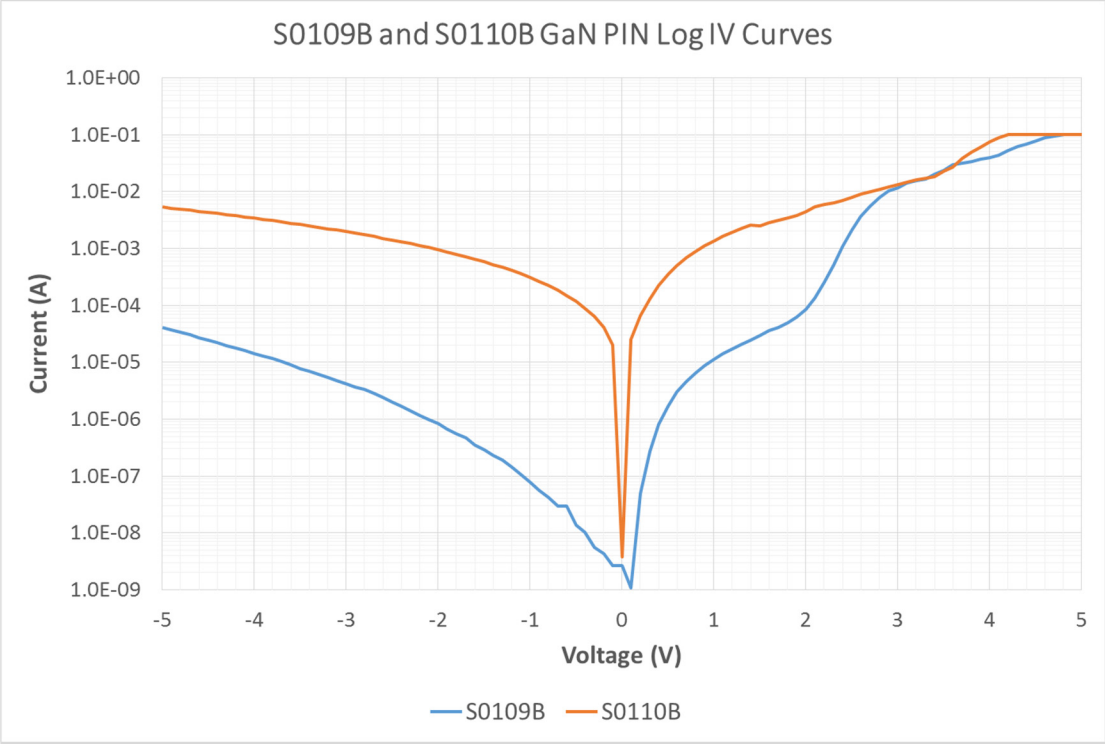

Figure 106: Log-IV Curves for GaN PINs S0109B (non-annealed) and S0110B (non-annealed).

Finally, IV testing of the BGaN PIN, T1405b, can be seen in Figure 107 and Figure 108 (again, IV and log-IV, respectively). This show a turn on voltage of only around 0.5 V and a leakage of around 10 nA, which are comparable to the 600 nm intrinsic GaN PINs (S0110A and B). The low turn on voltage is likely due to processing, since the BGaN PINs had a p-GaN region that was 150 nm thick, while the GaN PINs had a p-GaN region that was 270 nm thick. The same contacting specifications were used for both devices (in the interest of time) and the contacts were not optimized for the BGaN PIN devices. With further contact optimization, it may be possible to increase the turn on voltage of the BGaN PINs to be competitive with the GaN PINs.

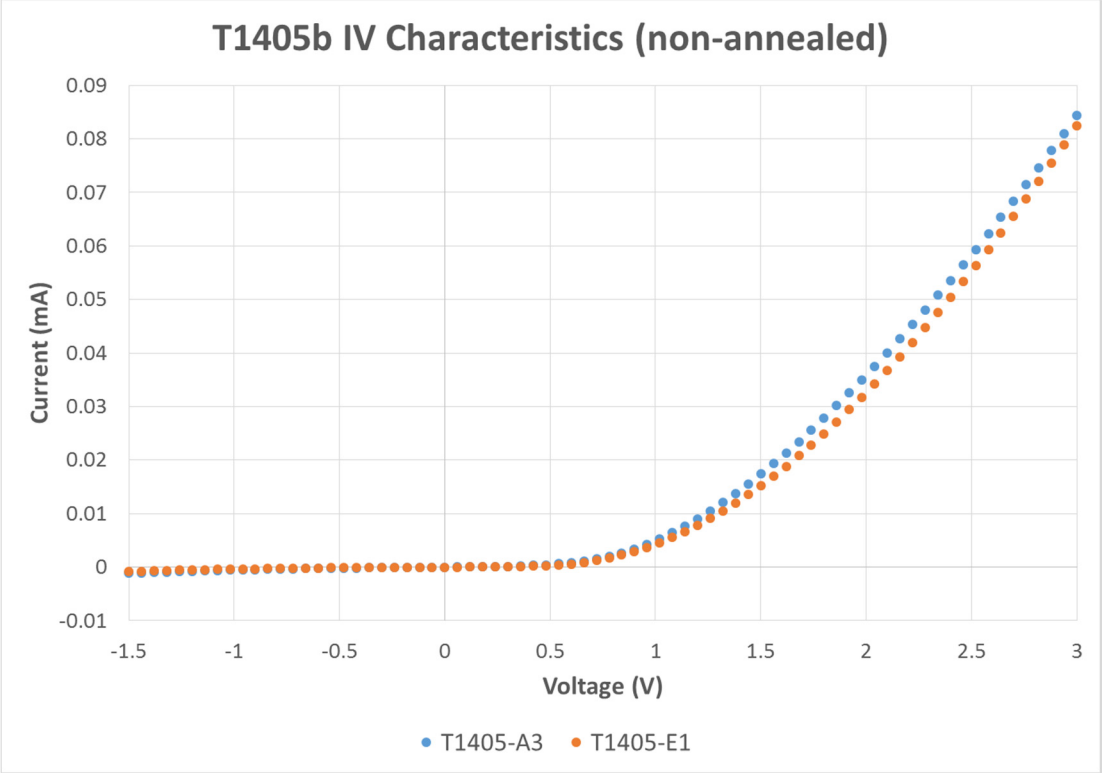

Figure 107: Dark IV Curves for BGaN PINs T1405b-A3 and T1405b-E1 (non-annealed contacts).

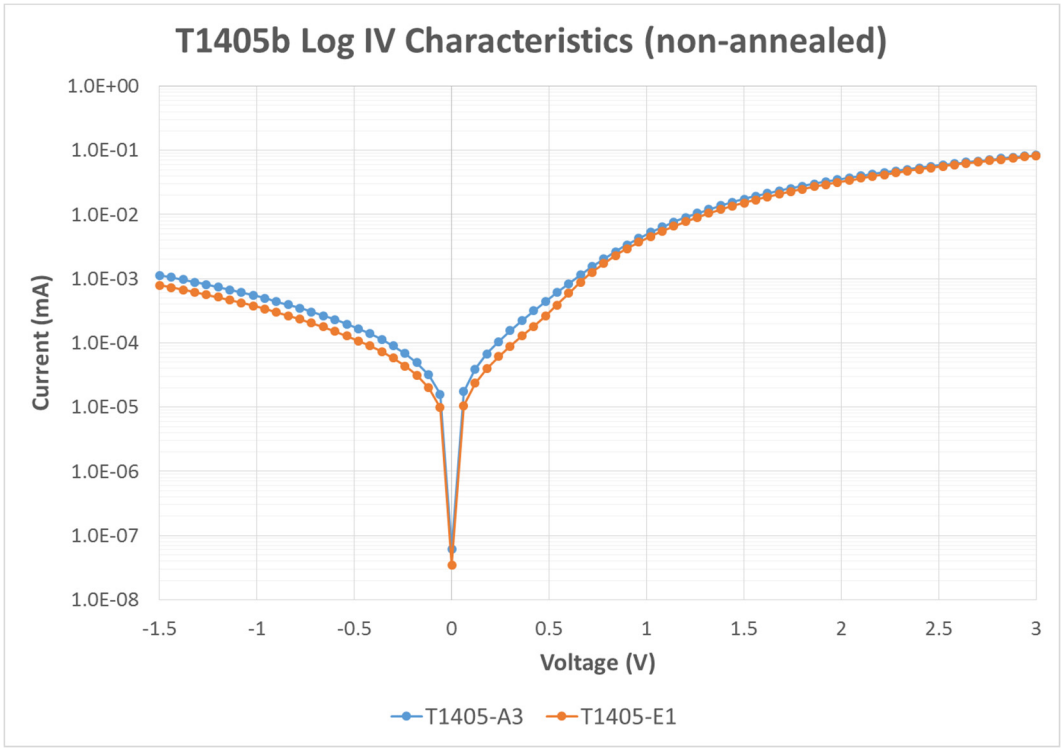

Figure 108: Log-IV Curves for BGaN PINs T1405b-A3 and T1405b-E1 (non-annealed contacts).

Device Betacurrents (SEM Illumination)

Before Ni-63 testing can be done, it is helpful to first run SEM betacurrent measurements (using our SEM equipment's EBIC functionality) to get an idea of the expected performance of these devices. In order to best mimic Ni-63, an energy of 17 keV was used for these tests, with a specimen beam power of approximately 80 uW.

In Figure 109 one can see the S0109B sample (non-annealed) under no illumination (blue) and under 80 uW of illumination, both through the spreading layer (orange) and directly on the p-GaN field (grey). Note that the difference in betacurrent through the spreading layer is approximately 22% here (meaning that 22% of our beam energy is absorbed by the spreading layer).

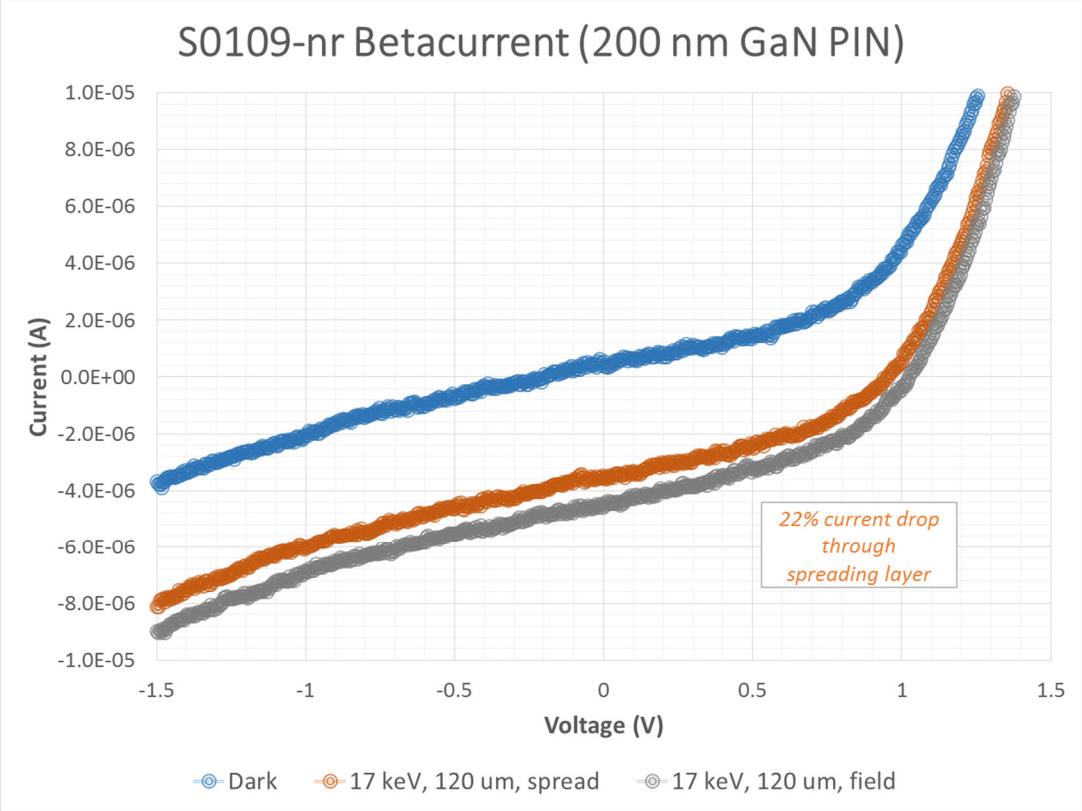

Figure 109: S0109B (non-annealed) SEM-based betacurrent with 80 uW incident power (17 keV).

Note that this predicts a betacurrent of around 4 uA with 80 uW of incident power and a turn on voltage of around 1 V.

In Figure 110 one can similarly see the S0109B sample, but annealed this time. Note the significant decrease in turn on voltage performance here (less than 0.2 V). It is still not certain why the device performance is lowered upon annealing, but this result is consistent with all samples that were processed in this fashion (using both samples grown by our lab and commercial samples) and is mostly likely due to processing issues. Betacurrent performance, however, is unaffected, as one would expect. We still expect to get out around 4 uA for 80uW of incident power.

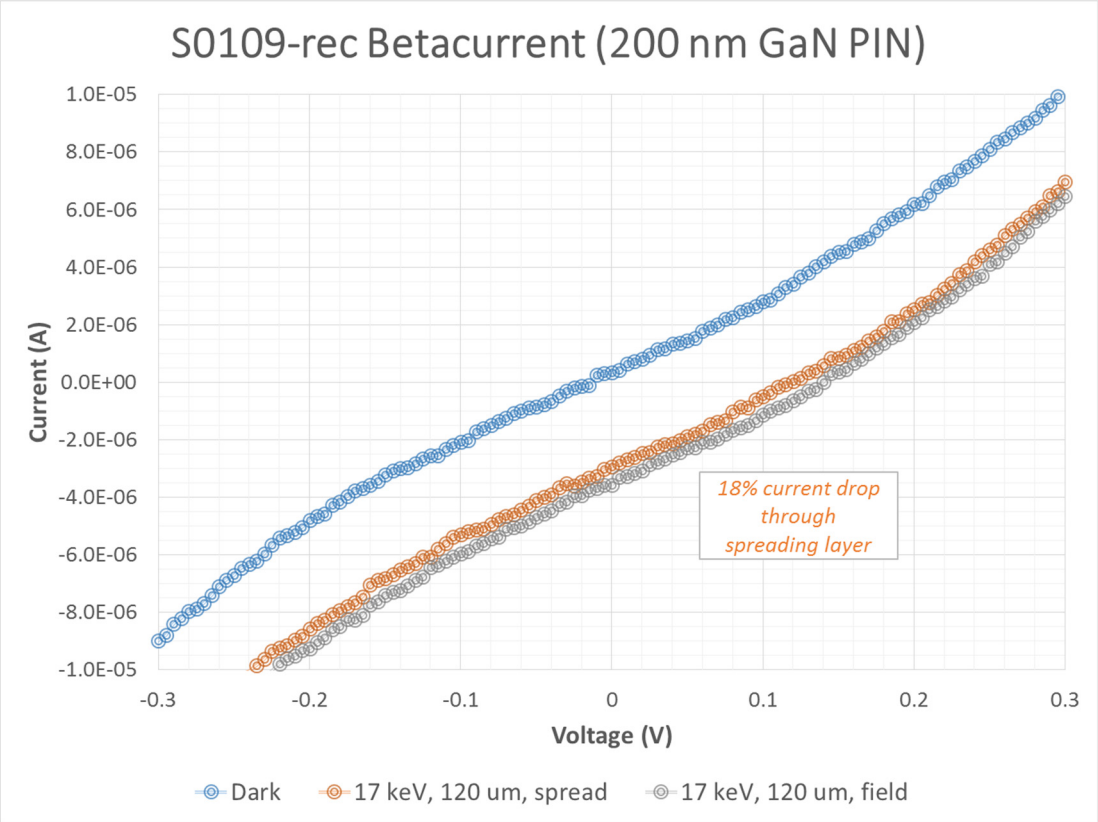

Figure 110: S0109B (annealed) SEM-based betacurrent with 80 uW incident power (17 keV).

Finally, Figure 111 shows the betacurrent measurements for the S0110B device, which is expectedly lower than the S0109B device. The turn on voltage here is less than

0.02 V (since the recombination is very high, as discussed before). The betacurrent here is around 2 uA for an 80 uW incident energy, which is also lower than the 4 uA gotten from the 200 nm intrinsic S0109B samples (again, likely due to losses due to recombination).

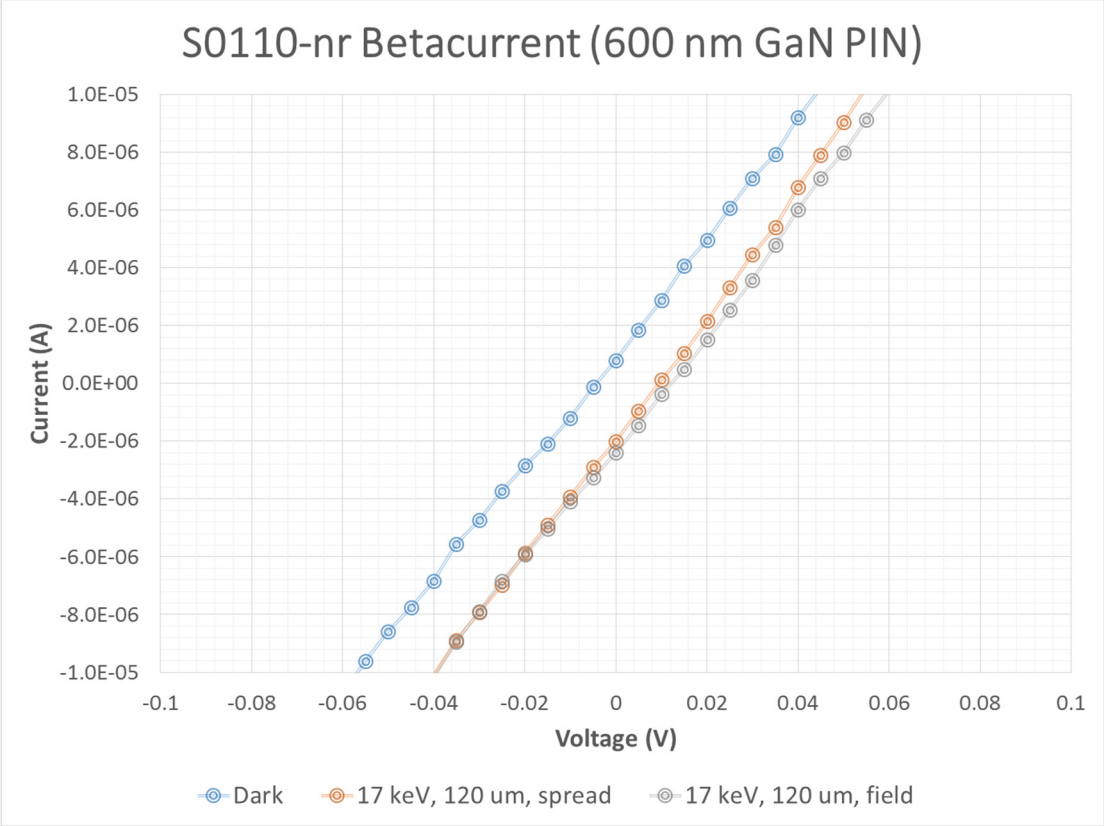

Figure 111: S0110B (non-annealed) SEM-based betacurrent with 80 uW incident power (17 keV).

Device EBIC Results

In addition to SEM-based betacurrent IV measurements, EBIC images were also taken of the full device for S0109B. These images were combined together to create the full EBIC as depicted in Figure 112.

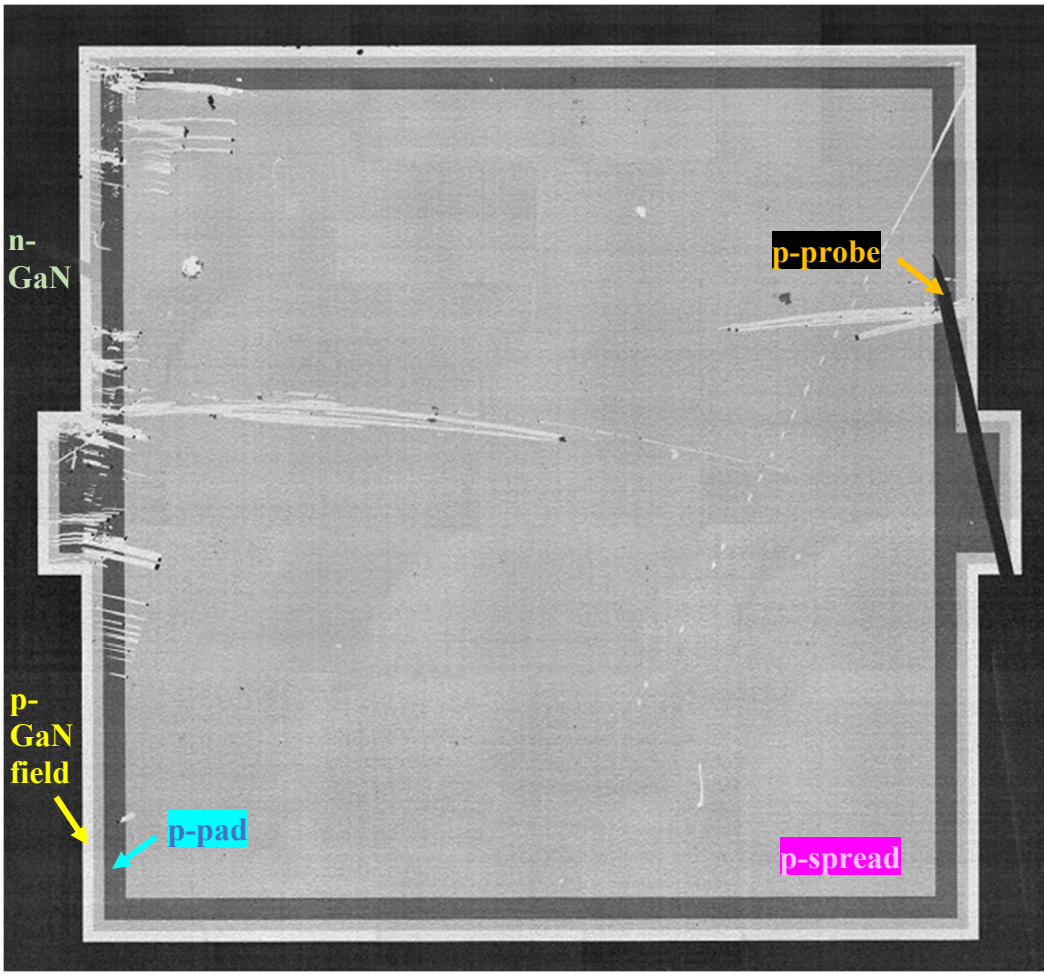

Figure 112: S0109B (non-annealed) EBIC image (17 keV). N-GaN section is darkest (black), p-GaN field (yellow) is brightest, followed by p-GaN spreading layer (purple) and p-GaN pad (blue). The p probe is denoted in orange.

The black area around the border of the image represents the n-GaN region of the device, while the center of the image is the top of the p-GaN mesa. Clearly seen here are the EBIC p-probe (orange), p-GaN field without metals (light grey around the border, yellow) and dark grey p-pads (blue). The spreading layer is the bulk of the visible image here (purple). Note here that the device shows a very consistent betacurrent throughout the entire area, with little to no variation (and thus a high quality PIN).

Note that the contacts were scratched heavily during the EBIC measurements, as seen particularly on the left side of the device, which may have resulted in a high leakage current of this particular device (as discussed previously).

Device Betacurrents (Ni-63 Illumination)

The final tests involved the usage of real Ni-63. For our experimental set up we had three 3 GBq Ni-63 sources that were electrodeposited onto copper foil (named Danton, Marat and Robespierre). The deposition yield was approximately 80% (giving around 2.4 GBq of activity in each source in total). This results in a source power of approximately 3.27 uW of power on each side of the source (or 6.545 uW total).

The first test was performed with our best-performing device – S0109A (as shown by the IV curve experiments). The results can be seen in Figure 113, where the black curve is the dark current and the red and blue curves are with the Danton and Marat Ni-63 sources, respectively. Unfortunately the device's wire bonding broke during testing of the Robespierre source, and thus we do not have data for this source.

The betacurrents for Danton was 1.37 nA and 1.26 nA for Marat. The turn on voltage for these devices were both above 0.75 V, which results in an output power of approximately 1 nW (and an efficiency of 0.03%, or 0.015% for one-sided collection). As we will see later, the betacurrent for this device should have been closer to 2.57 nA, but issues with the 3D printed packaging prevented the device from being raised all the way up to the Ni-63 source (and thus reduced the potential power that reached the device).

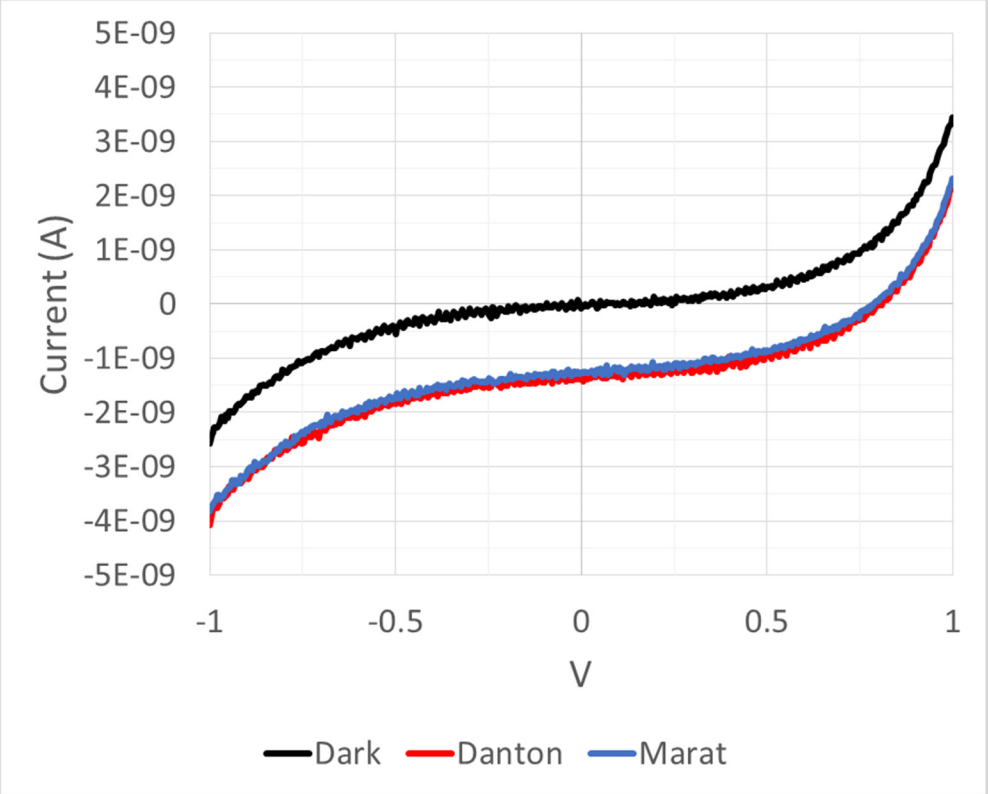

Figure 113: S0109A (non-annealed) Ni-63-based betacurrent with 3 GBq activity (80% yield).

If a 2.57 nA current were achieved, however, this would have resulted in a turn on voltage of over 0.93 V and thus a power of around 2.39 nW. The efficiency of this device would then be approximately 0.07% (0.038% for one-sided collection). This is almost perfectly in line with the simple modeling results we performed, which predict a 0.06% efficiency for one-sided collection. The prediction is approximately 16x less efficient than the iron-doped device described in [14], predominantly due to the reduced intrinsic region thickness (200 nm vs. 900 nm) and increased spreading layer thickness (40 nm vs. 18 nm). Running our full device contact model (including losses due to contact inefficiencies, as seen in Figure 114 and Figure 115) we get an expected efficiency of approximately 0.08% (or 0.04% for one-sided collection), which is only 0.002% higher than our contact model predicts.

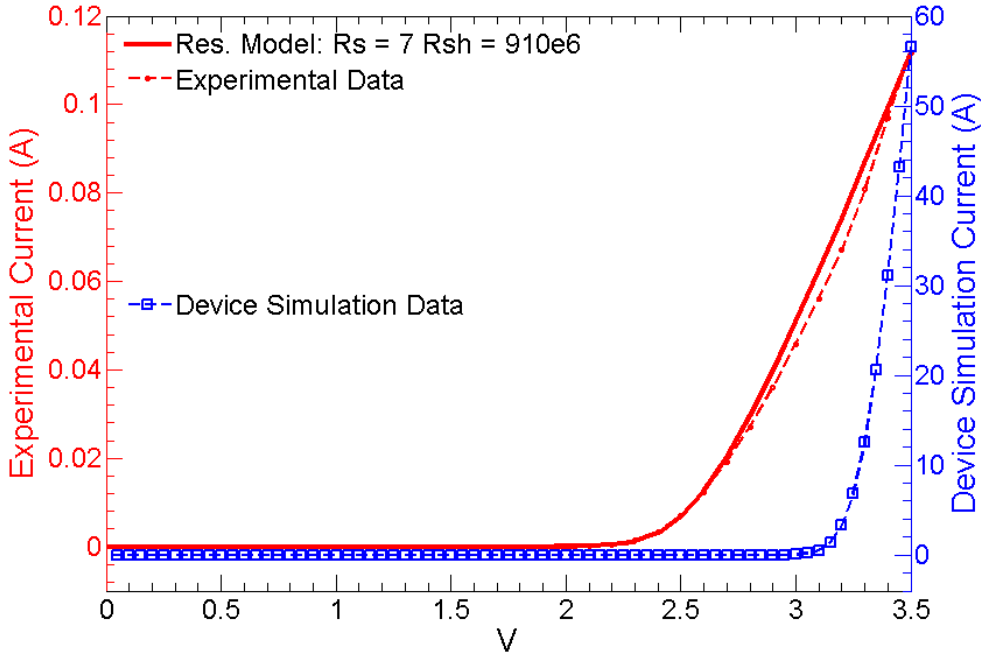

Figure 114: Simulated results for S0109A (non-annealed) assuming a 2.57 nA betacurrent achieved, focusing on overall IV curve shape.

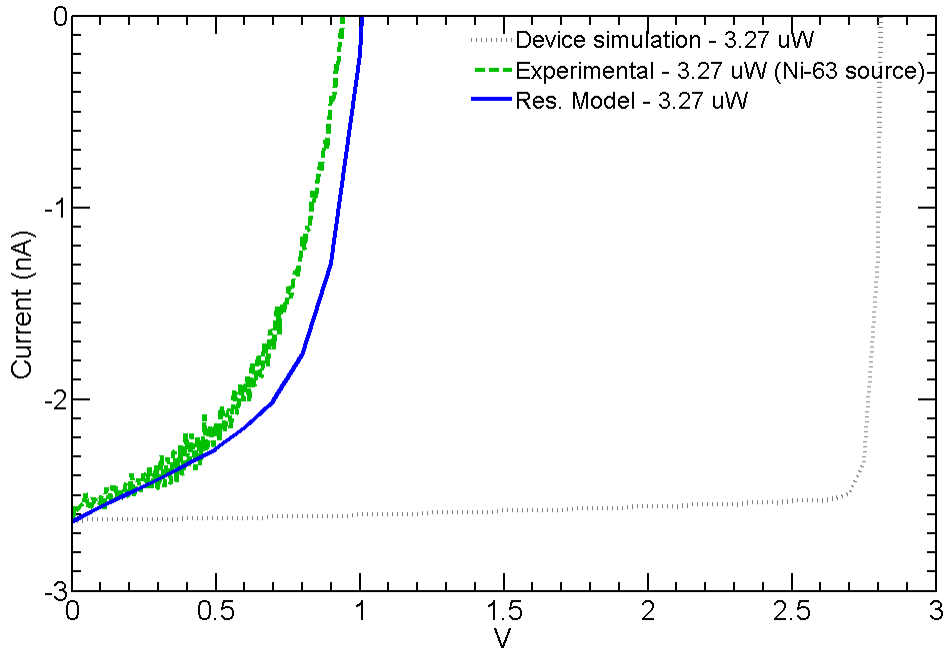

Figure 115: Simulated results for S0109A (non-annealed) assuming a 2.57 nA betacurrent achieved, focusing on betacurrent.

In Figure 116 one can see the Ni-63 betacurrent IV curves for S0110A. Note that the turn on voltage is very low (below 0.0002 V), as expected. The betacurrents here were 430 pA (Danton), 450 pA (Marat) and 780 pA (Robespierre).

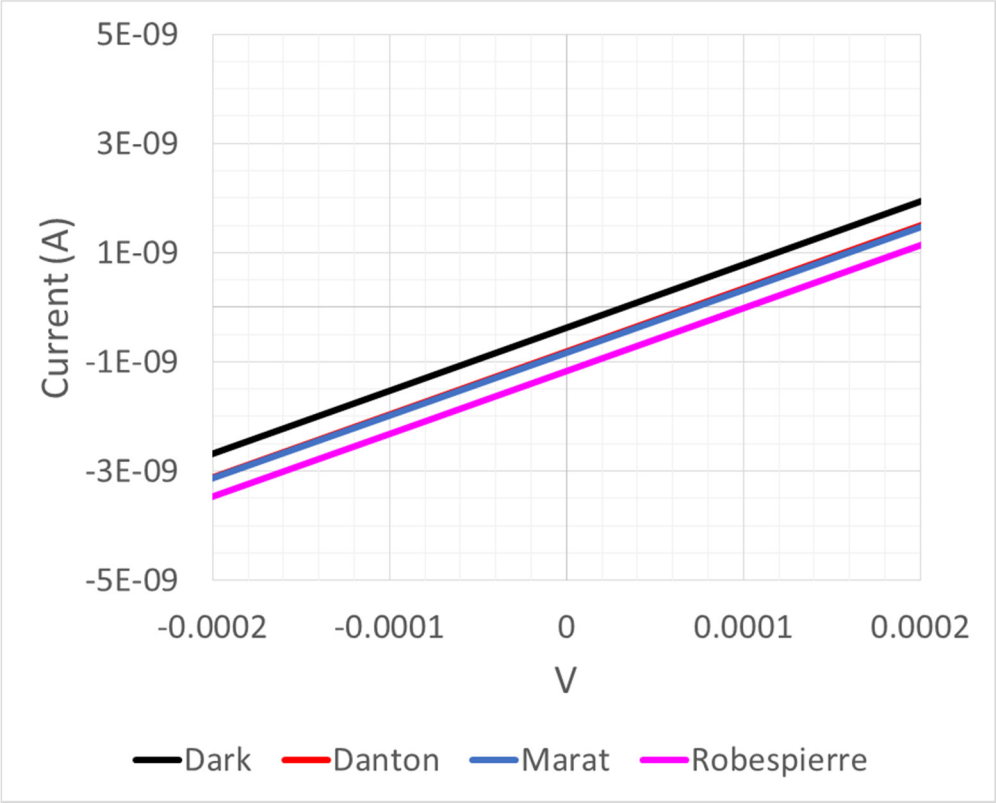

Figure 116: S0110A Ni-63-based betacurrent with 3 GBq activity (80% yield).

Next, Figure 117 shows the betacurrent results for S0109B (non-annealed). Although the betacurrent measurements are similar to S0109A (non-annealed), the turn on voltage is only 0.05V (as opposed to 0.75+ V). This matches well with the results from the EBIC testing done previously, which shows a reduced turn on voltage (as discussed). The betacurrent values here were 930 pA (Danton), 1.1 nA (Marat) and 1.35 nA (Robespierre).

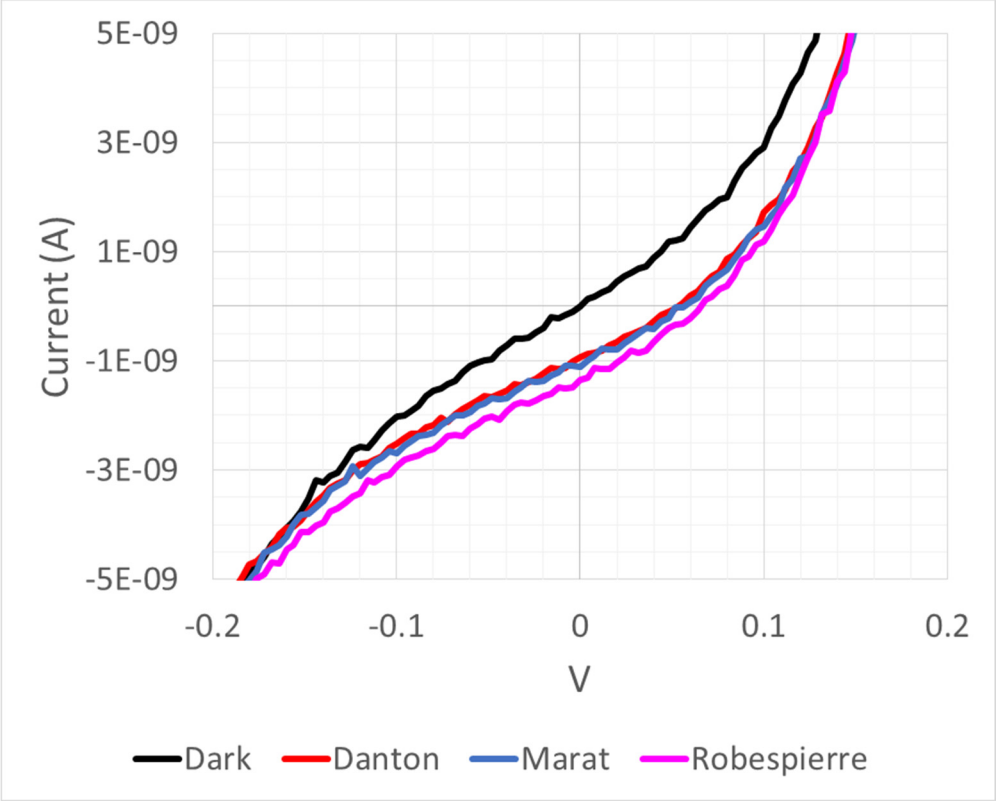

Figure 117: S0109B (non-annealed) Ni-63-based betacurrent with 3 GBq activity (80% yield).

Finally, in Figure 118 one can see the results for S0109B (annealed). As expected, the turn on voltage is very low (below 0.0002 V), which we predicted during our EBIC measurements. For this device, however, we were able to get the device to approach the source the closest of all of the devices. This explains why the betacurrent measurements were so much higher for this device than the others. The betacurrent values here were 2.44 nA (Danton) and 2.5 nA (Robespierre). The betacurrent for Marat could not be obtained due to the wire bonding breaking during the measurements.

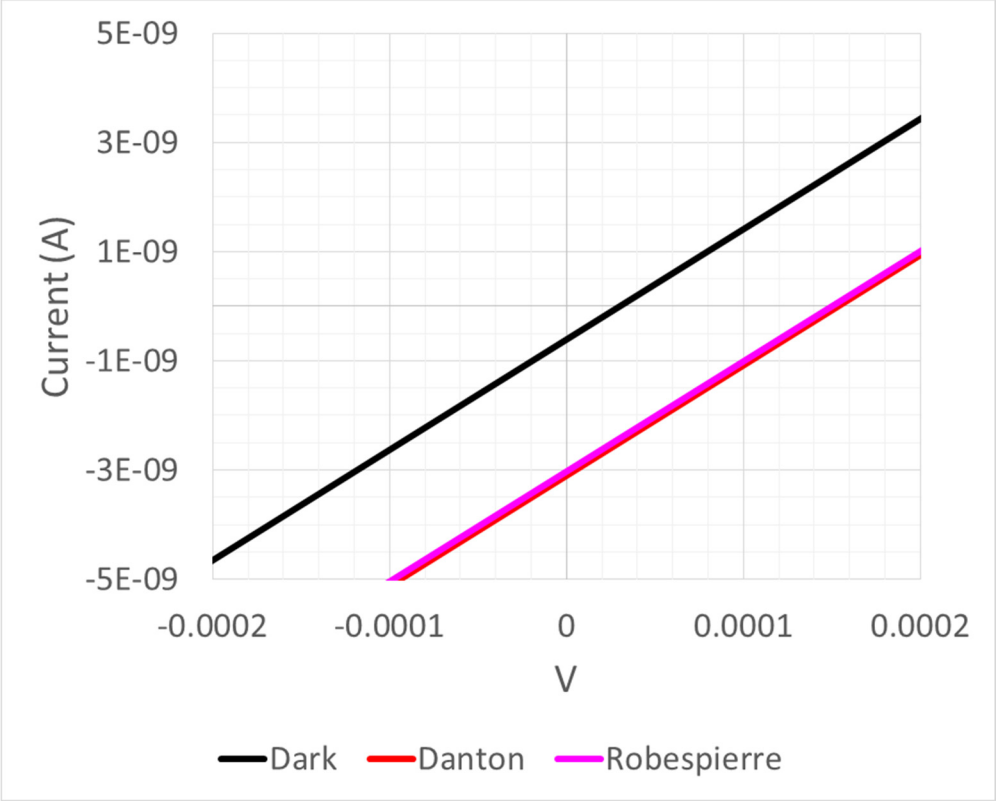

Figure 118: S0109B (annealed) Ni-63-based betacurrent with 3 GBq activity (80% yield).

Conclusions

In conclusion, we have demonstrated a Ni-63 betavoltaic battery device that can achieve an efficiency of approximately 0.03% (stacked) or 0.015% (one-sided), but could potentially reach an efficiency of 0.076% (stacked) or 0.038% (one-sided) with some modifications to our 3D printed packaging (which would allow our device to approach the Ni-63 source closer).

This falls in line nicely with our full contact model predictions, which predicts that our device should be able to achieve 0.08% efficiency (stacked) or 0.04% efficiency (one-sided) – off by approximately 0.002% (one-sided). Even without the contact model (and only using our Ni-63 and Silvaco model), we still predict an efficiency of 0.12% (stacked) or 0.06% (one-sided), which is only off by approximately 0.022% (one-sided).

CHAPTER 7

FUTURE WORK

This section will detail additional work that could be done as a supplement to this research, and builds upon the work that has already been performed here.

BGaN PIN Optimization

The PIN devices grown with a BGaN intrinsic region in these experiments were limited to around 400 or 500 nm in thickness due to cracking issues that appeared with thicker BGaN layers. Further research could be done to determine ways that this BGaN intrinsic region could be expanded to be closer to the 1000 nm goal.

For instance, usage of a superlattice design, as seen in Figure 119, could help alleviate the strain in the BGaN region and allow it to achieve greater thicknesses [63, 64]. That is to say, instead of a single, thick BGaN layer with a lateral-growth cap, it could be beneficial to use two thinner BGaN layers with lateral-growth caps after each.

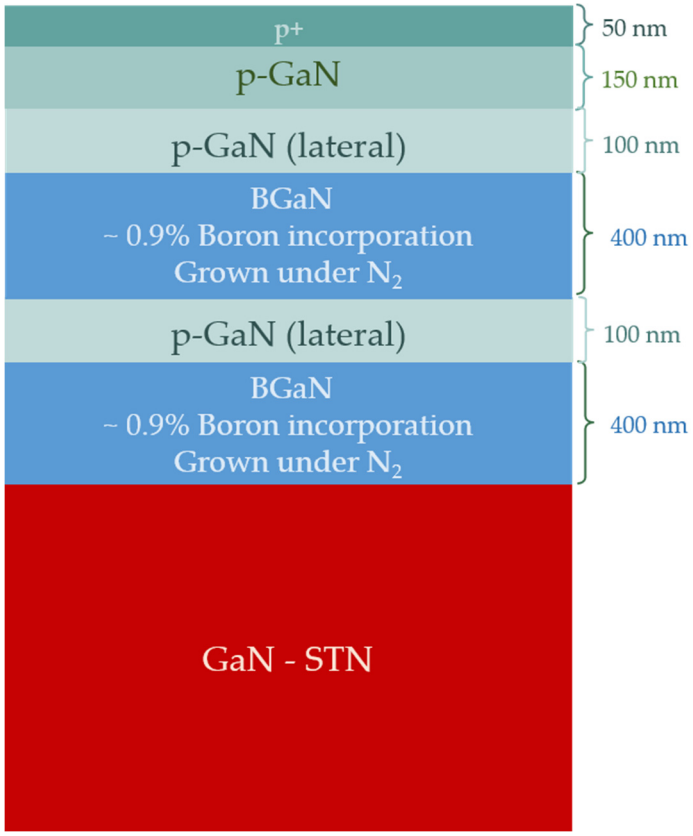

Figure 119: Potential BGaN PIN superlattice design.

More research and optimization would be required to determine the optimal thicknesses of the BGaN and lateral-growth layers, as well as the number of superlattice iterations that should be performed in order to obtain the highest quality material overall.

Realistic Longevity Bombardments

The longevity experiments performed during this research used an SEM with a maximum electron energy of 25 keV. As mentioned previously, the emission profile of Ni-63 details that beta particles with energies up to around 65 keV are possible (although with a much lower probability than 17 keV beta particles).

With usage of an SEM or similar electron beam that can reach 65 keV, performing longevity experiments by SEM bombardment with a Ni-63-like electron energy profile would be possible (rather than assuming that all of the beta particles were

around 20 keV as was assumed in our bombardment experiments). The material interactions of higher-energy beta particles, such as 50 keV and above, should be different than beta particles solely with lower energies (i.e., higher-energy beta particles should be more damaging), even if they are less likely to occur with Ni-63.

Ni-63 Source Substrates

Since Ni-63 suffers from self-absorption issues in the source, the source itself should be optimized to minimize these effects. The current design that we performed our testing with uses Ni-63 that was deposited on piece of a 200 um thick copper foil, which itself absorbs around half of the potential energy from the Ni-63 material.

Low-density metals such as aluminum, as seen in Figure 120, offer the best performance in terms of minimizing self-absorption. The penetration depths of 17 keV electrons in CASINO v2 Monte Carlo simulations were used to generate this figure. It can be seen here that electrons can penetrate nearly three times as far into aluminum compared with copper, so it is the best candidate to be used as a source substrate material.

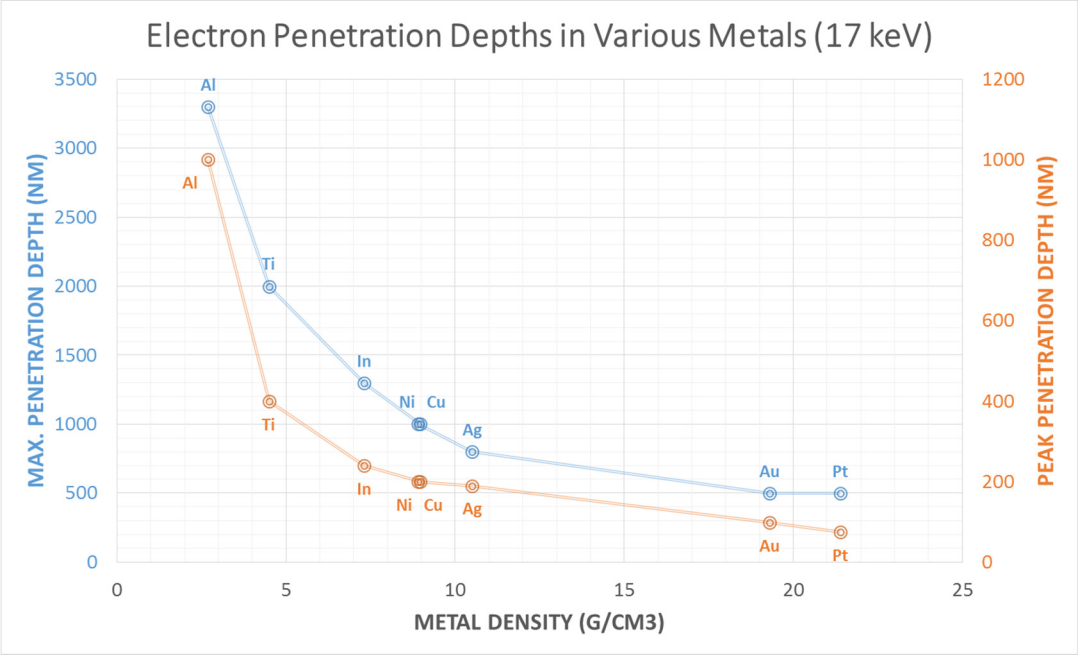

Figure 120: Beta particle penetration depth (max and peak) for 17 keV electron in various metals.

A general overview of this design can be seen in Figure 121, which depicts the electrodeposited Ni-63 onto an aluminum/acrylic substrate. The acrylic substrate could then be dissolved in acetone when it is applied to the betavoltaic device.

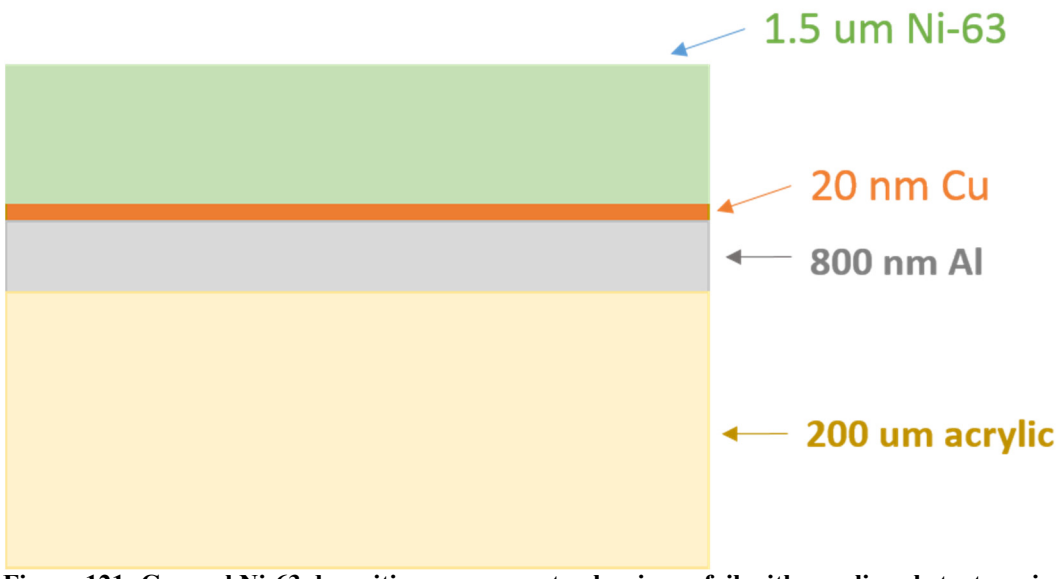

Figure 121: General Ni-63 deposition process onto aluminum foil with acrylic substrate, using a copper strike layer in this case (also possible with nickel strike).

This design could potentially achieve around 85 - 95% source efficiency (depending on the thickness needed to do efficient Ni-63 deposition), since our simulations show around a 4% energy loss per 100 nm of aluminum. This design also allows for easy electrodeposition, since the thick acrylic layer provides a good support layer to attach alligator clips onto for the deposition process.

One issue with this technique is that aluminum is a difficult metal to electrodeposit onto, particularly since aluminum oxidizes very quickly. A common solution in industry is to perform an initial zincate step (or more often double zincate) in order to remove the oxide layer and add a protective zinc layer to prevent reformation of the oxide. Also, since nickel adheres to copper better than aluminum, a thin copper strike

layer (e.g., around 20 nm) is typically added before the nickel electrodeposition (as can be seen in Figure 121). It is also common to use a nickel strike instead of copper, however.

Our partner lab in Paris, CEA-list, attempted many times to perform this process in the lab, using cold nickel instead of Ni-63, and achieved mixed results. The first attempt used the zincate process with a nickel strike, as can be seen in Figure 122. Here, (a) shows the original aluminum foil substrate with no treatment, (b) shows the same aluminum foil after the zincate treatment, (c) is after spontaneous electrochemical replacement of zinc with nickel (as a nickel strike), and (d) is after electrodeposition of nickel. This process resulted in successful deposition of nickel on the aluminum foil, but had a low yield (around 23%). This technique could potentially be improved in the future, with further optimizations (e.g., using a double zincate treatment), to see if the yield can be increased.

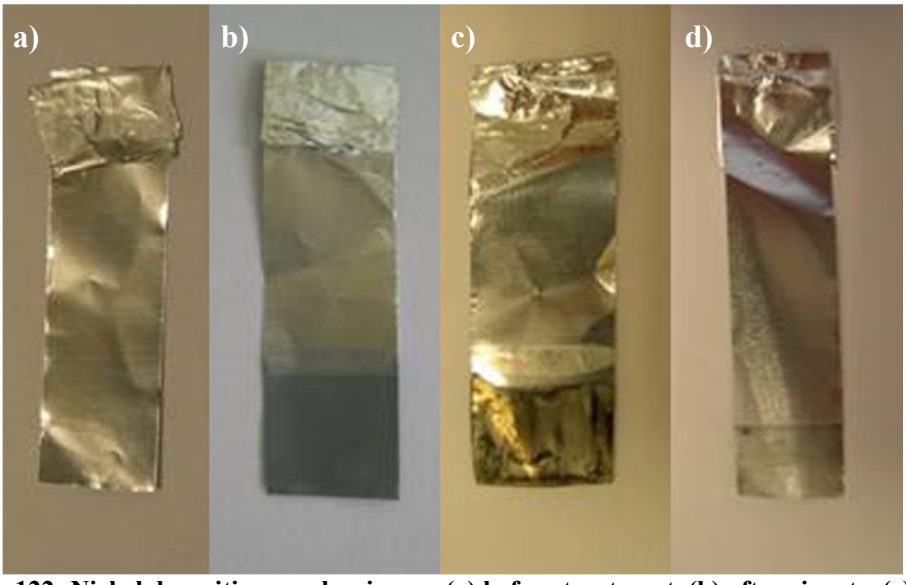

Figure 122: Nickel deposition on aluminum. (a) before treatment, (b) after zincate, (c) after spontaneous electrochemical replacement of Zn with Ni, (d) electrodeposition of Ni – image courtesy CEA-LIST

The next attempt was to add a copper strike before electrodeposition (instead of nickel). During the deposition process, the copper strike layer would eventually separate from the aluminum foil substrate, possibly due to the galvanostatic process between copper and aluminum. In the future we could try optimizing and perfecting the process with a copper strike to increase the effectiveness and chance of success with this technique.

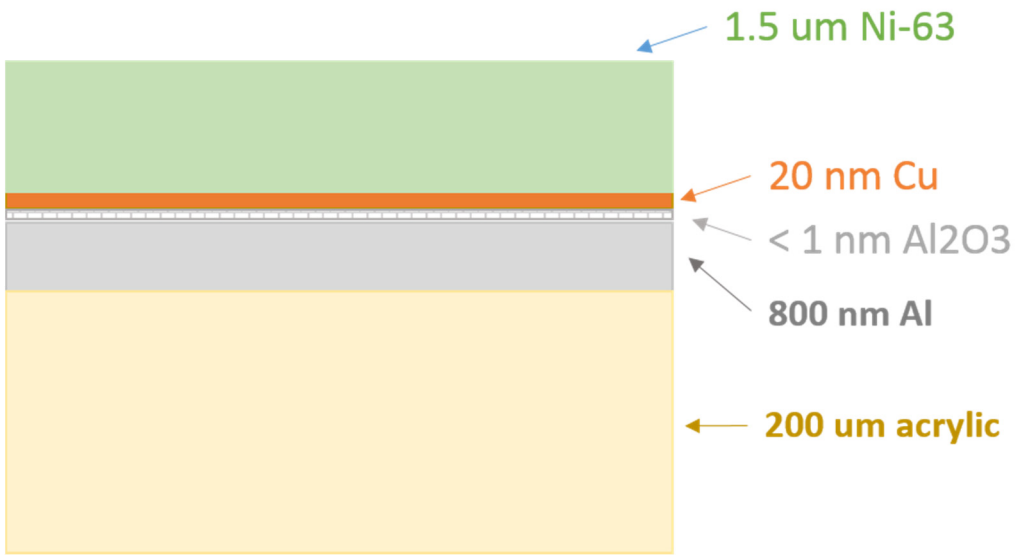

Figure 123: PVD process onto aluminum foil with acrylic substrate.

Another option considered was to use Physical Vapor Deposition (PVD) to deposit the copper strike directly onto the aluminum substrate (and on top of the naturally-formed oxide layer, rather than using the zincate treatment to first remove this layer). This can be seen depicted in Figure 123. Unfortunately experiments to attempt this also were not successful; since the aluminum foil is attached to the acrylic substrate via an electrostatic process, the aluminum separated from the acrylic substrate during the PVD process and the thin aluminum/copper layer became impossible to manipulate.

Further experimentation is required to optimize the zincate treatment process and electrodeposition. We were able to achieve promising results, though with a low yield, when electrodepositing on a nickel strike. We could potentially also achieve success with a copper strike, possibly with an improved double zincate step. Finally, it could be useful to try the PVD process again, but with a different type of aluminum substrate in order to prevent electrostatic separation.

X-Ray Experiments

There are two main energy loss mechanisms that occur during beta particle absorption in a material: atomic excitation/ionization (which have the potential to produce characteristic X-rays) and Bremsstrahlung radiation (caused by beta particle acceleration due to directional changes via interactions with atomic nuclei). Since Bremsstrahlung radiation occurs in the form of X-ray radiation, it would be useful to know how much X-ray energy is released during Ni-63 beta particle interactions with GaN. Doing this would require an SEM (again, preferably with the potential to reach up to around 65 keV electron energy) that is outfitted with an X-ray detector.

An estimate for the Bremsstrahlung radiation wavelength can be calculated from Planck's law:

$$\lambda = \frac{h*c}{E}, \quad (15)$$

Here, h is Planck's constant (6.626×10^{-34} J*s), c is the speed of light (2.998×10^{8} m/s) and E is the maximum energy of our beta particles (around 65 keV for Ni-63, or 1.04×10^{-14} J). This results in an expected radiative wavelength of around 0.02 nm, which is in the hard X-ray range. Of course this is the worst-case scenario (where the full

energy of the highest-energy beta particle will become an X-ray via Bremsstrahlung radiation). On average, however, the energy released (in keV) is expected to be [65]:

$$E_{avg} = 1.4 \times 10^{-7} * Z * E^2 = 18\, eV, \quad (16)$$

Here, Z is the atomic number of our absorbing material (31 for gallium, worst-case assumption) and E is the maximum energy of our beta particles (in keV). Solving for the wavelength using Equation 15 we get 69 nm. Therefore, the most common Bremsstrahlung radiation that is released due to the highest-energy Ni-63 beta particles in GaN will be in the extreme UV range, but could be into the hard X-ray range in the worst case.

In regard to characteristic X-rays due to inner-shell ionization, we can predict the K-alpha X-ray energies for gallium (again, worst case assumption) using the Bohr adaptation of Moseley's law [66]:

$$h\nu_{K\alpha} = R * (Z-1)^2 * \left(\frac{1}{1^2} - \frac{1}{2^2}\right) = 9.18\, keV, \quad (17)$$

Here, R is the Rydberg constant (13.6 eV) and Z is the atomic number of the absorber (31 for gallium). Solving for the wavelength here we get 0.135 nm, which is on the edge of the hard X-ray range. Considering that the binding energy of the K-shell electron of gallium is only 10.37 keV [67], Ni-63 has the potential to ionize inner shell electrons and release characteristic X-ray photons.

By running this experiment at various electron energies and various beam currents, it would be possible to experimentally obtain an idea as to how much X-ray energy is released from these processes and what energies these X-rays typically are (as a spectrum). Particularly noteworthy is that by using a beam energy of under 10 keV (the

gallium K-shell binding energy), we can ensure that the majority of X-rays being released are due to Bremsstrahlung radiation (as we will see later, K-shell ionization in nitrogen only releases a characteristic X-ray with a probability of < 1%, and less than 10% of all L-shell ionizations for gallium and nitrogen will result in characteristic X-rays). This would be useful for determining if additional shielding is necessary if these batteries are used in consumer applications, for instance.

InGaN-based Betavoltaic

As explained in the proposed X-ray study, the K-shell binding energy of gallium is around 10.37 keV, which means that only beta particles with an energy of around 10.37 keV have the capability to ionize them with a high probability. Likewise, the L-shell binding energies of gallium are around 1.1 keV, and the K-shell binding energy of nitrogen is around 400 eV [67]. Unfortunately, energies far above 10 keV will have an ever-decreasing probability of ionization in GaN, since there are no electron shells in GaN with binding energies in the 20+ keV range, for instance [69].

This can be seen visually in Figure 124 and Figure 125, which show the ionization cross-sections for the k-shells of nitrogen and gallium, respectively. For nitrogen, the k-shell electrons have the largest cross section for incident beta particles that are around four times larger than the k-shell binding energy of nitrogen, and the cross-section drops off as the incident beta particle energy increases. Similarly, the k-shell cross section is largest for gallium at around two times its k-shell binding energy and quickly drops off as the incident beta particle energy increases.

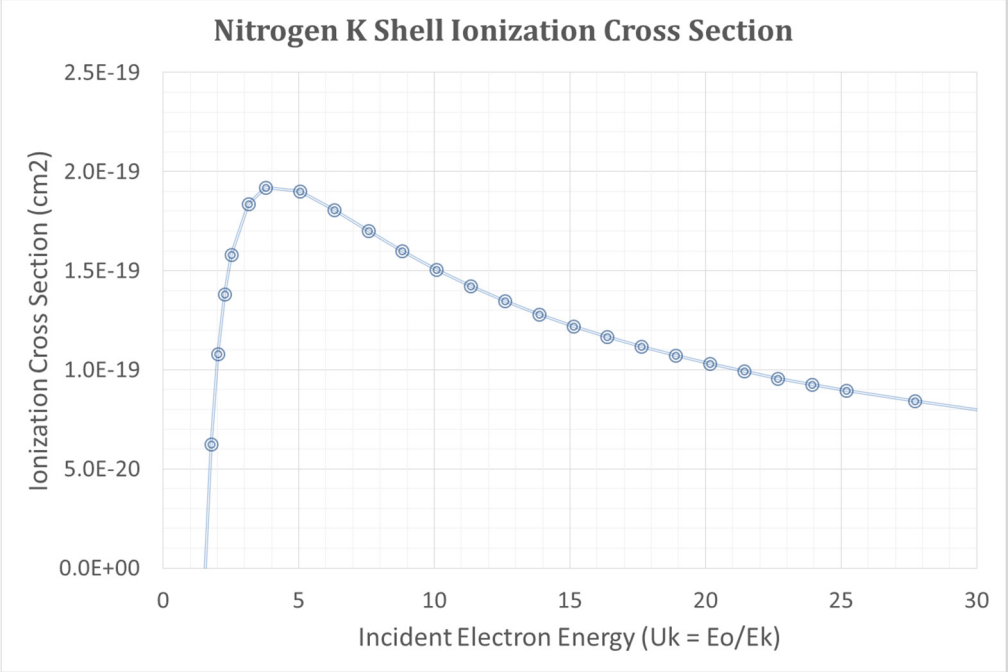

Figure 124: Ionization cross-section for k-shell of nitrogen [72].

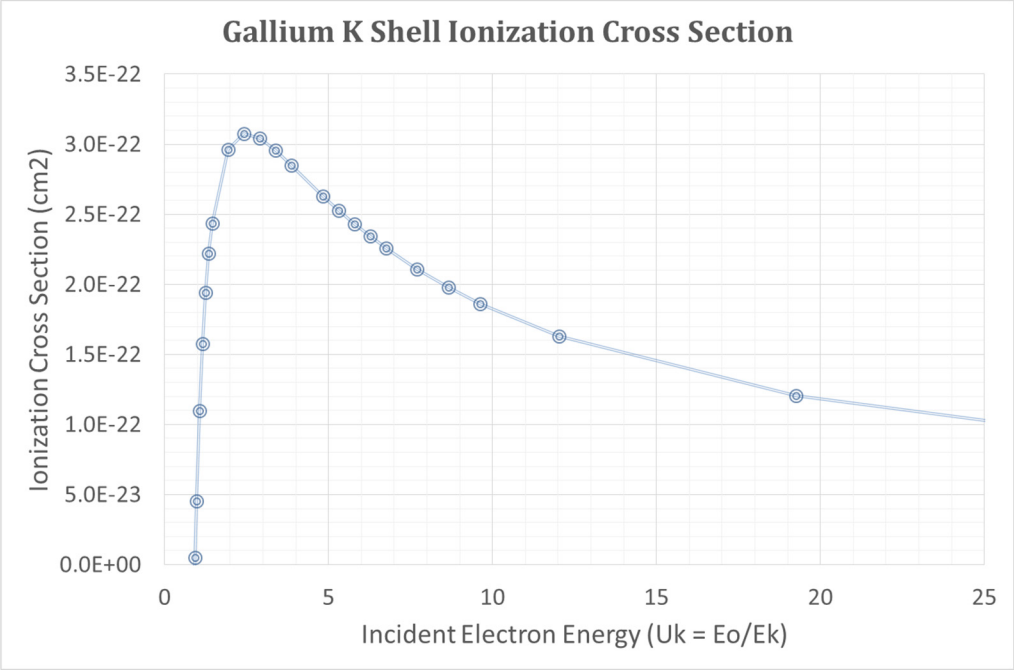

Figure 125: Ionization cross-section for k-shell of gallium [72, 73].

Note that the energy banding effects seen in semiconductors are typically limited to the outer shells, due to the Pauli Exclusion Principle not allowing two electrons to share the same quantum state. The overlap of the outermost shells in crystalline structures forces bands to form (the valence and conduction bands, for example), but there is usually little-to-no overlap of the inner shells of atoms in a crystal and thus this does not apply (and so the inner shells will require more discretized energies in order to ionize) [74-75].

One possibility to increase absorption efficiency for beta particle energies above 20 keV would be through the incorporation of indium (Z=49, with a K-shell binding energy of 27.94 keV, and an L-shell binding energy of nearly 4 keV [67]) in the device's intrinsic region. This would allow for the ionization of K shell electrons in the 28 keV range. The usage of InGaN would give the device absorption edges of approximately 28 keV, 10 keV, 4 keV, 1 keV and 400 eV (In K-shell, Ga K-shell, In L-shell, Ga L-shell and the N K-shell, respectively).

An unfortunate consequence of using indium in the device is that the majority of the ionized K-shell electrons (approximately 85%) will result in releasing of X-ray characteristic radiation rather than Auger electrons. One can see in Figure 126 and Figure 127 the proportion of Auger electrons and X-ray photons for both the K-shell vacancies and the L-shell vacancies, respectively [68]. Note that this same issue is not as important for L-shell vacancies for indium, gallium and nitrogen, since over 90% of all L-shell ionizations will result in Auger electrons rather than X-rays.

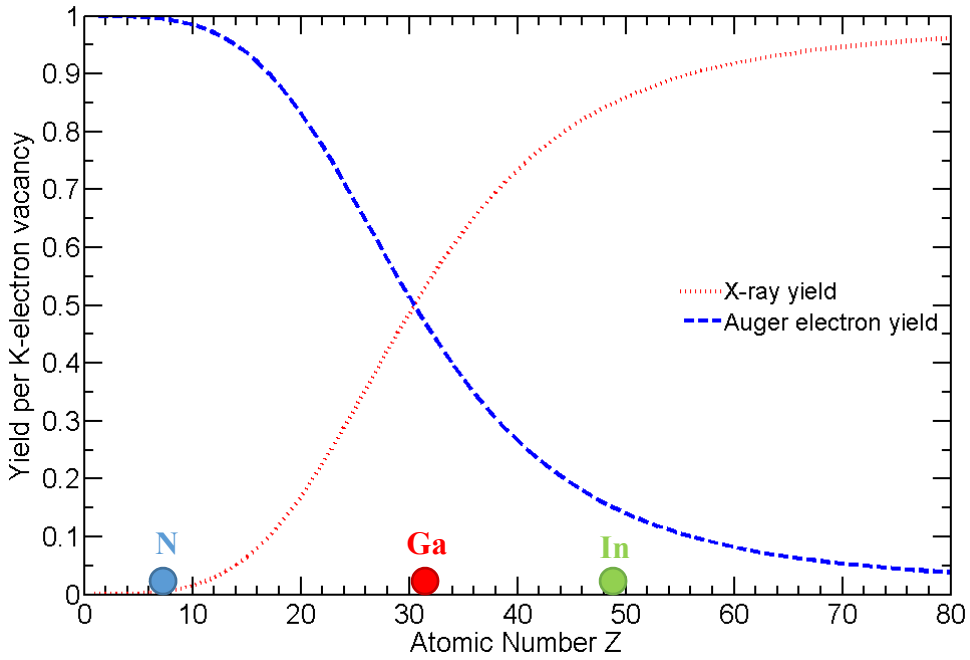

Figure 126: Yield per K-electron vacancy vs. atomic number.

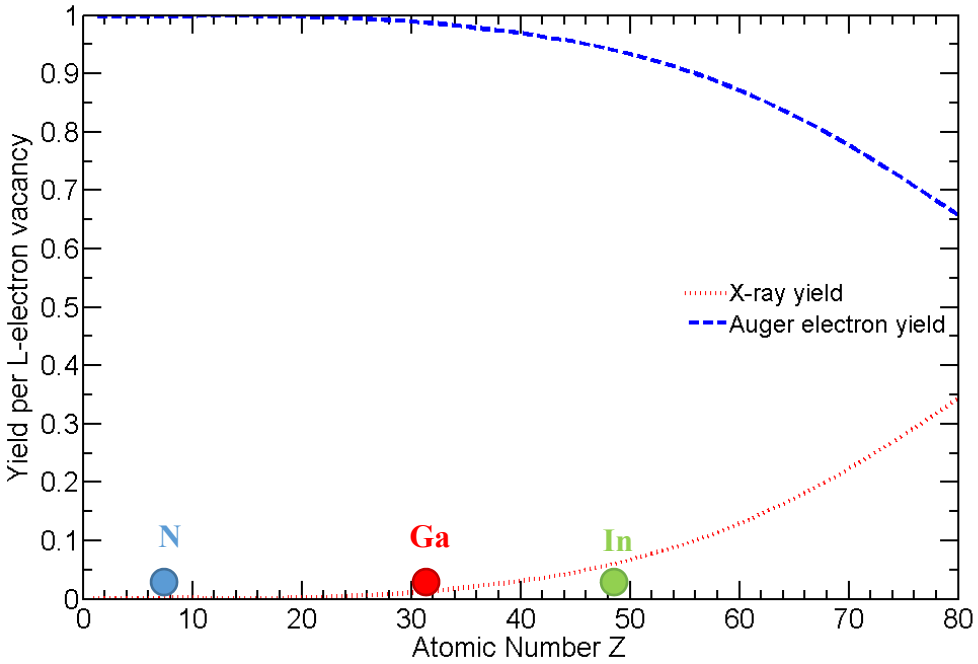

Figure 127: Yield per L-electron vacancy vs. atomic number.

Also noteworthy in Figure 126 and Figure 127 is that nitrogen ionizations (Z=7) will rarely result in the release of X-ray radiation (< 1% probability), and that gallium K-

shell ionizations (Z=31) will only release X-rays (as opposed to Auger electrons) approximately 50% of the time.

Preliminary CASINO v2 Monte Carlo simulations using InGaN (seen in Table 7) have shown a similar IQE between GaN and InGaN with 10% indium, and this is not taking into account the additional Auger electrons that would be generated from the indium K- and L-shells at the 28 keV and 4 keV peaks, respectively (which could increase the efficiency even further).

Table 7: Percentage of SEM absorption occurring between device depths of 150 nm and 750 nm (common intrinsic region), scaled by Ni-63 beta particle probability and bandgap-based beta-efficiency [34].

beam energy	GaN	InGaN (10% In)	InGaN (20% In)	InN
5 keV	4.39%	3.76%	3.23%	0.508%
10 keV	24.35%	23.48%	21.91%	5.41%
15 keV	22.88%	22.61%	22.30%	6.75%
20 keV	13.39%	13.79%	13.60%	4.65%
25 keV	8.07%	8.32%	8.46%	3.10%
30 keV	5.24%	5.49%	5.59%	2.12%
35 keV	2.75%	2.91%	3.11%	1.27%

Because the bandgap of InN is very low (less than 1 eV), it is expected that the potential beta-efficiency would be less than that of a higher bandgap material such as GaN (7% efficiency for InN and 27% efficiency for GaN [34]), which is reflected in this table. A small amount of indium, in the range of 10 – 20%, would afford the benefits of a high bandgap device with the additional absorption edges of 28 keV and 4 keV.

This is illustrated visually in Figure 128, where one can see a log-log plot of the mass-energy absorption profiles of gallium and indium [70]. Clearly seen are the L-shell and K-shell edges for gallium at around 1 keV and 10 keV (in blue), and the L-shell and K-shell edges for indium at around 4 keV and 30 keV (in orange).

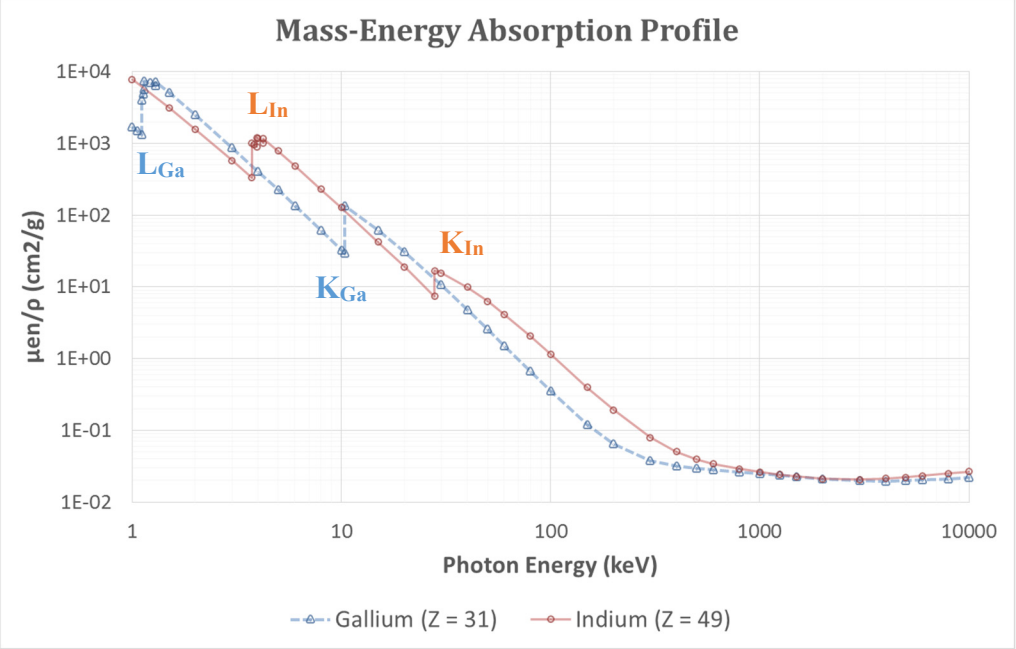

Figure 128: Mass-energy absorption profiles for gallium and indium.

In summation, by adding a small amount of indium into the intrinsic region of the device, it is possible to gain additional inner-shell excitation cites for high-energy beta particles that would promote the generation of secondary electrons and Auger electrons, though at the expense of a higher amount of X-rays produced.

CHAPTER 8

CONCLUSIONS

In this thesis we have covered the creation of a Ni-63 betavoltaic battery, starting with a full model (including, among others, the self-absorption of Ni-63, beta particle absorption in the device materials, device electrical characteristics as EHP collection and losses due to contact efficiencies). This model was shown to be confirmed with both SEM experimentation and by comparison with an experimental device from literature.

In order to determine the material and contact longevity of our betavoltaic device, to ensure the battery could easily last the full 100 year lifespan of the Ni-63 beta emitting material, various experimental longevity studies were also performed via SEM bombardment. These experiments ranged from bombardment of GaN materials alone, bombardment of contacts specifically, and a full 100 year equivalent bombardment. The CL, IV/CV, AFM and SEM measurements confirmed that significant changes were not noticed in neither the GaN materials of our device nor the Schottky and Ohmic contacts.

Part of this thesis focused on the design and development of a BGaN-based PIN device, which could allow for the extension of the intrinsic region of the PIN device (over straight GaN). A carrier density study was performed with various percentages of boron in BGaN to show that the carrier concentration is reduced with increasing boron percentage. Additionally, a study for smoothing the BGaN layer (in order to have a good surface for efficient device contacting) was performed, showing very promising results. Both AFM/SEM and STEM studies showed a good quality surface. One set of device BGaN PIN devices were also processed by our partner lab, LPN, which showed a working PIN (though with a low turn on voltage of around 0.5 V). With proper optimization of the contacts, it could be possible to increase this turn on voltage to make this device competitive with GaN PIN devices.

In order to test our Ni-63 and device models, real Ni-63 experiments were also performed. 3D printed boxes were designed and printed by colleagues at Georgia Tech Lorraine and Institut Lafayette, which helped to facilitate these experiments (allowing for easy loading/unloading of various Ni-63 sources, as well as adjustments of the distance between the devices and the Ni-63 source).

These Ni-63 experiments showed that our devices gave a very high output power (relative to previous experimentation that has been published in literature) of potentially 2.5 nW, though our efficiency was only around 0.08% due to our thin intrinsic region (200 nm) and a thick current spreading layer (50 nm of metals). With a reduced leakage current (and increased open circuit voltage), this efficiency could be even further increased.

In the future, this work could be improved by optimizing the BGaN PIN device, both with improving the contacts and by using a superlattice structure. To take into account damage caused to GaN-based materials due to high energy beta particles, it could also be helpful to perform additional bombardment experiments using a more realistic range of electron SEM energies (ranging potentially up to 65 keV).

Since our Ni-63 source used a thick copper foil layer for electrodeposition, our source ended up being approximately 50% efficient (since all energies released towards the copper foil would be lost). The Ni-63 source design could also be improved so that our device can take advantage of the full energy deposited on the substrate.

Finally, in the future, one could perform X-ray experiments in order to determine the safety and shielding requirements for Ni-63 bombardment in GaN-based materials, and research could be done investigating the usage of InGaN as a device material as a potential improvement over GaN or BGaN.

REFERENCES

[1] Ulmen, B., et al. Development of diode junction nuclear battery using Ni-63. (2009, November). Journal of Radioanalytical and Nuclear Chemistry, 282(2):601-604.

[2] Tang, X., Liu, Y., Ding, D., & Chen, D. (2012). Optimization design of GaN betavoltaic microbattery. Science China Technological Sciences, 55(3), 659-664.

[3] Honsberg, C. B., Doolittle, W. A., Allen, M., & Wang, C. K. C. (2005, January). GaN betavoltaic energy converters. Conference Record IEEE Photovoltaic Specialists Conference (Vol. 31, No. 1, pp. 102-105). IEEE.

[4] Polikarpov, M. A., & Yakimov, E. B. (2013). Application of a scanning electron microscope in simulating a beta-emission-induced current. Journal of Surface Investigation. X-ray, Synchrotron and Neutron Techniques, 7(1), 81-84.

[5] Guoping, Z. U. O., Jianliang, Z. H. O. U., & Guotu, K. E. (2013). A Simple theoretical model for 63 Ni betavoltaic battery. Applied Radiation and Isotopes, 82, 119-125.

[6] San, H., Yao, S., Wang, X., Cheng, Z., & Chen, X. (2013). Design and simulation of GaN based Schottky betavoltaic nuclear micro-battery. Applied Radiation and Isotopes, 80, 17-22.

[7] Manasse, F. K., Pinajian, J. J., & Tse, A. N. (1976). Schottky barrier betavoltaic battery. Drexel Univ., Philadelphia.

[8] Wacharasindhu, T., Kwon, J. W., Meier, D. E., & Robertson, J. D. (2009). Radioisotope microbattery based on liquid semiconductor. Applied physics letters, 95(1), 4103.

[9] Hai-Yang, C., Lan, J., & Da-Rang, L. (2011). Measurement of beta particles induced electron-hole pairs recombination in depletion region of GaAs PN junction. Chinese Physics Letters, 28(5), 058101.

[10] Tang, X., Ding, D., Liu, Y., & Chen, D. (2012). Optimization design and analysis of Si-63Ni betavoltaic battery. Science China Technological Sciences, 55(4), 990-996.

[11] Yao, S., Song, Z., Wang, X., San, H., & Yu, Y. (2012). Design and simulation of betavoltaic battery using large-grain polysilicon. Applied Radiation and Isotopes, 70(10), 2388-2394.

[12] Lu, M., Wang, G., & Yao, C. S. (2012). Gallium nitride for nuclear batteries. In Advanced Materials Research (Vol. 343, pp. 56-61). Trans Tech Publications.

[13] Cheng, Z. J., San, H. S., Feng, Z. H., Liu, B., & Chen, X. Y. (2011). High open-circuit voltage betavoltaic cell based on GaN pin homojunction. Electronics letters, 47(12), 720-722.

[14] Cheng, Z., Chen, X., San, H., Feng, Z., & Liu, B. (2012). A high open-circuit voltage gallium nitride betavoltaic microbattery. Journal of Micromechanics and Microengineering, 22(7), 074011.

[15] Zai-Jun, C., Hai-Sheng, S., Xu-Yuan, C., Bo, L., & Zhi-Hong, F. (2011). Demonstration of a high open-circuit voltage GaN betavoltaic microbattery. Chinese Physics Letters, 28(7), 078401.

[16] Liu, Y., Hu, R., Yang, Y., Wang, G., Luo, S., & Liu, N. (2012). Investigation on a radiation tolerant betavoltaic battery based on Schottky barrier diode. Applied radiation and isotopes, 70(3), 438-441.

[17] Liu, Y., Tang, X., Xu, Z., Hong, L., Wang, P., & Chen, D. (2014). Optimization and temperature effects on sandwich betavoltaic microbattery. Science China Technological Sciences, 57(1), 14-18.

[18] Cheng, Z., Chen, X., San, H., Feng, Z., & Liu, B. (2012). A high open-circuit voltage gallium nitride betavoltaic microbattery. Journal of Micromechanics and Microengineering, 22(7), 074011.

[19] Li, F., Gao, X., Yuan, Y., Yuan, J., & Lu, M. (2014). GaN PIN betavoltaic nuclear batteries. Science China Technological Sciences, 57(1), 25-28.

[20] Lu, M., Zhang, G. G., Fu, K., Yu, G. H., Su, D., & Hu, J. F. (2011). Gallium nitride Schottky betavoltaic nuclear batteries. Energy Conversion and Management, 52(4), 1955-1958.

[21] Tang, X., Liu, Y., Ding, D., & Chen, D. (2012). Optimization design of GaN betavoltaic microbattery. Science China Technological Sciences, 55(3), 659-664.

[22] Duggirala, R., Tin, S., & Lai, A. (2007, June). 3D silicon betavoltaics microfabricated using a self-aligned process for 5 milliwatt/CC average, 5 year lifetime microbatteries. In TRANSDUCERS 2007-2007 International Solid-State Sensors, Actuators and Microsystems Conference.

[23] Guo, H., Li, H., Lal, A., & Blanchard, J. (2008, October). Nuclear microbatteries for micro and nano Devices. In Solid-State and Integrated-Circuit Technology, 2008. ICSICT 2008. 9th International Conference on (pp. 2365-2370). IEEE.

[24] Lee, S. K., Son, S. H., Kim, K., Park, J. W., Lim, H., Lee, J. M., & Chung, E. S. (2009). Development of nuclear micro-battery with solid tritium source. Applied Radiation and Isotopes, 67(7), 1234-1238.

[25] Meier, D. E., Garnov, A. Y., Robertson, J. D., Kwon, J. W., & Wacharasindhu, T. (2009). Production of 35S for a liquid semiconductor betavoltaic. Journal of radioanalytical and nuclear chemistry, 282(1), 271-274.

[26] Wacharasindhu, T., Nullmeyer, B. R., Kwon, J. W., Robertson, J. D., & Garnov, A. Y. (2014). Mechanisms leading to losses in conventional betavoltaics and evolution: Utilizing composite semiconductor with infused radioisotope for efficiency improvement. Journal of Microelectromechanical Systems, 23(1), 56-65.

[27] Liu, P., Chang, Y., & Zhang, J. (2014). Single-walled carbon nanotube film-silicon heterojunction radioisotope betavoltaic microbatteries. Journal of Micromechanics and Microengineering, 24(5), 055026.

[28] Da-Rang, L., Lan, J., Jian-Hua, Y., Yuan-Yuan, T., & Nai, L. (2012). Betavoltaic battery conversion efficiency improvement based on interlayer structures. Chinese Physics Letters, 29(7), 078102.

[29] Da-Yong, Q., Wei-Zheng, Y., Peng, G., Xian-Wang, Y., Bo, Z., Lin, Z., ... & Hong-Jian, Z. (2008). Demonstration of a 4H SiC betavoltaic nuclear battery based on Schottky barrier diode. Chinese Physics Letters, 25(10), 3798.

[30] Deus, S. (2000). Tritium-powered betavoltaic cells based on amorphous silicon. In Photovoltaic Specialists Conference, 2000. Conference Record of the Twenty-Eighth IEEE (pp. 1246-1249). IEEE.

[31] Li, X. Y., Ren, Y., Chen, X. J., Qiao, D. Y., & Yuan, W. Z. (2011). 63Ni schottky barrier nuclear battery of 4H-SiC. Journal of Radioanalytical and Nuclear Chemistry, 287(1), 173-176.

[32] Qiao, D. Y., Chen, X. J., Ren, Y., & Yuan, W. Z. (2011). A micro nuclear battery based on SiC Schottky barrier diode. Journal of Microelectromechanical Systems, 20(3), 685-690.

[33] Ulmen, B., et al. Development of diode junction nuclear battery using Ni-63. Journal of Radioanalytical and Nuclear Chemistry, (2009), Vol. 282 (2), pp. 601-604.

[34] Olsen, L. C. (1993). Review of Betavoltaic Energy Conversion. NASA Conference Publication, (pp. 256–256). NASA.

[35] Gao, H., Luo, S., Zhang, H., Wang, H., & Fu, Z. (2013). Demonstration, radiation tolerance and design on a betavoltaic micropower. Energy, 51, 116-122.

[36] Li, X., Gu, S. Q., Reuter, E. E., Verdeyen, J. T., Bishop, S. G., & Coleman, J. J. (1996). Effect of e-beam irradiation on ap-n junction GaN light emitting diode. Journal of applied physics, 80(5), 2687-2690.

[37] Lopatiuk-Tirpak, O., Chernyak, L., Wang, Y. L., Ren, F., Pearton, S. J., & Gartsman, K. (2007). Doping level dependence of electron irradiation-induced minority carrier diffusion length increase in Mg-doped GaN. Applied Physics Letters, 91(9), 092107.

[38] Chernyak, L., Osinsky, A., Fuflyigin, V., & Schubert, E. F. (2000). Electron beam-induced increase of electron diffusion length in p-type GaN and AlGaN/GaN superlattices. Applied Physics Letters, 77(6), 875-877.

[39] Gelhausen, O., Klein, H. N., Phillips, M. R., & Goldys, E. M. (2003). Low-energy electron-beam irradiation and yellow luminescence in activated Mg-doped GaN. Applied physics letters, 83(16), 3293-3295.

[40] Gelhausen, O., Klein, H. N., Phillips, M. R., & Goldys, E. M. (2002). Influence of low-energy electron beam irradiation on defects in activated Mg-doped GaN. Applied physics letters, 81(20), 3747-3749.

[41] Shmidt, N. M., Vergeles, P. S., Yakimov, E. E., & Yakimov, E. B. (2011). Effect of low-energy electron irradiation on the cathodoluminescence of multiple quantum well (MQW) InGaN/GaN structures. Solid State Communications, 151(3), 208-211.

[42] Vergeles, P. S., Shmidt, N. M., Yakimov, E. E., & Yakimov, E. B. (2011). Effect of low energy electron irradiation on optical properties of InGaN/GaN light emitting structures. physica status solidi (c), 8(4), 1265-1268.

[43] Vergeles, P. S., Shmidt, N. M., & Yakimov, E. B. (2011). Study of the effect of irradiation with the SEM electron beam on cathodoluminescence and the induced current in InGaN/GaN structures with multiple quantum wells. Journal of Surface Investigation. X-ray, Synchrotron and Neutron Techniques, 5(5), 945-948.

[44] Vergeles, P. S., Shmidt, N. M., & Yakimov, E. B. (2012). Influence of electron-beam irradiation in SEM on the cathodoluminescence and electron-beam-induced current in InGaN/GaN light-emitting diodes with a buried active region. Journal of Surface Investigation. X-ray, Synchrotron and Neutron Techniques, 6(6), 890-893.

[45] Nykänen, H., Mattila, P., Suihkonen, S., Riikonen, J., Quillet, E., Homeyer, E., & Sopanen, M. (2011). Low energy electron beam induced damage on InGaN/GaN quantum well structure. Journal of Applied Physics, 109(8), 083105.

[46] Nykänen, H., Suihkonen, S., Sopanen, M., & Tuomisto, F. (2013). Thermally assisted recovery of low energy electron beam irradiation induced optical degradation of GaN. physica status solidi (c), 10(3), 461-463.

[47] Suihkonen, S., Nykänen, H., Tanikawa, T., Yamaguchi, M., Honda, Y., & Amano, H. (2013). Effects of low energy e-beam irradiation on cathodoluminescence from GaN. physica status solidi (a), 210(2), 383-385.

[48] Nykänen, H., Suihkonen, S., Kilanski, L., Sopanen, M., & Tuomisto, F. (2012). Low energy electron beam induced vacancy activation in GaN. Applied Physics Letters, 100(12), 122105.

[49] Nykänen, H., Mattila, P., Suihkonen, S., Riikonen, J., & Sopanen, M. (2012). Low energy electron beam induced damage on gallium nitride based materials. physica status solidi (c), 9(7), 1563-1565.

[50] Lee, D. U., Ha, L. K., Kim, J. S., Kim, E. K., Koh, E. K., & Han, I. K. (2008). Dislocation related defect states in GaN irradiated with 1 MeV electron-beam. physica status solidi (c), 5(6), 1630-1632.

[51] Peng, Z. G., Liu, H. L., & Zhang, R. B. (2012). The Parameter Influence of Electron Beam Irradiation on GaN Based Blue LED. In Advanced Materials Research (Vol. 415, pp. 2093-2096). Trans Tech Publications.

[52] Baghdadli, T., Hamady, S., Gautier, S., Moudakir, T., Benyoucef, B., & Ougazzaden, A. (2009). Electrical and structural characterizations of BGaN thin films grown by metal-organic vapor-phase epitaxy. physica status solidi (c), 6(S2), S1029-S1032.

[53] Salvestrini, J. P., Ahaitouf, A., Srour, H., Gautier, S., Moudakir, T., Assouar, B., & Ougazzaden, A. (2012, January). Tuning of internal gain, dark current and cutoff wavelength of UV photodetectors using quasi-alloy of BGaN-GaN and BGaN-AlN superlattices. In SPIE OPTO (pp. 82682S-82682S). International Society for Optics and Photonics.

[54] Beaumont, B., Haffouz, S., & Gibart, P. (1998). Magnesium induced changes in the selective growth of GaN by metalorganic vapor phase epitaxy. Applied physics letters, 72(8), 921-923.

[55] Beaumont, B., Vaille, M., Nataf, G., Bouillé, A., Guillaume, J. C., Vénnègues, P., & Gibart, P. (1998). Mg-enhanced lateral overgrowth of GaN on patterned GaN/sapphire substrate by selective Metal Organic Vapor Phase Epitaxy. MRS Internet Journal of Nitride Semiconductor Research, 3, e20.

[56] Munson IV, C. E., Arif, M., Streque, J., Belahsene, S., Martinez, A., Ramdane, A., & Ougazzaden, A. (2015). Model of Ni-63 battery with realistic PIN structure. Journal of Applied Physics, 118(10), 105101.

[57] Mnatsakanov, T. T., Levinshtein, M. E., Pomortseva, L. I., Yurkov, S. N., Simin, G. S., & Khan, M. A. (2003). Carrier mobility model for GaN. Solid-State Electronics, 47(1), 111-115.

[58] Vurgaftman, I., & Meyer, J. R. (2003). Band parameters for nitrogen-containing semiconductors. Journal of Applied Physics, 94(6), 3675-3696.

[59] Barbato, M., Meneghini, M., Cester, A., Mura, G., Zanoni, E., & Meneghesso, G. (2014). Influence of shunt resistance on the performance of an illuminated string of solar cells: Theory, simulation, and experimental analysis. IEEE Transactions on Device and Materials Reliability, 14(4), 942-950.

[60] Zhang, J., Lee, S. T., & Sun, B. (2014). Effect of series and shunt resistance on organic-inorganic hybrid solar cells performance. Electrochimica Acta, 146, 845-849.

[61] Witte, H., Fluegge, K., Dadgar, A., Krtschil, A., Krost, A., & Christen, J. (2003). Deep defects in Fe-doped GaN layers analysed by electrical and photoelectrical spectroscopic methods. In MRS Proceedings (Vol. 798, pp. Y5-37). Cambridge University Press.

[62] Polyakov, A. Y., Smirnov, N. B., Govorkov, A. V., Vdovin, V. I., Markov, A. V., Shlensky, A. A., ... & Pearton, S. J. (2007). Properties of Fe-doped, thick, freestanding GaN crystals grown by hydride vapor phase epitaxy. Journal of Vacuum Science & Technology B, 25(3), 686-690.

[63] Gautier, S., Sartel, C., Hamady, S. O. S., Maloufi, N., Martin, J., Jomard, F., & Ougazzaden, A. (2006). MOVPE growth study of B x Ga (1− x) N on GaN template substrate. Superlattices and Microstructures, 40(4), 233-238.

[64] Salvestrini, J. P., Ahaitouf, A., Srour, H., Gautier, S., Moudakir, T., Assouar, B., & Ougazzaden, A. (2012, January). Tuning of internal gain, dark current and cutoff wavelength of UV photodetectors using quasi-alloy of BGaN-GaN and BGaN-AlN superlattices. In SPIE OPTO (pp. 82682S-82682S). International Society for Optics and Photonics.

[65] Johnson, T.E. and Birky, B.K. (2011). Health Physics and Radiological Health Fourth Edition, Philadelphia: Wolters Kluwer.

[66] Lesk, A. M. (1980). Reinterpretation of Moseley's experiments relating Kα line frequencies and atomic number. American Journal of Physics, 48(6), 492-493.

[67] Bearden, J. A., & Burr, A. F. (1967). Reevaluation of X-ray atomic energy levels. Reviews of Modern Physics, 39(1), 125.

[68] Hubbell, J. H., Trehan, P. N., Singh, N., Chand, B., Mehta, D., Garg, M. L., & Puri, S. (1994). A Review, Bibliography, and Tabulation of K, L, and Higher Atomic

Shell X-Ray Fluorescence Yields. Journal of Physical and Chemical Reference Data, 23(2), 339-364.

[69] Klein, C. A. (1968). Bandgap dependence and related features of radiation ionization energies in semiconductors. Journal of Applied Physics, 39(4), 2029-2038.

[70] Hubbell, J. H., & Seltzer, S. M. (2004). NIST: X-Ray Mass Attenuation Coefficients - Table 3. X-Ray Mass Attenuation Coefficients, Physical Reference Data. Retrieved from http://physics.nist.gov/PhysRefData/XrayMassCoef/tab3.html

[71] Krane, K. S. (1988). Introduction to nuclear physics. New York: Wiley, 160-374.

[72] Powell, C. J., Mark, T. D., & Dunn, G. H. (1985). Electron impact ionization. Springer, Berlin, 198.

[73] Chang-Geng, Z., Zhu, A., & Zheng-Ming, L. (2001). Measurement and correction of K-shell ionization cross sections for copper and gallium by electron impact. Chinese Physics Letters, 18(6), 759.

[74] Lower, S. (2007). Chem1 Virtual Textbook: A Reference Text for General Chemistry. S. Lower.

[75] Grundmann, M. (2016). The Physics of Semiconductors: An Introduction Including Nanophysics and Applications. Springer.

VITA

CHARLES E. MUNSON IV

Charles was born in Saint Petersburg, Florida. He attended the University of Florida in Gainesville, Florida, where he received a B.S. in Computer Engineering in 2008. During the pursuit of his doctorate degree, Charles earned his M.S. in Electrical and Computer Engineering at the Georgia Institute of Technology in 2012. He is currently pursuing his doctorate in Electrical and Computer Engineering here as well. In his free time, Charles enjoys writing software, building websites and rock climbing outdoors with friends.